

# **UC Berkeley**

## **UC Berkeley Electronic Theses and Dissertations**

**Title**

Insights on Alzheimer's disease etiology from network approaches in healthy aging

**Permalink**

<https://escholarship.org/uc/item/0hw6f40w>

**Author**

Arnemann, Katelyn Laurel

**Publication Date**

2018

Peer reviewed|Thesis/dissertation

Insights on Alzheimer's disease etiology from network approaches in healthy aging

By

Katelyn Laurel Arnemann

A dissertation submitted in partial satisfaction of the

requirements for the degree of

Doctor of Philosophy

in

Neuroscience

in the

Graduate Division

of the

University of California, Berkeley

Committee in charge:

Professor William Jagust, Chair

Professor Mark D'Esposito

Professor Jack Gallant

Professor Lexin Li

Spring 2018



## Abstract

Insights on Alzheimer's disease etiology from network approaches in healthy aging

by

Katelyn Laurel Arnemann

Doctor of Philosophy in Neuroscience

University of California, Berkeley

Professor William Jagust, Chair

The etiology of Alzheimer's disease involves the presymptomatic development and progression of amyloid- $\beta$  and tau in healthy aging. Amyloid- $\beta$  and tau are naturally occurring proteins that can form abnormal aggregates – amyloid- $\beta$  plaques and neurofibrillary tangles – which constitute the pathological hallmarks of Alzheimer's disease. The initial formation of these aggregates occurs decades before the onset of cognitive symptoms, in individuals otherwise considered to be healthy and unimpaired. This dissertation hinges on *in-vivo* PET imaging of amyloid- $\beta$  and tau in humans using PIB-PET and AV1451-PET to explore this presymptomatic phase of Alzheimer's disease – when pathology is present without detectable symptoms. I place particular emphasis on amyloid- $\beta$  pathology – understanding the factors that underlie vulnerability to amyloid- $\beta$  as well as identifying the initial sources and progressive spread of amyloid- $\beta$  pathology in healthy aging. My focus on amyloid- $\beta$  is consistent with the predominant framework for Alzheimer's disease, the amyloid cascade hypothesis, which contends that amyloid- $\beta$  initiates a slow and ultimately deadly chain of events that results, decades later, in deteriorating memory and breakdown of cognition. In recognition that Alzheimer's disease does not reflect a focal disorder, but rather network failure of large-scale brain systems, I adapt a network-based framework to account for the role of the complex interdependencies between distributed brain regions – of glucose metabolism from FDG-PET, of brain activity from resting-state functional MRI, and of amyloid- $\beta$  from PIB-PET. Examining metabolic brain networks, I reveal widespread, highly systematic reorganization of glucose metabolism in old age – well beyond what has been revealed using other methods – that is more heterogeneous in those possessing both substantial amyloid- $\beta$  and genetic risk for Alzheimer's disease. Further, I demonstrate that the topology of early-life “metabolic inefficiency” – a novel metric that removes the potential association of glucose metabolism with highly connected hubs – explains the topology of amyloid- $\beta$  in healthy aging. Finally, I provide evidence that very early amyloid- $\beta$  accumulation, in those without substantial amyloid- $\beta$  pathology, is multifocal and broadly distributed across brain networks – consistent with shared tissue vulnerability, not transneuronal spread, being the driving force of accumulation of amyloid- $\beta$  pathology. These findings support the notion that shared tissue vulnerability of a metabolic origin drives widespread, systematic accumulation of amyloid- $\beta$  in healthy aging. Future work should uncover the nature and origin of metabolic tissue vulnerability to amyloid- $\beta$ , exploring the complex chain of events that drive widespread age-related

reorganization – especially of cerebral glucose metabolism – and its links other age-related changes and the onset of pathological accumulation of amyloid- $\beta$ .

Dedicated to

My husband James

for his unwavering support

## Table of contents

Chapter 1: Introduction	1
Chapter 2: Metabolic brain networks in aging and preclinical Alzheimer's disease	8
Abstract	8
Introduction	9
Materials and methods	11
Results	16
Discussion	24
Chapter 3: Metabolic inefficiency predicts the topology of amyloid- $\beta$	29
Abstract	29
Introduction	30
Materials and methods	32
Results	37
Discussion	42
Chapter 4: Amyloid- $\beta$ spreads from multiple sources in healthy aging	46
Abstract	46
Introduction	47
Materials and methods	49
Results	53
Discussion	56
Chapter 5: Discussion	59
References	62
Appendix	76

## Acknowledgements

My dissertation is the product of the efforts and support of many researchers and multiple institutions, and would not be possible without the generosity of hundreds of anonymous individuals that participated as subjects in our research efforts. Thank you all!

I am grateful for the mentorship of my advisor Bill Jagust, who has been my mentor for the past six years, and my thesis committee. Bill's unique take on the brain aging and Alzheimer's disease inspired the research in my dissertation. Bill gave me the independence to pursue my research interests and to provide my own network-based spin. His good humor and positivity created a wonderful environment where I was able to grow and thrive as a researcher. I have also been blessed to benefit from the mentorship and support of my thesis committee – Mark' D'Esposito, Jack Gallant, and Lexin Li. Both Jack Gallant and Mark D'Esposito contributed to my early research training, providing invaluable perspectives and advice that influenced my research and career.

I am indebted to the exceptional people that have been in and out of the Jagust Lab over the years, and have contributed in one way or another to my dissertation. Bill Jagust, Suzanne Baker, and Cindee Madison taught me almost everything I know about PET imaging, and Sam Lockhart and Anne Maass further trained me to work with tau PET. Early in my PhD, Cindee Madison trained me in programming and computational methods. Lab managers Jake Vogel, Rachel Bell, and Laura Fenton helped in so many ways, including data acquisition. Suzanne Baker helped manage and preprocess the data. My research assistants Sharada Narayan, Dino Digma, and Ollie Peng checked data quality and assisted with analysis. Anne Berry, Sam Lockhart, and Tessa Harrison provided valuable mentorship. The entire Jagust Lab provided critical feedback, advice, and made my PhD a wonderful experience.

For **Chapter 2**, I would like to acknowledge the essential contributions of Franz Stober and Sharada Narayan for assisting with data analysis, Gil Rabinovici for providing data, and Bill Jagust for assisting with design, conception, and interpretation. For **Chapter 3**, I would like to acknowledge the essential contributions of Anne Maass for assisting with data analysis and Gael Chetelat and Robin de Flores for providing data, and Bill Jagust for assisting with design, conception, and interpretation. For **Chapter 4**, I would like to acknowledge the essential contributions of Dino Digma for assisting with data analysis and Bill Jagust for assisting with design, conception, and interpretation.

Data were provided in part by the Berkeley Aging Cohort Study at the University of California, Berkeley, the Imagerie Multimodale de la maladie d'Alzheimer à un stade Précoce (Caen, France), the Memory and Aging Center at the University of California, San Francisco, and the Human Connectome Project. This work was financially supported by the National Science Foundation, the National Institute on Aging, the John Douglas French Alzheimer's Foundation, the State of California Department of Health Services, the Alzheimer's Disease Research Centre of California, and the Alzheimer's Association. The Helen Wills Neuroscience Institute at the University of California, Berkeley is responsible for providing me with a phenomenal graduate education in neuroscience.

## Chapter 1

### Introduction

Despite being the most prevalent form of dementia, the etiology of Alzheimer's disease (AD) remains poorly understood. While a host of AD-related biomarkers have been characterized, including the hallmark pathologies of AD – amyloid- $\beta$  plaques ( $A\beta$ ) and neurofibrillary tangles (tau) – we still don't fully understand why these pathologies form in the first place or how they come to spread throughout the brain. The difficulty of illuminating the etiology of AD pathology lies in its gradual progression, which occurs over the course of decades, resulting in a protracted pre-symptomatic phase during which there is substantial AD pathology in the absence of clinical symptoms (Sperling et al., 2011). Paradoxically, the necessity of characterizing the processes that initiate and carry forward the complex chain of events ending in profound memory loss and general decline that characterize AD, leads to the study of healthy aging in those with intact cognition. In seeking to delineate the early brain changes that ultimately lead to AD, including how and where AD pathology begins, this dissertation explores how brain structure and function in young adults and cognitively normal older adults can illuminate how AD begins and how it progresses in its pre-symptomatic phase.

The classic model of AD progression, the amyloid cascade hypothesis, posits that  $A\beta$  pathology initiates a complex chain of events that ultimately lead to cognitive decline (Jack et al., 2010). However, the factors that drive accumulation of  $A\beta$  pathology remain unclear.  $A\beta$  pathology exhibits a characteristic spatiotemporal pattern of progression across distributed brain areas, indicative of systematic differences in tissue susceptibility to  $A\beta$  pathology across the brain. The release of  $A\beta$  appears to be linked to neural activity (Bero et al., 2011), potentially explaining the overlapping topology of  $A\beta$  with brain areas that exhibit elevated cerebral glucose metabolism and aerobic glycolysis in early life (Vlassenko et al., 2010, Oh et al., 2016). However, the systematic progression of  $A\beta$  pathology across distributed brain areas may also indicate that  $A\beta$  pathology spreads through distributed brain networks. These two different hypotheses can be contrasted as pathology arising in a single vulnerable epicenter and spreading throughout the brain from that site, as opposed to multiple simultaneous epicenters that share some sort of particular vulnerability.

The dissertation adapts network-based approaches to explore important unanswered questions about how  $A\beta$  pathology begins, spreads, and impacts distributed brain networks in normal aging. **Chapter 2** explores the differential influences of  $A\beta$  pathology and genetic risk for AD on dependencies in cerebral glucose metabolism across distributed brain networks in healthy aging. **Chapter 3** demonstrates the ability of a novel marker of metabolic inefficiency to explain the topology of  $A\beta$  pathology in normal aging, lending support to a role of metabolic processes in driving tissue vulnerability to  $A\beta$ . **Chapter 4** characterizes the progression of  $A\beta$  pathology in normal aging, identifying the initial source(s) of  $A\beta$  pathology and how  $A\beta$  progresses throughout the brain presymptomatically. **Chapter 5** discusses how the insights described in **Chapters 2, 3, and 4** come together to inform understanding of the etiology of AD.

#### Alzheimer's disease.

Rates of AD are projected to nearly quadruple over the next 50 years, affecting 1 of every 45 Americans, constituting a major and worsening national public health crisis (Brookmeyer et al.,

2011). Patients with AD suffer from intractable memory loss, general cognitive decline, personality and behavior changes that all contribute to the devastating impact of AD. Currently, AD is irreversible with treatments only temporarily and marginally alleviating the symptoms of the disease. Approaches for the diagnosis of AD focus on its most prominent symptom – progressive and ultimately profound memory loss – however, efforts driven by scientific research have shifted the definition of the AD away from its symptoms and towards A $\beta$  and tau, which constitute the characteristic pathology of AD (Jack et al., 2018a).

The prominent role of A $\beta$  in AD has been magnified, most notably due to the causal role of genetic mutations affecting the amyloid precursor protein (APP), presenilin 1 (PS1), and presenilin 2 (PS2) in determining autosomal dominant AD (Bertram et al., 2010). While A $\beta$  is an undeniable component of AD, its counterpart tau is more closely linked to the neurodegeneration (LaPoint et al., 2017), hypometabolism (Hanseeuw et al., 2017, Adams et al., 2018), and even episodic memory decline (Maass et al., 2018) associated with AD. However, abnormal tau is not specific to AD, also characterizing frontotemporal dementia, chronic traumatic encephalopathy, and other tauopathies (Iqbal et al., 2005). The deposition and toxic impacts of tau in AD appear to act in concert with A $\beta$  (Ittner and Götz, 2011), with more widespread tau being associated with higher antecedent A $\beta$  deposition (Tosun et al., 2017, Leal et al., 2018).

The amyloid cascade hypothesis contends that accumulation of A $\beta$  initiates a slow but devastating cascade of events – aggregation of tau, synaptic dysfunction, neural death, and brain shrinkage – that ultimately lead to cognitive failure (Jack et al., 2010). Recently, the model has been updated to acknowledge that tau aggregation in the entorhinal cortex and medial temporal lobe can precede accumulation of A $\beta$  later in life (Jack et al., 2013). In autosomal dominant AD, A $\beta$  deposition occurs at least 15 years prior to the anticipated onset of AD (Bateman et al., 2012, Fleisher et al., 2012). AD slowly progresses over the course of decades, with a prolonged presymptomatic phase during which the pathological hallmarks, A $\beta$  and tau, are present and progress without clinical symptoms of the disease (Sperling et al., 2011). Delineating the factors that initiate the accumulation of A $\beta$  and tau – explored in **Chapter 2** and **Chapter 3** – and how they spread through the brain – explored in **Chapter 4** – is central to understanding, treating, and preventing AD.

### The primary pathologies of AD: A $\beta$ and tau.

The normal function of A $\beta$  is not well understood, however amyloid precursor protein (APP) serves a number of biological functions associated with synaptic formation and repair (Priller et al., 2006) and facilitation of axonal transport (Satpute-Krishnan et al., 2006). A $\beta$  is formed through the cleavage of the amyloid precursor protein (APP) by alpha, beta, and gamma secretases. Differential cleavage of APP can produce multiple isoforms of A $\beta$ , with the most common being A $\beta_{40}$  and A $\beta_{42}$ . These isoforms influence the pathogenicity of A $\beta$ , with the more insoluble form A $\beta_{42}$  having a stronger propensity to self-aggregate and form extracellular A $\beta$  oligomers, fibrils, and plaques (Haass and Selkoe, 2007). Synapses endure most of the toxic effects of A $\beta$ , with A $\beta$  application inducing loss of synapses and dendritic spines, long-term depression, and impairment of long term potentiation (Shankar et al., 2008). Further, A $\beta$  may induce tau aggregation (Oddo et al., 2004) and results in a slew of biochemical changes including inflammation, oxidative stress, disrupted homeostasis, and excitotoxicity (Haass and Selkoe, 2007, Roberson et al., 2007). Soluble A $\beta$  is more tightly correlated with cognitive decline than A $\beta$  plaques (Naslund et al., 2000), although neurons surrounding A $\beta$  plaques typically display signs of injury and dysfunction (Tsai et al., 2004). The concentration of A $\beta$

rises with neural activity (Cirrito et al., 2005, Bero et al., 2011), with AD reflecting elevated production and/or reduced clearance of A $\beta$ .

Tau is a microtubule association protein that promotes stability and flexibility of microtubules, particularly in the axonal cytoskeleton, and regulates axonal transport (Gotz et al., 2006). Tau occurs in multiple isoforms, typically in a phosphorylated state. Hyperphosphorylation of tau destabilizes microtubules, causing them to unravel into paired helical filaments, which can subsequently lead to the formation of neurofibrillary tangles (Ballatore et al., 2007). Hyperphosphorylated tau disrupts the integrity of the cytoskeleton of neurons, driving neural dysfunction by interfering with axonal transport and mitochondrial respiration (Gotz et al., 2006, Ittner et al., 2009).

A $\beta$  and tau exhibit distinct spatiotemporal patterns of progression. Staging of A $\beta$  begins in neocortex, implicating frontal, parietal, temporal, and occipital cortex, before spreading to subcortical brain areas, the brainstem, and the cerebellum (Thal et al., 2002). Patients with AD already exhibit widespread A $\beta$  throughout the neocortex, with a similar pattern of A $\beta$  pathology typically observed in patients with mild cognitive impairment (MCI) and cognitively normal older adults with “positive” A $\beta$  PET scans (Rowe et al., 2007). **Chapter 4** uses in-vivo A $\beta$  PET imaging in young and cognitively normal older adults to further explore the “spread” of A $\beta$  across the spectrum of normal aging, identifying potential early sources of A $\beta$  pathology. Tau exhibits more constrained systematic stages than A $\beta$ , beginning in the transentorhinal cortex, spreading to limbic and association cortex, before finally reaching primary sensory cortex (Braak and Braak, 1991). Tau can occur in the locus coeruleus and transentorhinal cortex early in life (Braak et al., 2011), with the interval between the initial occurrence of tau and its widespread distribution throughout the neocortex potentially being as long as 50 years (Braak and Braak, 1995). While the earliest markers of tau are more prevalent with advancing age and can appear much earlier than A $\beta$ , unlike A $\beta$ , tau is typically not widespread throughout the cortex in healthy aging (Scholl et al., 2016).

### In-vivo PET imaging of AD biomarkers.

Positron emission tomography (PET) has revolutionized the study of AD by enabling in-vivo imaging of AD pathology and biomarkers in humans. PET is a highly sensitive imaging technique that detects pairs of gamma rays emitted by a radionucleotide undergoing positron emission decay. A cyclotron is used to produce the positron-emitting isotopes and form radionucleotides, by chemically incorporating the isotopes into a biologically active molecule. For example, the [F<sup>18</sup>] isotope is incorporated into a glucose molecule to form [F<sup>18</sup>]-fluorodeoxyglucose (FDG), a radiotracer that enables imaging of glucose metabolism. Prior to PET imaging, the radionucleotide is typically introduced through intravenous injection, followed by a tracer-dependent waiting period to allow the radionucleotide to equilibrate in the brain before PET imaging commences.

PET images can be modeled to provide information about the spatial distribution of a radiotracer across the brain. 3D reconstruction is possible because positron-electron annihilation events can be localized due to emission of gamma photons at an ~180-degree angle from each other, and also because positrons typically travel < 1-mm before interacting with an electron. Attenuation correction is important, typically involving a transmission scan in the form of a computed tomography (CT) x-ray scan to account for differences in absorption of photons by tissue prior to detection by the sensors (e.g. in superficial versus deep bodily tissue).

To account for the dynamic processes of tracer uptake and decay, PET is modeled when the signal stabilizes, exhibiting steady state tracer uptake. In the absence of arterial blood sampling, models account for the amount of tracer in the blood by relying on signal from a reference region with little or no tracer binding sites. The standard uptake value ratio (SUVR) is computed by taking the ratio of the radioactivity concentration of a voxel or brain region relative to that of the reference region. For reversibly binding radiotracers, the distribution value ratio (DVR) is computed as the ratio of a linear function of a voxel or brain region relative to that of the reference region, referred to as “Logan graphical analysis” (Logan et al., 1996). Methods such as partial volume correction can be used to adjust for the PET signal from neighboring tissue, such as white matter or cerebral spinal fluid, bleeding into the measurement of a given voxel or brain region (Rousset et al., 1998).

### *A $\beta$ PET imaging.*

The topology of A $\beta$  deposition has been imaged in-vivo for more than a decade (Klunk et al., 2004), with the most prevalent radiotracers being [ $C^{11}$ ]-Pittsburgh Compound B (PIB) and [ $F^{18}$ ]-florbetapir. A $\beta$  PET helped reveal the characteristic topology of A $\beta$  in patients with AD, implicating prefrontal, lateral temporal, parietal, and cingulate cortices (Klunk et al., 2004). However, a comparable amount and topology of A $\beta$  is apparent in approximately 20-30% of cognitively normal adults aged 75 and up (Jansen et al., 2015). Identification of “positive” A $\beta$  PET scans has transformed the study of AD, enabling the study of pre-symptomatic AD (Sperling et al., 2011) in **Chapter 2**, **Chapter 3**, and **Chapter 4** and study of the complex interactions between A $\beta$  and other biomarkers, as in **Chapter 2** and **Chapter 3**, as well as cognition. So far, evidence suggests that A $\beta$  pathology is only weakly related to atrophy (Chetelat et al., 2012, Dore et al., 2013, Villemagne et al., 2013), hypometabolism (Lowe et al., 2014), and cognitive decline (Hedden et al., 2013, Jansen et al., 2018). Additionally, A $\beta$  PET opens up the complex challenges of teasing apart brain changes driven by AD pathology from those driven by aging more generally, as demonstrated in **Chapter 2**.

### *Tau PET imaging.*

More recently, the topology of tau has been imaged in-vivo, with a host of radiotracers being explored using multiple derivatives of [ $F^{18}$ ]-THK (including THK5117, THK5317, THK5351), [ $F^{18}$ ]-AV1451 (also known as T807 or flortaucipir), and [ $C^{11}$ ]-PBB3. Existing tau radiotracers have high affinity for tau, however their affinity varies for different domains and forms of tau and the tracers have imperfect specificity leading to off-target binding (Saint-Aubert et al., 2017). In-vivo tau PET imaging can reproduce Braak stages of tau pathology in AD, originally established through postmortem examination of brain tissue (Schwarz et al., 2016, Scholl et al., 2016). In normal aging, tau is more typically constrained to the medial temporal and sometimes the inferolateral temporal cortex, with widespread tau typically only observed in patients (Johnson et al., 2016, Scholl et al., 2016). The topology of tau PET closely tracks that of atrophy (Wang et al., 2016, LaPoint et al., 2017) and hypometabolism (Ossenkoppele et al., 2016), and demonstrates a stronger relationship with clinical symptoms than A $\beta$  (Xia et al., 2017). However, **Chapter 3** demonstrates that the topology of tau does not substantially overlap with cerebral glucose metabolism in early life. Tau PET may help distinguish between and explain the differing symptoms of different variants of AD (Scholl et al., 2017) and dementia (Bejanin et al., 2017).

### *PET imaging of glucose metabolism.*

PET imaging using the  $[F^{18}]$ -FDG radiotracer to detect glucose metabolism instigated the acceptance and expansion of PET imaging. Neural activity appears to be the dominant factor underlying cerebral glucose metabolism (Rocher et al., 2003, Goyal et al., 2014), however multiple metabolic processes certainly contribute (Zimmer et al., 2017). FDG-PET established the existence of a characteristic pattern of hypometabolism in AD, which can distinguish AD from healthy aging and other forms of dementia (Mosconi, 2005, Herholz et al., 2002). Cerebral hypometabolism is an important marker of neurodegeneration, which appears to mirror the topology of tau (Ossenkoppele et al., 2016), precede atrophy (Gordon et al., 2018), and track clinical progression more closely than A $\beta$  or tau (Chiots et al., 2017). **Chapter 2** explores how interdependencies in glucose metabolism, in the form of metabolic brain networks, are differently reflected in aging, pre-symptomatic AD, and clinical AD. The topology of healthy cerebral glucose metabolism and aerobic glycolysis, established by FDG-PET, overlaps with the topology of A $\beta$  in patients with AD, leading to speculation that metabolic tissue vulnerability may drive accumulation of A $\beta$  – a hypothesis explored and expanded in **Chapter 3**.

### Etiology of AD pathology.

A $\beta$  and tau pathologies exhibit distinct, but potentially synergistic spatiotemporal progression (Ittner and Gotz, 2011). Widespread A $\beta$  may drive the spread of tau (Lockhart et al., 2017), with tau pathology being more widespread and accumulating more rapidly in those with substantial deposition of A $\beta$  (Tosun et al., 2017, Leal et al., 2018, Jack et al., 2018b). Although there is some overlap and interdependence of the topologies of A $\beta$  and tau, they reflect distinct mechanisms and spatiotemporal progression in AD. The primary mechanisms driving the progressive accumulation A $\beta$  and tau pathologies throughout the brain remain unclear, however numerous mechanisms have been proposed including transneuronal spread, shared tissue vulnerability, neuroplasticity failure, cascading network failure, and diffusion-based mechanisms.

### *Spread of AD pathology*

Both A $\beta$  and tau, as well as pathologies associated with other neurodegenerative disorders, demonstrate evidence of prion-like qualities (Frost and Diamond, 2010). Intra-cerebral inoculation of cells and/or animals with A $\beta$  results in formation of A $\beta$  aggregates (Eisele et al., 2010, Moreno-Gonzalez and Soto, 2011) and, in the case of tau, spread to downstream brain areas (de Calignon et al., 2012). Alternately, spread of A $\beta$  may occur through extracellular-based transmission via diffusion to spatially contiguous neighbors (Knowles et al., 2011) or transmission via the blood stream (Walker et al., 2012). However, with evidence restricted to cell and animal models, it remains unclear to what extent, if any, transneuronal transmission drives the spread of either A $\beta$  or tau in humans. Unlike A $\beta$ , tau exhibits a highly predictable and constrained sequence of progression (Braak and Braak, 1991) that is consistent with transneuronal spread. **Chapter 4** demonstrates that A $\beta$  is diffuse and multifocal, with even the earliest sources of A $\beta$  broadly distributed and implicating multiple brain networks, making connectivity-based spread unlikely. Cascading network failure may provide an alternate framework of how pathology may “spread” to distal brain areas through propagation of dysfunction through the system as it slowly breaks down (Jones et al., 2016, Jones et al., 2017).

### *Vulnerability to AD pathology.*

The differential topologies of early A $\beta$  and tau suggest that distinct, although potentially synergistic, mechanisms initially drive formation of A $\beta$  and tau pathologies. The diffuse, multifocal accumulation of A $\beta$  in its earliest stages demonstrated in **Chapter 4** indicates that A $\beta$  may be driven by shared tissue vulnerability across distributed brain areas. Metabolic tissue vulnerability may explain differential vulnerability to A $\beta$ , as the topology of A $\beta$  overlaps with that of aerobic glycolysis and glucose metabolism (Vlassenko et al., 2010, Oh et al., 2016). Synaptic activity, the primary driver of cerebral glucose metabolism (Rocher et al., 2003, Goyal et al., 2014), results in the secretion of A $\beta$  (Cirrito et al., 2005, Bero et al., 2011). However, the topology of A $\beta$  in patients with AD also overlaps with highly connected brain regions called “hubs” (Buckner et al., 2009), which in simulations exhibit heightened vulnerability to activity-dependent degeneration (de Haan et al., 2012). **Chapter 3** uses hubs to demonstrate that a novel marker of “metabolic inefficiency” explains the topology of A $\beta$ , but not tau, in healthy aging. While the mechanism remains unclear, tau is thought to reflect neuroplasticity failure (Mesulam, 1999).

### *Lifespan perspective on vulnerability.*

The processes associated with typical brain aging play a critical role in rendering the aging brain vulnerable to AD, with the markers of AD appearing at higher and higher rates with advancing age. The prevalence of substantial levels of A $\beta$ , comparable to that of patients with AD, increases from approximately 10% of cognitively normal older adults at age 50 to 44% at age 90 (Jansen et al., 2015). Tau in the transentorhinal cortex can be observed in some young adults, becoming increasingly frequent with advanced aging, to the point of being nearly universal by age 90 (Braak and Braak, 1997). As with other age-related conditions, understanding the contributions of the entire lifespan of brain function is central to understanding why AD develops (Jagust and Mormino, 2011).

There are a wide variety of age-related changes to brain structure and function that may contribute to the vulnerability of the aging brain to AD. The neural systems impacted by aging – the medial temporal lobe memory and the frontostriatal executive systems – overlap with those impacted by AD (Jagust, 2013). Aging is associated with widespread reorganization of brain function, both of spontaneous brain function at rest (Tomasi and Volkow, 2012, Geerligs et al., 2015) and as well as reorganized activation during cognitive tasks (Park et al., 2004, Prakash et al., 2012). Impaired structural integrity of white matter pathways in old-age (Andrews-Hanna et al., 2007, Saenger et al., 2017) may underlie reorganization of functional connectivity and task-related brain activation (Sala-Llonch et al., 2015). However, there is also evidence of age-related synaptic reduction (Masliah et al., 1993) as well as reduction of glucose metabolism and aerobic glycolysis (Chetelat et al., 2013, Goyal et al., 2017). In **Chapter 2**, metabolic brain networks reveal widespread, systematic changes in glucose metabolism in older compared to younger adults. Further work is necessary to demonstrate how these changes reflect and confer vulnerability to the aging brain to drive it to begin the cascade of events that lead to AD.

### Network-based approaches to aging and AD.

Network-based approaches stemming from graph theory provide a framework for modeling pairwise structural and functional interdependence across the brain (Bullmore and Sporns, 2009). While there is some utility in considering modules or units – whether they are voxels, brain

regions, or brain networks – as independent entities, ultimately most aspects of behavior and disease are the products of interdependent complex distributed systems. Graphs (i.e. networks) use edges to represent dependencies between the units of the graph, called nodes or vertices. Network-based approaches can provide a unifying framework for understanding the interdependence between A $\beta$ , tau, and neurodegeneration and their links to healthy brain function, reorganization, behavior, and cognitive decline.

AD leads to profound disruption of large-scale brain networks. Modularity, a fundamental principle of brain organization that characterizes the segregation of the brain into modules underlying distinct cognitive functions, shows signs of disruption in old-age (Chen et al., 2011, Geerligs et al., 2015), which more pronounced in AD, showing step-wise reductions with AD severity (Brier et al., 2014a). Reorganization of brain connectivity over the course of AD may begin with reduced posterior connectivity in initial stages followed by increased anterior connectivity with further disease progression (Jones et al., 2016), and A $\beta$  further alters functional connectivity of distributed brain networks, including the default mode network, in cognitively normal older adults (Sperling et al., 2009).

A foundational study by Seeley and colleagues (2009) demonstrates the power and utility of a network-based framework for explaining the distinct patterns of atrophy observed across subtypes of dementia. Cast in a network framework, we can suddenly understand that distributed patterns of atrophy track the functional and structural independencies of the healthy brain. Each form of dementia may reflect failure of a different brain system, with AD reflecting network failure of the predominant brain system (Raj et al., 2012). These patterns may reflect prion-like spreading of pathological proteins, like tau, through neural connections in neurodegenerative diseases (Frost and Diamond, 2010). However, systematic patterns could also reflect cascading network failure over the course of decades (Jones et al., 2016). Even in the absence of transneuronal spread through neural connections, network-based approaches can be used to model and predict the accumulation of pathology and neurodegeneration through the brain, as demonstrated in **Chapter 4**.

Where and how different brain regions are embedded in the topology of brain networks may provide insights into their vulnerability. Across brain disorders, lesions appear to be more common in densely connected brain regions called “hubs” (Crossley et al., 2014), with A $\beta$  pathology being more concentrated in hubs in patients with AD (Buckner et al., 2009). Network-based simulations suggest that activity-dependent degeneration may explain hub vulnerability in AD (de Haan et al., 2012) and that attacks on hubs produce greater disruption of brain function (Crossley et al., 2014). The topological embedding of brain areas within a network could explain differences in regional vulnerability due to many factors, including trophic failure, nodal stress, and transneuronal spread (Zhou et al., 2012).

By investigating pairwise dependencies across the brain, network approaches extract a shared pattern of covariation over time within subjects in the case of fMRI (Salvador et al., 2005) and electrophysiological methods (Bassett et al., 2006, Stam et al., 2007) or across subjects in cross-sectional studies of PET (Horwitz et al., 1986, Sepulcre et al., 2013), structural MRI (He et al., 2007), and gene expression (Richiardi et al., 2015). Network methods have revealed a wide variety of insights about aging and AD. This dissertation examines information from metabolic brain networks using FDG-PET in **Chapter 2**, functional brain networks using resting-stage functional MRI in **Chapter 3**, and directed progression networks of A $\beta$  using PIB-PET in **Chapter 4**.

## Chapter 2

### Metabolic brain networks in aging and preclinical Alzheimer's disease

\* This chapter is based on the following publication:

Arnemann, K.L., Stober, F., Narayan, S., Rabinovici, G. D., Jagust, W. J., (2017). Metabolic brain networks in aging and preclinical Alzheimer's disease. *NeuroImage Clin*, 17, 987-999.

#### Abstract

Metabolic brain networks can provide insight into the network processes underlying progression from healthy aging to Alzheimer's disease. We explore the effect of two Alzheimer's disease risk factors, amyloid- $\beta$  and ApoE  $\epsilon 4$  genotype, on metabolic brain networks in cognitively normal older adults (N=64, ages 69-89) compared to young adults (N=17, ages 20-30) and patients with Alzheimer's disease (N=22, ages 69-89). Subjects underwent MRI and PET imaging of metabolism (FDG) and amyloid- $\beta$  (PIB). Normal older adults were divided into four subgroups based on amyloid- $\beta$  and ApoE genotype. Metabolic brain networks were constructed cross-sectionally by computing pairwise correlations of metabolism across subjects within each group for 80 regions of interest. We found widespread elevated metabolic correlations and desegregation of metabolic brain networks in normal aging compared to youth and Alzheimer's disease, suggesting that normal aging leads to widespread loss of independent metabolic function across the brain. Amyloid- $\beta$  and the combination of ApoE  $\epsilon 4$  led to less extensive elevated metabolic correlations compared to other normal older adults, as well as a metabolic brain network more similar to youth and Alzheimer's disease. This could reflect early progression towards Alzheimer's disease in these individuals. Altered metabolic brain networks of older adults and those at the highest risk for progression to Alzheimer's disease open up novel lines of inquiry into the metabolic and network processes that underlie normal aging and Alzheimer's disease.

## **Introduction**

Distinct patterns of change in brain and cognitive functions dissociate the processes of healthy aging and Alzheimer's disease. Beyond the brain changes and gradual cognitive decline characteristic of normal aging (Park and Reuter-Lorenz, 2009), the hallmark of Alzheimer's disease is a stereotyped spatial pattern of neuritic plaques (amyloid- $\beta$  or A $\beta$ ) and neurofibrillary tangles (tau), alongside loss of episodic memory and cognitive decline. Early identification of vulnerability to Alzheimer's disease – prior to the onset of clinical symptoms – is a central problem for the study of aging. PET imaging has revealed that some cognitively normal older adults harbor substantial A $\beta$  (Sperling et al., 2011) and/or tau (Scholl et al., 2016) pathology, and are thought to be in a “preclinical” stage of Alzheimer's disease. Examining older adults with and without evident Alzheimer's disease pathology is necessary to dissociate brain changes of aging from the earliest stages of Alzheimer's disease.

Aging and Alzheimer's disease are associated with distinct changes in cerebral metabolism. Alzheimer's disease is associated with a characteristic pattern of cerebral hypometabolism in angular gyrus, posterior cingulate, precuneus, temporal, and parietal regions (de Leon et al., 1983, Minoshima et al., 1997). This pattern is distinct from that seen in normal aging, which is associated with hypometabolism in prefrontal, precentral, perisylvian, and anterior cingulate cortices (Chetelat et al., 2013). The spatial pattern of hypometabolism is a reasonably sensitive biomarker for predicting future progression to Alzheimer's disease and can discriminate between normal aging, Alzheimer's disease, and other neurodegenerative diseases (Mosconi, 2005, Herholz et al., 2002). However, there is no consensus on changes in cerebral metabolism specific to preclinical Alzheimer's disease – while some studies detect hypometabolism (Drzezga et al., 2011, Lowe et al., 2014), other studies find hypermetabolism (Cohen et al., 2009, Oh et al., 2014), and others still find no differences in metabolism (Cohen et al., 2009, Altmann et al., 2015) associated with A $\beta$  in normal aging and mild cognitive impairment (MCI).

Cerebral metabolism may not only be useful as a biomarker – it could play a causal role in the development of Alzheimer's disease pathology (Bero et al., 2011, Jagust and Mormino, 2011, Mosconi, 2013). Although the spatial pattern of atrophy and hypometabolism largely overlap in Alzheimer's disease, there is marked regional variability in their interrelationship, which suggests that hypometabolism may precede atrophy and possibly even pathology (Chetelat et al., 2008). Sustaining high levels of metabolism may come at a cost (Bullmore and Sporns, 2012, Tomasi et al., 2013), the effects of which may be compounded across the lifetime (Jagust and Mormino, 2011) and induce vulnerability to A $\beta$  deposition (Vlassenko et al., 2010, Oh et al., 2016). Highly metabolically active areas of the brain tend to be more highly connected (Tomasi et al., 2013) and exhibit a distinct pattern of gene expression (Goyal et al., 2014) compared to areas of the brain with lower metabolic demand. Further study of cerebral metabolism across the lifespan and prior to the onset of clinical symptoms is necessary to understand the role of metabolic processes in aging and the development of Alzheimer's disease.

However, these approaches are restricted to investigating univariate increases or decreases in metabolism between groups, whereas multivariate approaches may be more sensitive for investigating the relationship between A $\beta$  and metabolism in the earliest stages of Alzheimer's disease. Researchers began looking at pairwise regional dependencies of glucose metabolism (Horwitz et al., 1984) near the advent of the use of [ $^{18}\text{F}$ ] fluorodeoxyglucose (FDG) to measure cerebral metabolic rate (Phelps et al., 1979). This approach has recently reemerged

and grown in popularity, reconsidered in a network framework that allows for the application of the mathematical tools of graph theory (Bullmore and Sporns, 2009). By investigating pairwise dependencies across the brain, network approaches extract a shared pattern of covariation over time in the case of fMRI (Salvador et al., 2005) and electrophysiological methods (Bassett et al., 2006, Stam et al., 2007) or across subjects in the case of PET (Horwitz et al., 1986, Sepulcre et al., 2013), structural MRI (He et al., 2007), and gene expression (Richiardi et al., 2015). Studies of brain networks have revealed important insights into the phenomena of healthy aging and progression to Alzheimer's disease, including reduced connectivity affecting the main intrinsic brain networks (ICNs) in healthy aging (Sala-Llonch et al., 2015), profound reductions particularly to the default mode network in Alzheimer's disease (Dennis and Thompson, 2014), and accelerated desegregation of brain networks from healthy aging to Alzheimer's disease (Brier et al., 2014a). However, potential reorganization of metabolic brain networks in aging and Alzheimer's disease progression remain poorly characterized.

Studies of metabolic brain networks, which measure co-variation in metabolism across individuals, complement univariate analyses of metabolism and other analyses of functional and structural brain networks. Metabolic brain networks are closely related to cortical thickness networks in that they estimate pairwise dependence of brain regions by examining correlations across individuals – just of metabolism measured by FDG PET, rather than cortical thickness measured by MRI (Alexander-Bloch et al., 2013). Early work on metabolic brain networks demonstrated age-related reductions of frontal-parietal metabolic correlations (Horwitz et al., 1986, Azari et al., 1992) and Alzheimer's-related reductions of metabolic correlation in frontal-parietal and homologous brain regions (Horwitz et al., 1987). More recent studies of MCI and Alzheimer's disease reported discrepant effects of ApoE genotype (Yao et al 2015, Carbonell et al., 2014) and reduced metabolic correlation associated with A $\beta$  in MCI (Carbonell et al., 2014). However, no studies have examined either (1) the joint effects of Alzheimer's disease risk factors (A $\beta$  and ApoE  $\epsilon$ 4) in cognitively normal older adults, which have confounded studies of network function during resting state fMRI in normal aging (Brier et al., 2014b), or (2) metabolic connectivity within- and between- canonical ICNs and graph theoretic properties of metabolic brain networks in cognitively normal aging. These gaps in knowledge obfuscate the link between metabolic brain networks and inquiries into aging, Alzheimer's disease progression, and brain network function in general.

It remains unclear whether Alzheimer's disease risk factors in cognitively normal older people will reflect a transitional stage between normal aging and Alzheimer's disease, if they will be indistinguishable from normal aging, or if they will demonstrate a unique profile of metabolic correlation. Using [ $^{11}\text{C}$ ] Pittsburgh compound B (PIB) -PET to divide cognitively normal subjects into groups based on A $\beta$  (PIB- for low and PIB+ for high A $\beta$  load) as well as ApoE genotype (ApoE  $\epsilon$ 4- and ApoE  $\epsilon$ 4+), we explore differences in properties of group metabolic brain networks using FDG-PET for young adults, subgroups of cognitively normal older adults, and patients with Alzheimer's disease.

## Materials and methods

### Participants.

The study examined 17 young adults, 64 cognitively normal older adults, and 22 patients with Alzheimer's disease. All participants completed MR and PET imaging, as well as genetic testing for ApoE ε4 carrier status using previously published methods (Agosta et al., 2009). Because the ε4 polymorphism of the apolipoprotein E gene (ApoE) is a major genetic risk factor for Alzheimer's disease (Corder et al., 1993, Schellenberg, 1995), we stratified subjects based upon the presence of this allele as well as their Aβ status. Prior to participation all subjects provided informed consent in accordance with the Institutional Review Boards at UC Berkeley, UC San Francisco, and Lawrence Berkeley National Laboratory.

Young adults and cognitively normal older adults were recruited from the community via newspaper advertisements as part of the Berkeley Aging Cohort (BAC) at UC Berkeley. Subjects were required to live in the community independently, without any major medical, neurological, and psychiatric illnesses that could influence cognition; young adults were 18 to 30 years old and old adults were at least 60 years old. All subjects had scores on the Mini Mental State Examination ≥ 26 and performance on memory tests within 1.5 standard deviations of age-adjusted norms. The study included all eligible young adults who underwent both MR and FDG-PET imaging and were Aβ negative on PIB-PET scanning. From the population of cognitively

Group Demographics						
	Young	Alzheimer's disease	Old PIB-ApoE4-	Old PIB-ApoE4+	Old PIB+ ApoE4-	Old PIB+ ApoE4+
# Subjects	17	22	16	16	16	16
Gender (Female / Male)	10 / 7	12 / 10	7 / 9	7 / 9	9 / 7	11 / 5
Age <sup>a</sup>	23.59±2.79 (20-30)	74.82±4.98 (69-89)	75.19±3.68 (71-84)	74.81±3.76 (71-83)	76.31±3.23 (70-80)	75.23±4.57 (69-89)
PIB Index <sup>b</sup>	0.98±0.04 (0.92-1.05)	1.62±0.25 (1.11-2.09)	1.01±0.03 (0.96-1.06)	1.00±0.08 (0.72-1.07)	1.26±0.14 (1.09-1.54)	1.37±0.24 (1.08-1.76)
# ApoE Carriers <sup>c</sup> (ε4+ / ε4-)	6 / 11	14 / 7	0 / 16	16 / 0	0 / 16	16 / 0
Years of Education	15.59±1.68 (12-20)	16.27±2.72 (12-22)	16.88±2.23 (12-20)	16.88±2.42 (12-20)	16.63±1.36 (14-20)	16.75±2.22 (12-20)
Scanner # ECAT / BIOGRAPH	13 / 4	15 / 7	11 / 5	8 / 7	8 / 8	7 / 9

**Table 1.** Participant demographics.

<sup>a</sup> Young group < Old groups and Alzheimer's disease group

<sup>b</sup> Young group and Old PIB- groups < Old PIB+ groups < Alzheimer's disease group

<sup>c</sup> Young group < Old ApoE ε4+ groups; Old ApoE ε4- groups < Old ApoE ε4+ groups and Alzheimer's disease group

normal older BAC participants meeting our criteria (N=141), we formed four subpopulations based on PIB status (PIB- or PIB+, see section 2.2.3) and ApoE ε4 carrier status (ApoE ε4- or ApoE ε4+), then identified the subgroup which included the fewest number of participants: those who were PIB- and ApoE ε4+ (N=16). Three other subgroups (PIB- ApoE ε4-, PIB+ ApoE ε4-, and PIB+ ApoE ε4+) were then each formed by individually selecting 16 participants that best matched the demographic characteristics of participants in the PIB- ApoE ε4+ group based on age, gender, and years of education.

Alzheimer's disease patients were recruited at the University of California San Francisco Memory and Aging Center. Alzheimer's disease diagnosis was based on a comprehensive multi-disciplinary evaluation (Kramer et al., 2003); patients met criteria for probable Alzheimer's disease (McKhann et al., 2011), were Aβ positive on PIB-PET scanning, and were without any major comorbid medical, neurological, and psychiatric illnesses.

A single set of Alzheimer's disease and young controls were examined throughout the study; older control subjects were initially separated only by PIB status. For the remainder of analyses, the cognitively normal older adults were divided into four subgroups (N=16) based on both PIB status and ApoE ε4 carrier status: Old PIB- ApoE ε4-, Old PIB- ApoE ε4+, Old PIB+ ApoE ε4-, and Old PIB+ ApoE ε4+ groups.

Table 1 shows the expected differences between groups in age, PIB index, and ApoE genotype based on group definitions. Two of the Alzheimer's disease participants were missing information – one did not undergo ApoE genotyping and another had an incomplete PIB scan and thus the PIB index could not be calculated but their Aβ positivity was confirmed through visual inspection by a clinician. We found no differences in gender and years of education between any of the groups, consistent with our sampling protocol.

#### MR Imaging acquisition and processing.

MR imaging of control subjects was performed at LBNL on a 1.5T Magnetom Avanto (Siemens Medical Systems) scanner using a 12 channel head coil. Structural scans were acquired axially using a high-resolution T1 MP-RAGE sequence (TR = 2110 ms; TE = 3.58 ms; TI = 1100 ms; flip angle = 15°; voxel dimension = 1.00 mm<sup>3</sup>; slice thickness = 1.00 mm with 50% gap).

MR imaging for Alzheimer's disease patients was performed at the Memory and Aging Center at UCSF on either a 1.5 T Siemens VISION System (N = 9) or 3 T Siemens Tim Trio (N = 13) scanner. Structural scans were acquired using high-resolution T1 MP-RAGE sequences, respectively acquired coronally with a quadra-core head coil (TR = 10 ms; TE = 7 ms; TI = 300 ms; flip angle = 15°; voxel dimension = 1.00 mm<sup>3</sup>; slice thickness = 1.40 mm with no gap) and axially with a 12-channel head coil (TR = 2300 ms; TE = 2.98 ms; TI = 900 ms; flip angle = 9°; voxel dimension = 1.00 mm<sup>3</sup>).

The T1 MRI data underwent anatomical tissue segmentation using Freesurfer v5.3 (<http://surfer.nmr.mgh.harvard.edu/>) to produce 80 cortical and subcortical regions of interest (ROIs) in each subject's native space based on the Desikan-Killiany atlas. The segmentation was coregistered to PET using an inverted transformation of the affine mapping between the mean PET image and the skull-stripped brain in Anatomical Normalization Tools (ANTs; <http://picsl.upenn.edu/software/ants/>).

### PET Imaging acquisition and processing.

PIB- and FDG-PET imaging were performed at LBNL (ECAT EXACT HR or BIOGRAPH Truepoint 6 PET scanners in 3D acquisition mode), enabling *in vivo* measurements of A $\beta$  and metabolism respectively. Imaging began with injection for 15-mCi of [ $^{11}\text{C}$ ] PIB, followed by 6 to 10-mCi of [ $^{18}\text{F}$ ] FDG at least 2-hours later and included a 10-minute transmission scan or an X-ray CT for attenuation correction. PIB-PET scanning began immediately upon injection, with dynamic acquisition frames obtained over 90-minutes (4 x 15 s, 8 x 30 s, 9 x 60 s, 2 x 180 s, 10 x 300 s, and 2 x 600 s). FDG-PET scanning began after 30-minutes of eyes-open quiet rest, with 6 x 5 minutes emission frames. Distribution volume ratio (DVR) images of PIB were produced by Logan graphical analysis with a cerebellar grey reference region. Standardized uptake value ratio (SUVR) images of FDG were produced with the pons as a reference region. Compared to other proposed FDG-PET reference regions, the pons has stable FDG tracer uptake across the aging and Alzheimer's disease spectrums (Minoshima et al., 1995). (For further details on PET acquisition and processing, see Wirth et al., 2013).

### PIB index.

A PIB index was computed for each subject as the mean DVR across prefrontal, lateral temporal, parietal, and cingulate cortices, and was then used to separate the cognitively normal older subjects into Old PIB- (PIB index < 1.08) or Old PIB+ (PIB index  $\geq$  1.08) groups (Mormino et al., 2012). This threshold has previously been validated versus post-mortem A $\beta$  burden (Villeneuve et al., 2015).

### Metabolic brain network generation.

Group metabolic brain networks were constructed for each group by computing Pearson's correlations of the FDG SUVR values across subjects between all pairs of ROIs. These correlations reflect relationships between brain regions across subjects, and are not based on canonical resting state networks but rather an approach used in graph theory in which the network reflects the interdependencies of all regions across the brain. FDG SUVR values were computed for each ROI by finding the mean SUVR value across all voxels within the ROI. This resulted in a fully weighted, symmetric 80 x 80 adjacency matrix for each group. The adjacency matrix was then converted to a fully weighted network, composed of 80 nodes (one for each ROI) and 3,240 undirected weighted edges (one for each pairwise correlation between two ROIs, i.e. the values in the adjacency matrix). See Appendix Table 1 for information about ROIs.

### Metabolic correlation strength.

To summarize the metabolic correlation strength for each group, we computed the average correlation between all ROIs in the metabolic brain network. Metabolic correlation strength was computed on Fisher's Z-transformed correlation data, which was then inverse transformed back to correlation values with a possible range from -1 to 1. We also computed metabolic correlation strength at the region level by averaging the strength of the correlations of each individual ROI with all other ROIs (Carbonell et al., 2014).

### Statistical testing.

All descriptive statistics and statistical testing were performed on Fisher's Z-transformed data. We conducted ANOVA with a family-wise error rate of 0.05 to test for group differences in analyses of demographic data and metabolic brain networks, followed by Tukey's HSD post-hoc test to examine pairwise differences between groups. We conducted chi-squared tests to test for group differences of dichotomous demographic data followed by pairwise differences between groups, adjusting the p-value using Bonferroni correction.

### Permutation testing of regional differences in correlation strength.

The statistical significance of differences in mean regional correlation strength between groups was estimated using permutation testing. We pooled subjects in the two groups under comparison, and then randomly assigned N subjects to the first group and the remaining subjects to the second group, extracting their FDG SUVR data to generate group metabolic brain networks. We then computed differences in mean regional correlation strength between the groups. Differences were computed on Fisher's Z-transformed data before being transformed back into correlations with a possible range from -1 to 1. We repeated this procedure 100,000 times, with the results used to estimate a 95% confidence interval of group differences. If the empirical value of the difference between groups lay outside the 95% confidence interval of differences produced by this random assignment procedure, then we rejected the null hypothesis and the empirical difference between the groups was deemed significant.

### Control for spatial proximity based on anatomical distance.

We computed the Chebyshev distance (the number of grey matter voxels that must be traversed to connect 2 points) between the centers of mass for each pair of ROIs using the Freesurfer average brain parcellation in MNI152 space. We computed the center of mass for each ROI using Chebyshev distance in a similar manner, by finding the voxel within each ROI that minimized the number of grey matter voxels that must be traversed to connect the voxel and all other voxels within the ROI. We deemed connections long-distance if the Chebyshev distance was above the median of all pairwise distances. We then employed statistical testing, as described in section 2.4.2 to compare group differences in metabolic correlation strength for only long-distance connections.

### Intrinsic connectivity network analysis.

Using the functional atlas proposed by Shirer and colleagues (2012), composed of 84 ROIs associated with 14 intrinsic connectivity networks (ICNs), we sought to compare features of metabolic correlations within- and between-ICNs derived from resting-state fMRI. The ICNs are composed of ROIs that functionally coordinate in the absence of evoked activity, i.e. during a "resting" scenario similar to that in which the participants engaged during the FDG-PET scan. To examine the metabolic correlations within- and between-ICNs, we used the approach described in section 2.3. to generate metabolic brain networks from the 84 ROIs in the functional atlas. We then computed the metabolic correlation strength within each ICN and between each pair of ICNs. We computed within-ICN correlation strength for a given ICN by calculating the average correlation strength of the connections between all ROIs within an ICN. Given two ICNs, we computed between-ICN correlation strength by calculating the average correlation strength of the connections between all ROIs in one ICN and all ROIs in the other ICN. As

described in section 2.4.1, metabolic correlation strengths were calculated by averaging Fisher's Z-transformed data, before inverse-transforming the data to correlation values between with a possible range of -1 to 1.

## Results

### Group differences in metabolic brain networks when normal older groups dichotomized by A $\beta$ .

*Qualitative differences in metabolic brain network correlation matrices.*

Adjacency matrices of the metabolic brain networks are shown in Fig. 1, revealing qualitative differences in the pattern of metabolic correlation strengths in the young, Alzheimer's disease, Old PIB-, and Old PIB+ groups, prior to splitting the cognitively normal older adults into four subgroups. The Young group exhibits the most heterogeneous pattern of correlations, with the strength of the correlations ranging from moderate negative correlations to strong positive correlations, and a combination of strong local (i.e. within-lobe) and distant (i.e. between-lobe)

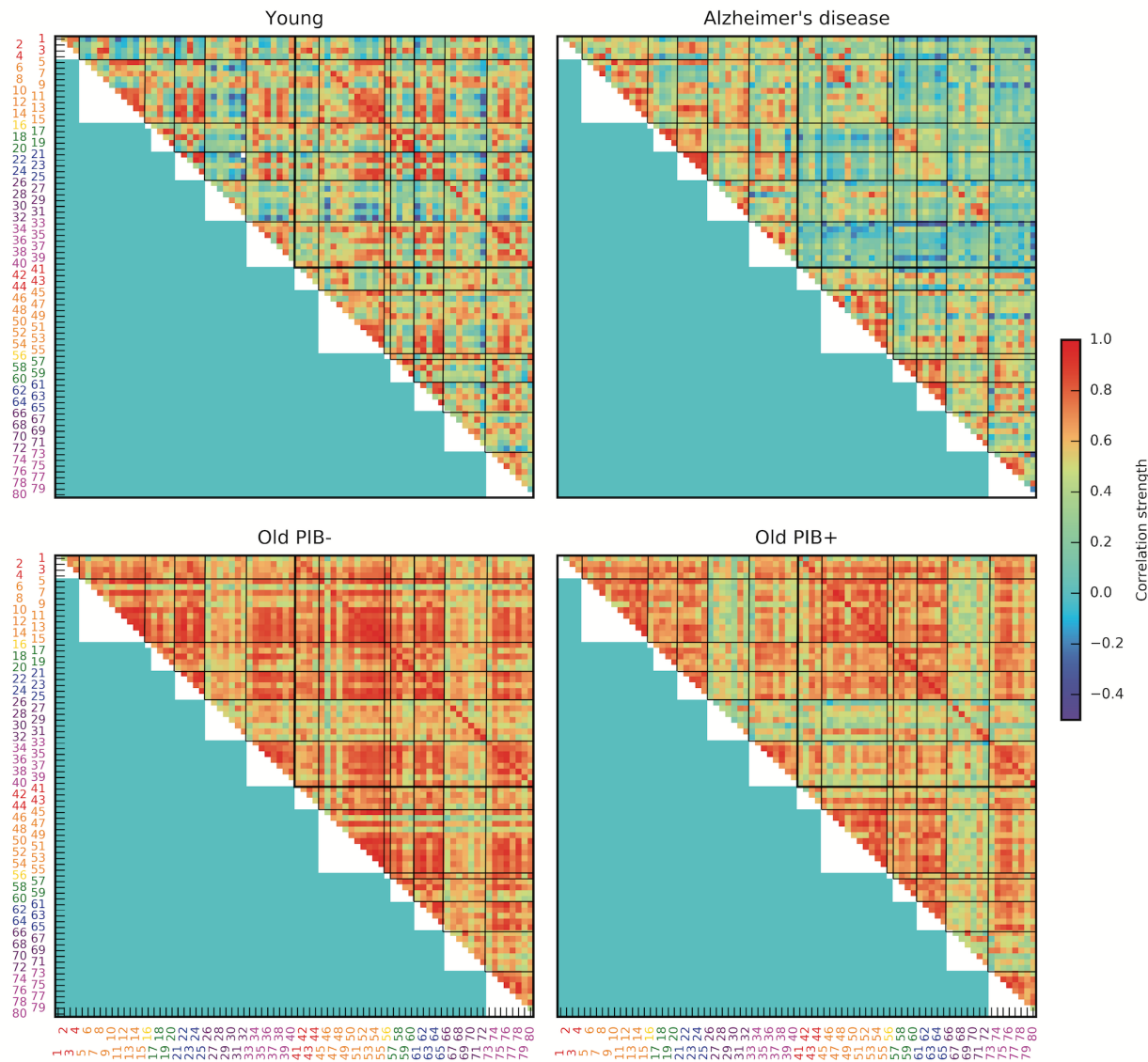


**Fig. 1:** Group metabolic adjacency matrices. Adjacency matrices are composed of pairwise correlation strength between all ROIs shown for young, Alzheimer's disease, Old PIB, and Old PIB+ groups. Regions of interest are numbered with label color corresponding to lobe membership: red=cingulate, orange=frontal, yellow=insula, green=occipital, blue=parietal, purple=subcortical, magenta=temporal.

associations. Although the Alzheimer's disease group also exhibits a relatively heterogeneous pattern of correlation strengths, a notable characteristic of the Alzheimer's disease group is reduction in correlation strength of homologous brain regions and between hemispheres (respectively the diagonal and off-diagonal of the upper right quadrant of the adjacency matrix in Fig. 1). Both the Old PIB- and Old PIB+ groups exhibit a homogenous increase in correlation strength across cortical (and to a lesser extent subcortical) ROIs relative to young adults and patients with Alzheimer's disease, with smaller increases in correlation strength in the Old PIB+ group.

#### *Mean metabolic correlation strength.*

The ANOVA examining group differences in mean metabolic correlation strength revealed a significant difference between the groups ( $F=1,159.01$ ,  $p<<1.00e^{-10}$ ,  $df=12,636$ ). The highest mean correlation strengths were seen in the Old PIB- group, followed by the Old PIB+, the young, and the Alzheimer's disease groups (Tukey's HSD post-hoc test FWE = 0.05).

#### Group differences in metabolic brain networks when normal older groups dichotomized by both A $\beta$ and ApoE 4 genotype.

#### *Qualitative differences in metabolic brain network correlation matrices.*

Adjacency matrices of the metabolic brain networks for older subjects defined by A $\beta$  and ApoE genotype are shown in Fig. 3. The Old PIB- ApoE  $\epsilon$ 4-, Old PIB- ApoE  $\epsilon$ 4+, and Old PIB+ ApoE  $\epsilon$ 4- groups all exhibit a similar homogeneous pattern of increased correlation strength between most cortical ROIs compared to the young and Alzheimer's disease groups in Fig. 1. This indicates that across subjects, the metabolic relationships between region-pairs are relatively consistent. However, the Old PIB+ ApoE  $\epsilon$ 4+ group exhibits a distinct, more heterogeneous pattern of correlation than other cognitively normal older adult subgroups, indicating that across all subjects, metabolism in one region inconsistently predicts metabolism in another region compared to other cognitively normal older adults. While the overall pattern of correlation strength may be dampened for the Old PIB+ ApoE  $\epsilon$ 4+ group relative to other subgroups of cognitively normal older adults, the reduced correlation strength of the Old PIB+ ApoE  $\epsilon$ 4+ group is particularly prominent in cingulate and temporal lobe ROIs.

#### *Mean metabolic correlation strength.*

The ANOVA examining group differences in mean metabolic correlation strength revealed a significant difference between the groups ( $F=1151.30$ ,  $p<<1.00e^{-10}$ ,  $df=18954$ , Fig. 2). The highest mean correlation strengths were seen in the Old PIB- ApoE  $\epsilon$ 4 -, Old PIB- ApoE  $\epsilon$ 4+, and PIB+ ApoE  $\epsilon$ 4- groups, which were not

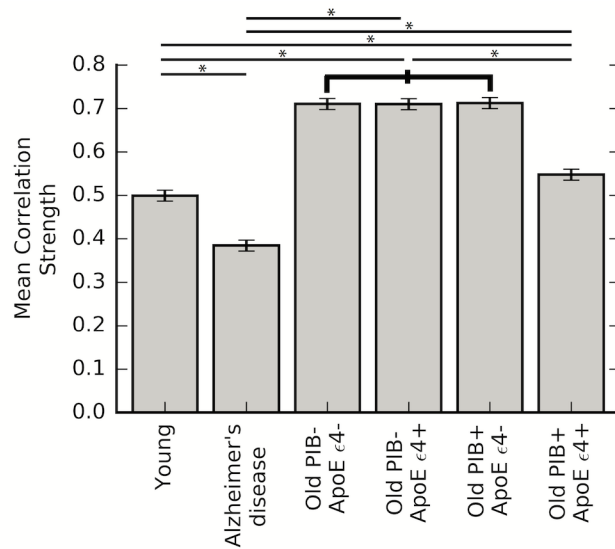


**Fig. 2:** Group differences in metabolic correlation strength. Error bars show the simultaneous confidence intervals from Tukey's HSD post-hoc test. \*  $p \leq 0.05$

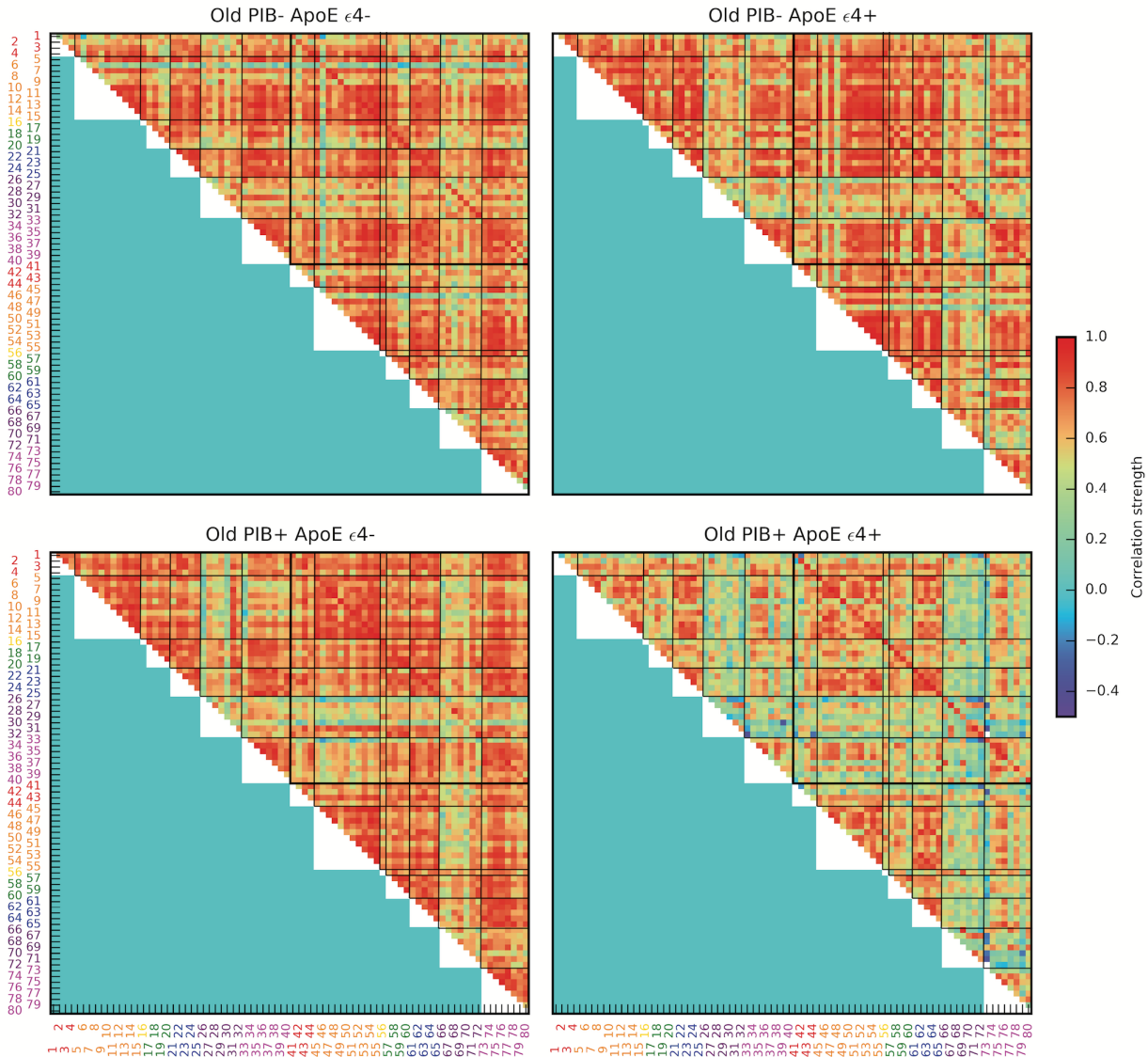


**Fig. 2:** Older subgroup metabolic adjacency matrices based on A $\beta$  and ApoE genotype. Adjacency matrices are composed of pairwise correlation strength between all ROIs shown for Old PIB- ApoE  $\epsilon 4-$ , Old PIB- ApoE  $\epsilon 4+$ , PIB+ ApoE  $\epsilon 4-$ , and Old PIB+ ApoE  $\epsilon 4+$  groups. Regions of interest are numbered with label color corresponding to lobe membership: red=cingulate, orange=frontal, yellow=insula, green=occipital, blue=parietal, purple=subcortical, magenta=temporal.

significantly different from one another, while all other groups differed (Tukey's HSD post-hoc test FWE = 0.05) (Fig. 3). The Old PIB+ ApoE  $\epsilon 4+$  group was intermediate in correlation strength between the young subjects and the other old subjects.

#### Mean regional metabolic correlation strength.

We examined the mean regional metabolic correlation strengths of each group's metabolic brain network by computing the average correlation strength of each ROI with all other ROIs. All groups exhibited relatively high correlation strengths in frontal, parietal, and lateral and superior temporal ROIs and relatively low strengths observed in medial temporal lobe, temporal pole, cingulate, and subcortical ROIs (Fig. 4). Young adults and Alzheimer's patients show distinct

patterns of regional metabolic correlation strength. Similar patterns of relative correlation strength emerged across the subgroups of older adults, although the PIB+ ApoE  $\epsilon$ 4+ subgroup appeared to be in an intermediary stage between normal aging and Alzheimer's disease.

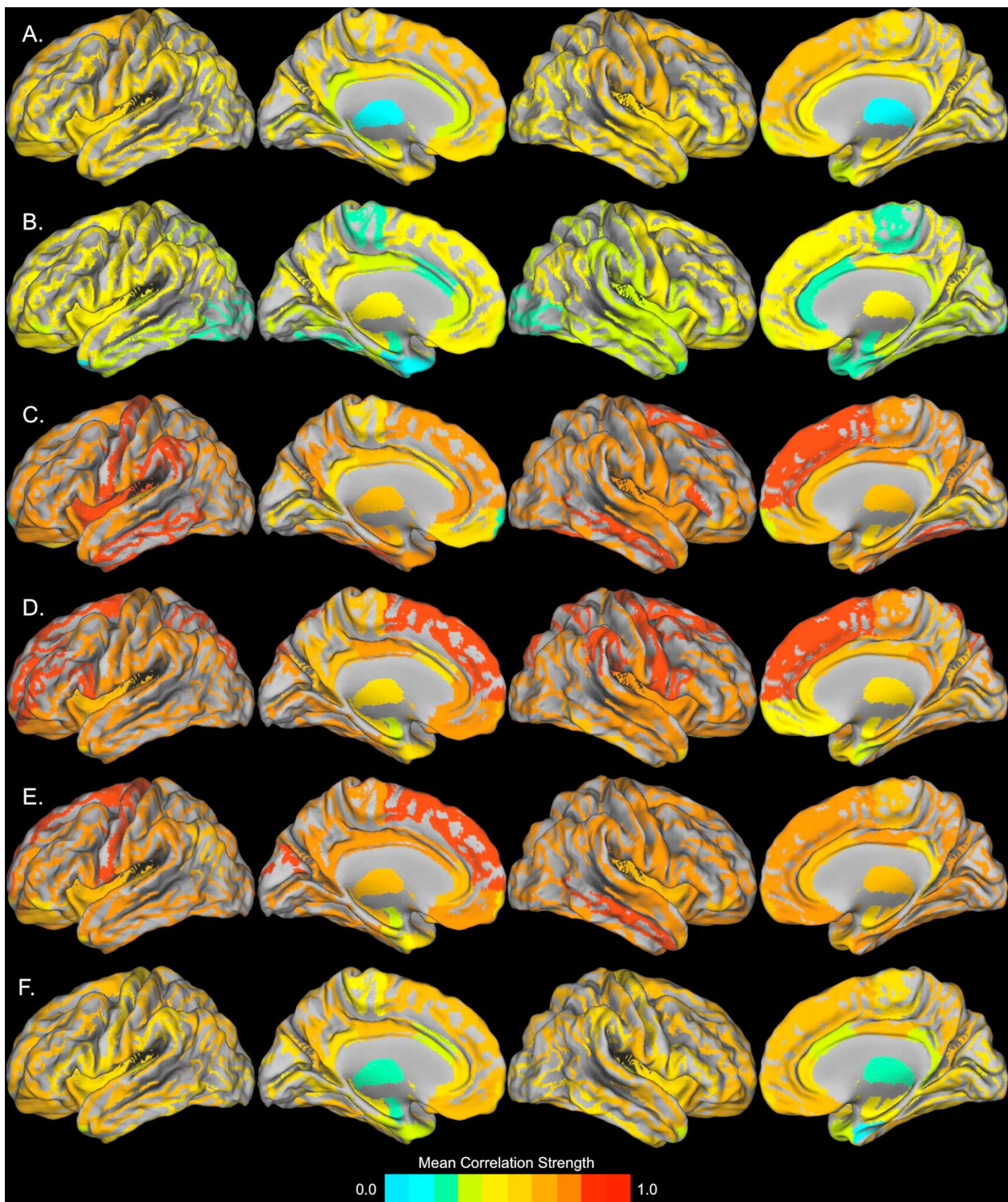


**Fig. 4:** Mean regional metabolic correlation strength for each group. **(A)** Young, **(B)** Alzheimer's disease, **(C)** PIB- ApoE  $\epsilon$ 4-, **(D)** PIB- ApoE  $\epsilon$ 4+. PIB+ ApoE  $\epsilon$ 4- **(E)**. PIB+ ApoE  $\epsilon$ 4+. Regions with high metabolic correlation strength are metabolic brain networks "hubs".

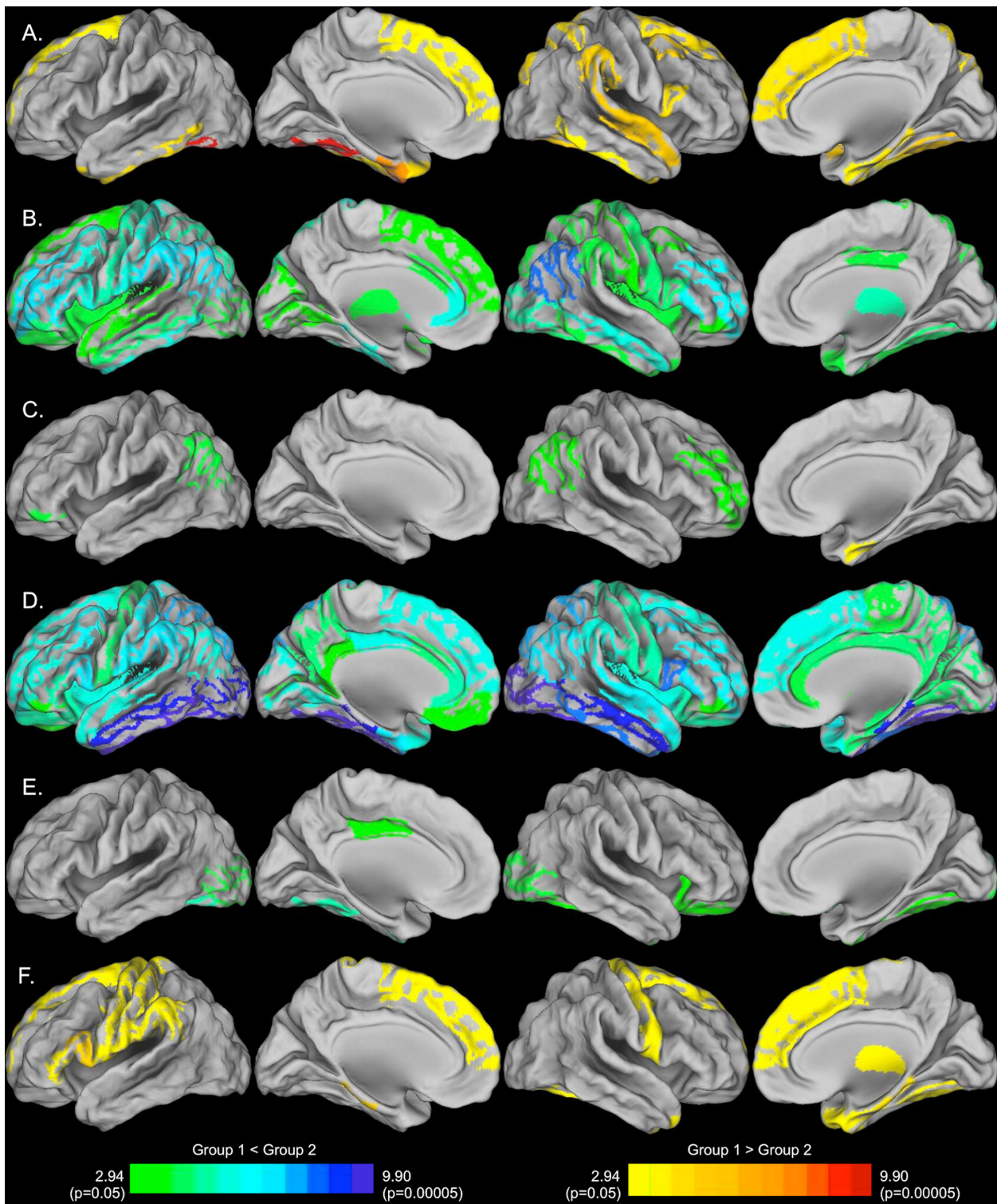


**Fig. 5:** Group differences in regional metabolic correlation strength. **(A)** Young > Alzheimer's disease (warm) and Young < Alzheimer's disease (cool) **(B)** Young > Other Old (warm) and Young < Other Old (cool) **(C)** Young > Old PIB+ ApoE ε4+ (warm) and Young < Old PIB+ ApoE ε4+ (cool) **(D)** Alzheimer's disease > Other Old (warm) and Alzheimer's disease < Other Old (cool) **(E)** Alzheimer's disease > Old PIB+ ApoE ε4+ (warm) and Alzheimer's disease < Old PIB+ ApoE ε4+ (cool) **(F)** Other Old > Old PIB+ ApoE ε4+ (warm) and Other Old < Old PIB+ ApoE ε4+ (cool). The significance of the difference between groups is indicated by the region's color as the logit of the uncorrected p-value obtained via permutation testing.

### Group differences in mean regional metabolic correlation strength.

We examined the topography of group differences in mean regional metabolic correlation strength using permutation testing (Fig. 5). Permutation testing revealed minimal differences between the Old PIB- ApoE ε4-, Old PIB- ApoE ε4+, and Old PIB+ ApoE ε4- groups. For this reason, we combined the results from these groups to simplify the analysis. This resulted in a comparison between the young, Alzheimer's disease, Old PIB+ ApoE 4ε+, and all other cognitively normal older subjects (i.e. "Other Old group", N=48).

The Young group differed profoundly from the Other Old group (Fig. 5 B) showing widespread reductions in correlation strength, but exhibited less extensive differences with the Alzheimer's disease group (Fig. 5 A) and the Old PIB+ ApoE ε4+ group (Fig. 5 C). Of interest, the Old PIB+ ApoE ε4+ group exhibited significant reductions relative to the Young group in right entorhinal cortex, and increases relative to the Young group in ROIs in the left pars orbitalis, right rostral middle frontal, and bilateral inferior parietal cortex. The Old PIB+ ApoE ε4+ showed relatively few differences with the Alzheimer's disease group (Fig. 5 E), but exhibited moderate differences with the Other Old group (Fig. 5 F). A notable commonality between the Old PIB+ ApoE ε4+ and the Alzheimer's disease groups is the low metabolic correlation strength in ROIs in the entorhinal cortex and medial temporal lobe compared to young and other old subjects.

### Control for spatial proximity.

Because partial volume effects of age- and disease-related atrophy may artificially inflate the metabolic correlation between spatially proximal regions (i.e. regions with short anatomical distance), we: (1) examined the relationship between the spatial proximity and correlation strength for all pairs of regions and (2) performed statistical testing for group differences in mean metabolic correlation strength on only long-distance connections that eliminate any shared effect of spatial proximity on correlation strength.

The Alzheimer's disease group demonstrated substantial decay in correlation strength with increasing anatomical distance ( $R=-0.52$ ,  $p<<1.00e^{-10}$ ), and a small but significant negative relationship was also found in the Young ( $R=-0.07$ ,  $p=3.45e^{-5}$ ), Old PIB- ApoE ε4- ( $R=-0.09$ ,  $p=4.38e^{-7}$ ), and Old PIB+ ApoE ε4- ( $R=-0.11$ ,  $p=8.51e^{-10}$ ) groups. No relationship was found in the Old PIB+ ApoE ε4+ group and a small but significant positive relationship was found in the

Old PIB+ ApoE ε4- group ( $R=0.05$ ,  $p=0.007$ ). Group differences in mean correlation strength persisted even after examining only long-distance connections ( $F=927.24$ ,  $p<<1.00e^{-10}$ ,  $df=9348$ ), where Tukey's HSD post-hoc test revealed significant differences between all groups except the Old PIB- ApoE ε4- with the Old PIB- ApoE ε4+ and Old PIB+ ApoE ε4- groups. The overall pattern of relative metabolic correlation strengths was identical to those reported in section 3.2.2.

### Intrinsic connectivity network connectivity.

For each group we examined the relationships within (diagonal) and between (off-diagonal) ICNs (Fig. 6). Unlike the previously presented graphical whole brain approach, this approach was designed to specifically test the expectation that the dependency of metabolic rate between regions should be greater for regions within the same ICN compared with regions outside of the ICN.

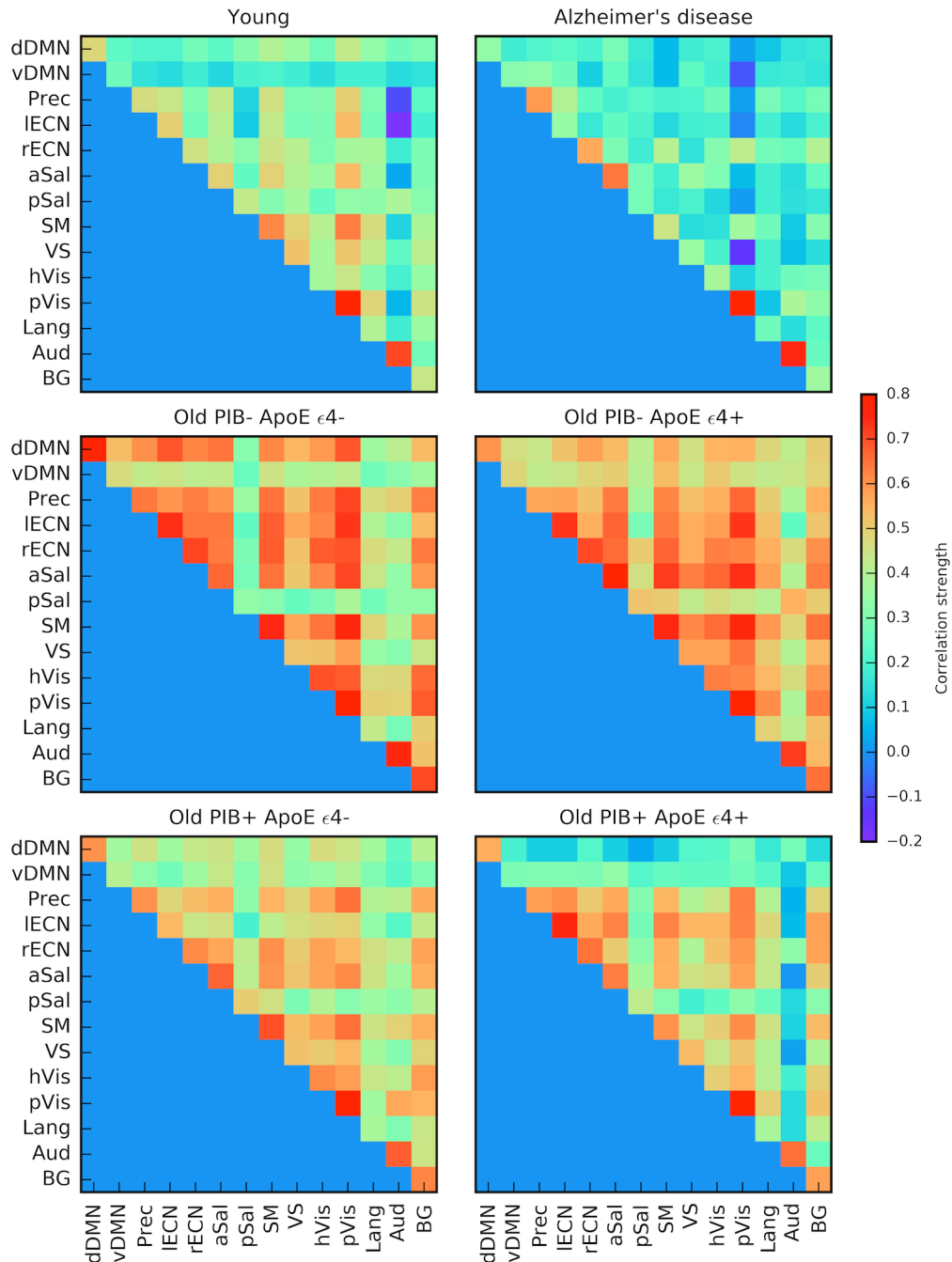


**Fig. 6:** Intrinsic connectivity networks metabolic correlation strengths for each subgroup. Metabolic correlation strengths shown within- (diagonal) and between- (off-diagonal) intrinsic connectivity networks. dDMN=dorsal Default Mode Network, vDMN=ventral Default Mode Network, Prec=Precuneus, IECN=left Executive Control Network, rECN=right Executive Control Network, aSal=anterior Salience, pSal=posterior Salience, SM=sensorimotor, VS=Visuospatial, hVis=high Visual, pVis=primary Visual, Lang=Language, Aud=Auditory, BG=Basal Ganglia

Examination of mean correlation within and between ICNs revealed clear qualitative distinction between the metabolic brain networks of young and Alzheimer's disease groups; high correlations for the Alzheimer's disease group were largely restricted to within-ICN associations, whereas the young group exhibited high correlations within most ICNs as well as a rich pattern of high and low correlations between ICNs. Both of the older PIB+ subgroups also exhibited

high correlations within most ICNs and a diverse pattern of correlations between ICNs, which generally showed more between-ICN correlations than seen in the young or Alzheimer's disease patients and fewer between-ICN correlations than the PIB- subgroups. The PIB+ ApoE4+ between-ICN metabolic correlations were weaker than seen in the PIB+ ApoE4- group. The Old PIB- subgroups exhibited a homogeneous pattern of widespread high correlations both within and between most ICNs. Interestingly, some of the most striking differences between the older subgroups were lower between-ICN metabolic correlation strengths between the dorsal DMN and the other ICNS in the older PIB+ subgroups compared with the older PIB- subgroups.

## Discussion

We examined metabolic brain networks of young adults, patients with Alzheimer's disease, and four subgroups of cognitively normal older adults based on the presence or absence of two Alzheimer's risk factors: A $\beta$  deposition and the ApoE  $\epsilon 4$  allele. Cognitively normal older adults exhibited widespread high metabolic correlation strength compared to young and Alzheimer's disease subjects. The extent of elevated metabolic correlation was reduced in the subgroup with both A $\beta$  and ApoE  $\epsilon 4$  genotype (Fig. 2) and in PIB+ older subgroups generally (Fig. 1). By comparison, young adults and patients with Alzheimer's disease both had lower mean metabolic correlation strength than cognitively normal older adults, with the metabolic correlation strength of Alzheimer's patients being somewhat lower than that of young adults. The pattern of metabolic dependencies across the brain differed between young adults, Alzheimer's patients, older adults with both A $\beta$  and ApoE  $\epsilon 4$  genotype, and other older adults.

We also examined metabolic brain network correlations within- and between- canonical resting state ICNs identified using resting-state fMRI by Shirer and colleagues (2012). These ICNs reflect sub-networks of ROIs that functionally couple at rest and underlie subject-driven cognitive states. Young adults showed relatively high metabolic correlation strength within ICNs and a rich pattern of varied metabolic correlation strengths between ICNs. In contrast, Alzheimer's patients showed a dramatic reduction in correlation strength between ICNs. PIB- older adults showed homogeneous high metabolic correlation strength both within and between ICNs. PIB+ older adults appeared to be intermediary to Alzheimer's patients and PIB- older adults, exhibiting similar within- and between-network correlation patterns to the young subjects. These findings identified previously undescribed alterations in metabolic networks in aging, Alzheimer's disease, and those at the highest Alzheimer's disease risk.

Metabolic brain networks, which reflect the co-variation in metabolism across individuals, should be interpreted differently than previously reported univariate analyses of metabolism and other analyses of functional brain networks. For example, while Alzheimer's patients may be hypometabolic in two ROIs compared to young adults (Fig. 7 A), the relative metabolism in one ROI compared to the other may be preserved (Fig. 7 B and C) – demonstrating the presence of a univariate group difference, but not a bivariate difference between groups in these ROIs. Alternately, while the metabolic rate may be indistinguishable across subgroups of older adults in two ROIs (Fig. 7 D), the groups may demonstrate different patterns of linear dependence between the two ROIs (Fig. 7 E and F) – demonstrating the presence of a bivariate group difference, but not a univariate difference between groups. Thus, significant univariate results do not imply significant bivariate results, and vice versa. Moreover, unlike functional brain networks, which utilize fluctuations in brain activity over time, metabolic brain networks utilize fluctuations in metabolism across individuals to infer dependence of metabolism in ROIs (Fig. 7 C and F). High metabolic correlations are consistent with low individual variability in the relative metabolism between brain regions (i.e. "metabolic homogeneity" across individuals), such that metabolism in one region can be used to infer metabolism in another region due to a consistent linear relationship in relative metabolism across individuals. Low metabolic correlations are consistent with high individual variability in the dependency of metabolism between brain regions (i.e. "metabolic heterogeneity" across individuals), such that metabolism in one region cannot be used to infer metabolism in another region due a lack of a consistent linear relationship across individuals. These separate ways of

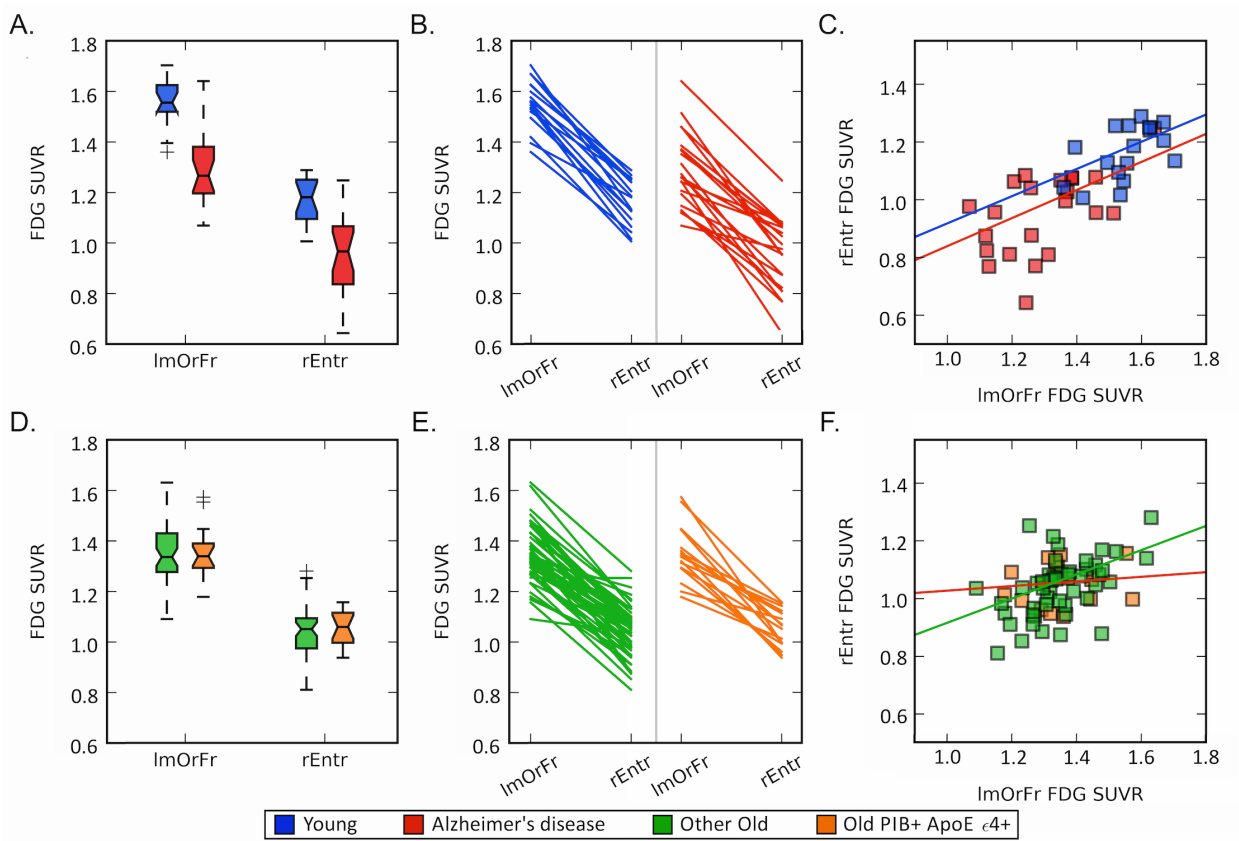


**Fig. 7:** A closer look at univariate versus bivariate relationships.\* (A) Boxplots of the distribution of FDG SUVR values for young adults and patients with Alzheimer's disease in two ROIs (ImOrFr = left medial orbitofrontal, rEntr = right entorhinal) reveals univariate differences in FDG SUVR between groups (Young > Alzheimer's disease) and between ROIs (left medial orbitofrontal > right entorhinal). (B) Difference in FDG SUVR values between ROIs for individual participants. Each line segment represents one young adult (blue) or patient with Alzheimer's disease (red). This demonstrates a similar bivariate metabolic relationship between the two ROIs across participants. (C) Scatter plot of the relationship between FDG SUVR values for two ROIs. Each point represents one participant. A regression line shows the relationship of FDG SUVR between the ROIs for each group. The linear relationship of FDG SUVR between the ROIs suggests that metabolism from one ROI predicts metabolism in the other ROI across all of the subjects in the analysis; there is a linear dependence of metabolism between these ROIs across subjects, and both young adults and patients with Alzheimer's disease demonstrate this similarly. Young  $R^2 = 0.54$ , Alzheimer's disease  $R^2 = 0.55$  (D) Boxplots of the distribution of FDG SUVR values for Old PIB+ ApoE ε4- and Old PIB+ ApoE ε4+ in two ROIs. This reveals no univariate differences in FDG SUVR for either ROI between groups. (E) Difference in FDG SUVR values between ROIs. Each line segment represents one older adult. This demonstrates group differences in the bivariate metabolic relationship between the two ROIs. (F) Scatter plot of the relationship between FDG SUVR values for two ROIs. Each point represents one participant. Regression line shows the relationship of FDG SUVR between the ROIs for each group. The linear relationships differ between groups; metabolism from one ROI predicts metabolism from the other ROI for the PIB+ ApoE ε4- group, but not for the PIB+ ApoE ε4+ group since that group does not demonstrate a consistent dependence in metabolism between the ROIs. Old PIB+ ApoE ε4-  $R^2 = 0.67$ , Old PIB+ ApoE ε4+  $R^2 = 0.13$ . \* This example was specifically selected to explain how univariate and bivariate results can differ within the same data, and is not necessarily representative of the dataset as a whole.

exploring group differences provide distinct insights into the underlying processes of aging and Alzheimer's disease in the brain.

Metabolic brain networks share commonalities with cortical thickness networks, both of which examine covariance between brain regions across subjects. In such networks positive correlations indicate that both ROIs are either increasing or decreasing consistently across subjects, negative correlations indicate that one ROI is increasing and the other is decreasing consistently across subjects, and near-zero correlations indicate inconsistency in the relative rates of the ROIs across subjects. Decreased structural covariance within the DMN has been reported

in older adults and patients with MCI and Alzheimer's disease (Spreng and Turner, 2013, Montembeault et al., 2016), however other brain networks were also disrupted and reflected an inverted-U pattern consistent with maximal segregation of functional networks in young adults followed by dedifferentiation in old age (DuPre and Spreng, 2017). Disruption is more exaggerated in patients with Alzheimer's disease (Montembeault et al., 2016) and in ApoE ε4 carriers (Spreng and Turner, 2013). Patients with Alzheimer's disease further exhibited increased local interregional correlations and disrupted long distance correlations (Yao et al., 2010), and altered graph theoretic properties (He et al., 2008, Yao et al., 2010). Our findings in metabolic brain networks of Alzheimer's patients mirror those reported in cortical thickness networks, however the widespread elevation of correlation strength, as we found in metabolic brain networks of older adults, was a divergent finding from previous reports of reductions in correlation strength for cortical thickness networks of older adults. Thus, metabolism may undergo a more homogenous pattern of change in older adults, compared to a more heterogeneous pattern of atrophy across individuals. Importantly, studies of cortical thickness networks in older adults have not accounted for the effects of Aβ. Exploration of preclinical Alzheimer's pathology on cortical thickness networks in old age would further clarify the relationship between the processes of atrophy and metabolic change, which have shown evidence of divergence in univariate studies (Ibanez et al., 1998, Chetelat et al., 2008, La Joie et al., 2012, Grothe et al., 2016, Kljajevic et al., 2014).

Widespread elevations in correlation strength of metabolic brain networks observed in cognitively normal older adults suggest a novel phenomenon in aging – metabolic homogeneity. Previous work posited that weaker metabolic correlation strength in Alzheimer's disease reflects "metabolic heterogeneity" due to variability in compensatory and/or degenerative process that lead to inter-individual variability in metabolism (Carbonell et al., 2014, Sanabria-Diaz et al., 2013). We found the opposite effect – very strong metabolic correlation strength – in cognitively normal older adults, which would be consistent with "metabolic homogeneity". Interestingly, this homogeneity must be occurring despite the presence of age-related compensatory and degenerative processes. As white matter integrity typically decreases in old age, the pervasive metabolic "hyper-connectivity" observed in the present study does not reflect increased structural connectivity between brain regions. Rather, this phenomenon may reflect dedifferentiation that occurs with age-related loss of aerobic glycolysis (Goyal et al., 2017), functional connectivity (Geerligs et al., 2015), white matter integrity (Andrews-Hanna et al., 2007, Saenger et al., 2017), and BOLD variability (Garrett et al., 2011) that negatively affect dynamic exploration of functional brain states (McIntosh et al., 2010, Deco et al., 2011). Our finding that reduction of correlations was related to further anatomical distance in two of the normal older groups (section 3.4) may be consistent with white matter alterations leading to metabolic homogeneity. Further work is needed to explore age-related metabolic homogeneity, including its potential relationship with aerobic glycolysis, functional connectivity, white matter alterations, and other measures of brain structure and function, as well as the effects of deviation from this old age-related metabolic correlation profile on brain function and degeneration.

Metabolic homogeneity may be a form of "dedifferentiation", an age-related process previously posited in light of reductions in hemispheric asymmetry (Dolcos et al., 2002), loss of functional specialization (Park et al., 2004), and reduced task-related deactivation (Prakash et al., 2012). Age-related dedifferentiation was further confirmed by our ICN analysis, which revealed widespread high between-ICN metabolic correlation strength in cognitively normal older adults, indicative of desegregation. This was true across all subgroups of older adults, regardless of Aβ

and ApoE status, although desegregation was greater in older subgroups without A $\beta$  compared to those with A $\beta$  which may be indicative of divergent process of aging and Alzheimer's disease. Segregation of the brain into functionally specialized subnetworks is a key organizational feature of structural and functional brain networks that supports differentiation of brain function (Chen et al., 2008, He et al., 2009). Studies in other modalities have also demonstrated age-related desegregation of brain networks (Chen et al., 2011, Geerligs et al., 2015), as well as step-wise decreases in segregation with Alzheimer's disease severity (Brier et al., 2014a). Overall, widespread elevated metabolic correlation was consistent with a profound loss of independence in metabolism across brain systems in normal aging, leading to dedifferentiation and desegregation of metabolism.

Individuals possessing both A $\beta$  and the ApoE  $\epsilon 4$  genotype appeared to be on an altered metabolic trajectory compared to other cognitively normal older adults without both risk factors. Because the network correlation pattern of this group was intermediate between young and Alzheimer's disease patients, and quite different from their normal old-aged peers, the altered trajectory could represent either preservation of youth-like function or the start of decline towards Alzheimer's disease. While the latter seems more likely, increased neural activity that might be associated with persistence of youth-like metabolic function has been proposed as an underlying mechanism linking ApoE genotype, A $\beta$ , and aging (Jagust and Mormino, 2011, Oh et al., 2016). However, the relatively low metabolic correlation strength in the entorhinal cortex and temporal lobe – regions that exhibit marked neurodegeneration in Alzheimer's disease (Du et al., 2001) as well as neurodevelopmental differences in early life (Shaw et al., 2007) – bore intriguing similarity to the Alzheimer's group (Fig. 3 and Fig. 4). Moreover, prior work demonstrating an interaction of A $\beta$  and ApoE  $\epsilon 4$  genotype in healthy older adults reported lower cognitive performance (Kantarci et al., 2012) and faster rates of cognitive decline (Mormino et al., 2014) only in subjects with both risk factors. Various mechanisms may make ApoE  $\epsilon 4$  carriers more vulnerable to the toxic effects of A $\beta$ , including alterations in tau phosphorylation, neuroinflammation, mitochondrial function, synaptic function, and/or neurodevelopmental differences in cortical thickness and connectivity (Wolf et al., 2013, Brown et al., 2009). However, another possibility is that individuals with both risk factors were further along the Alzheimer's disease continuum, given the younger age of onset of Alzheimer's disease in patients with ApoE  $\epsilon 4$  genotype (Corder et al., 1993).

Due to the plurality and diversity of age-related processes, the study of aging is rife with confounding variables and ultimately it is beyond the scope of any single study to address all of these challenges. The major limiting factor of the present study was the small number of subjects. We attempted to control for spurious results by confirming consistency using permutation testing, which helped protect against individual subject or a subset of subjects having undue influence on the results, and conducted some analyses on a larger group (i.e. Other Old, N=48) composed of all older adults except those in the PIB+ ApoE  $\epsilon 4+$  group (which remained lower powered at N=16). The limited number of subjects precluded the use of partial correlations to control for additional variables. However, we were able to match subgroups for sex, years of education, and, when appropriate, age. While brain atrophy and partial volume effects consequent to the relatively low resolution of PET will increase regional metabolic covariance, this did not seem likely to explain the pattern of results (see section 3.4). Moreover, atrophy was unlikely to explain opposite effects on metabolic correlation strength: elevated metabolic correlation strength in cognitively normal older adults, but reduced metabolic correlation strength in Alzheimer's patients. We conducted the analysis using fully-connected

weighted graphs for each group, and thus our results should not be directly compared with studies using binary graphs or partially-connected (i.e. thresholded) graphs, as well as graphs generated from other neuroimaging modalities. However, our results suggested that there may be significant differences in the appropriate “connection density” (i.e. number of edges in a graph) between groups, providing a strong case against the use of binary graphs or graphs thresholded based on connection density when examining age- and disease-related differences in metabolic brain networks (and possibly other neuroimaging modalities as well). We recognize that glucose metabolism is a complex phenomenon reflecting multiple metabolic processes (Zimmer et al., 2017). Nevertheless, it is clearly related to synapse structure and function as well as measures of brain function and connectivity using multiple modalities (Riedl et al., 2014, Tomasi et al., 2013, Rocher et al., 2003, Goyal et al., 2014).

### Conclusion.

Metabolic brain networks revealed distinct effects of aging and Alzheimer’s disease risk on metabolic processes in cognitively normal older adults. We identified a previously undescribed process of widespread elevated metabolic correlation in aging, which disrupted the segregation of ICNs across the brain. Moreover, we demonstrated that the metabolic brain network of normal older adults with both A $\beta$  and ApoE  $\epsilon$ 4 genotype differed substantially from that of their normal old-aged peers without both risk factors, possessing a pattern of metabolic correlations that is more similar to that of young adults and Alzheimer’s disease patients. Analysis based on ICNs further distinguished PIB+ from PIB- older adults, showing greater dedifferentiation in PIB- subgroups and a profile more similar to Alzheimer’s patients in PIB+ subgroups. The effect of dual Alzheimer’s risk factors appeared to be much more prominent when examining metabolic brain networks than the weak and inconsistent effects identified using other approaches, suggesting that the alterations captured by metabolic brain networks may be especially important for understanding cognitive decline and progression to Alzheimer’s disease. While the clinical applications of these results are unclear, the findings of alterations in metabolic networks that differ significantly in aging and those at high risk of Alzheimer’s disease may motivate the exploration of these effects in the further search for biomarkers and mechanisms important in the earliest stages of Alzheimer’s disease.

## Chapter 3

### Early-life metabolic inefficiency predicts late-life amyloid- $\beta$ topology

#### Abstract

Alzheimer's disease exhibits a characteristic spatiotemporal pattern of amyloid- $\beta$  plaques (A $\beta$ ) and neurofibrillary tangles (tau); the reasons for their varied concentrations across the brain remain unknown. To focus on the topologies of A $\beta$  and tau before they are widely distributed throughout the brain, we examined PIB-PET (N=138) and AV1451-PET (N=59) in cognitively normal older adults (ages 65-93). To examine the effects of lifespan brain activity on vulnerability to Alzheimer's disease pathology, we used measures of brain function in young adults (ages 20-41) – specifically brain regions showing high connectivity (hubs) estimated from rs-fMRI (N=100), glucose metabolism from FDG-PET (N=42), and a novel metric “metabolic inefficiency” – to predict the topologies of A $\beta$  and tau in healthy aging. We found that hubs did not explain the topology of A $\beta$  or tau pathologies in healthy aging. However, metabolic inefficiency strongly predicted the topology of A $\beta$  ( $R=0.525$ ,  $p<<e^{-100}$ ), with metabolically inefficient brain areas harboring 10 % more A $\beta$  than efficient regions. Although metabolic inefficiency significantly predicted the topology of tau ( $R=0.255$ ,  $p<<e^{-100}$ ), we demonstrated that this relationship was driven by correlation of tau with A $\beta$ , failing to explain tau pathology in the medial and inferior temporal lobe. While the exact cause of vulnerability of metabolically inefficient brain areas to A $\beta$  remains to be determined, we provide evidence that tissue metabolic factors, unrelated the role of glucose in sustaining brain connectivity, explains the topology of A $\beta$  in healthy aging.

## Introduction

Alzheimer's disease (AD) pathology exhibits a stereotyped spatiotemporal pattern across the brain. Tau initially appears in entorhinal and other medial temporal areas before spreading to association cortex (Braak and Braak, 1995), whereas A $\beta$  predominantly accumulates in prefrontal, lateral temporal, parietal, and cingulate cortices (Klunk et al., 2004). It remains unclear whether tau and A $\beta$  spread transsynaptically from epicenters, or whether specific aspects of regional vulnerability drive the distribution of each pathology in a multifocal manner (Thal et al., 2002, Grothe et al., 2017, de Calignon et al., 2012, Lowe et al., 2018). While there is ongoing work characterizing the spatiotemporal topology of AD pathology, we have little understanding of the etiology of A $\beta$  and tau – specifically, why particular brain areas are more or less susceptible to A $\beta$  and tau early in the course of the disease. Differences in the topology of A $\beta$  and tau in the initial stages of AD suggest that distinct factors contribute to their susceptibility.

Prior work suggests that patterns of regional connectivity or “hubness” (Buckner et al., 2009), glucose metabolism (Oh et al., 2016), and aerobic glycolysis (Vlassenko et al., 2010) across the healthy young brain closely overlap with the topology of A $\beta$  deposition in AD. Each of these factors implicates a different aspect of regional tissue bioenergetics. However, unraveling the relative contributions of these physiologic properties to AD pathology is challenging due to their complex interdependencies: aerobic glycolysis contributes to measurements of glucose metabolism (Fox and Raichle, 1986) and hubs experience elevated glucose metabolism and aerobic glycolysis (Bullmore and Sporns, 2012). Furthermore, metabolism and hubs share other physiologic properties (Newberg et al., 2005, Vaishnavi et al., 2010, Liang et al., 2013). The relationship of these measures to synaptic activity, which has been shown to release A $\beta$  in animal models (Bero et al., 2011), may drive the link between metabolism and hubs – a theory backed by computational models of “activity-dependent degeneration” (de Haan et al., 2012). However, this does not explain the link between early-life aerobic glycolysis and A $\beta$ , since aerobic glycolysis does not appear to support neural activity (Lin et al., 2010, Goyal et al., 2014) and is diminished in normal aging (Goyal et al., 2017).

While our ability to measure tau deposition *in vivo* is a relatively recent development, correlates of tau topology in the human brain remain elusive. The extent to which tau pathology overlaps with hubness, cerebral metabolism, aerobic glycolysis, and other sources of vulnerability linked to A $\beta$  remain unexplored. However, because of their different patterns of deposition across the brain, it seems likely that distinct mechanisms lead to A $\beta$  and tau pathologies. Theories about the origins of tau pathology differ from those suggested for A $\beta$ ; rather than metabolic features of tissue, tau deposition is proposed to reflect neuroplasticity failure (Mesulam, 1999) or high information processing load fueled by cascading network failure (Jones et al., 2017).

AD develops over the course of decades (Price et al., 1999); by the time clinical symptoms of the disease appear, AD pathology is already widespread throughout the brain (Braak and Braak, 1991). To provide insight into the etiology of A $\beta$  and tau pathologies we focused on the earliest stages of AD progression by examining the topologies of A $\beta$  and tau in cognitively normal, healthy older adults. To gain insight into the features of typical, healthy brain function that induce vulnerability to AD pathology, we compared the topologies of features of brain function in early-life with the topologies of AD pathology in late-life. Our approach of examining brain function in early-life was consistent with examining the effects of lifespan brain activity on vulnerability to AD pathologies (Jagust and Mormino, 2011, Jagust, 2013). By

examining the topologies of hubs and glucose metabolism in younger adults, we avoid the chicken-and-egg problem created by concurrent changes in brain structure and function and accumulation of AD pathology in late life (Sheline and Raichle, 2013). We specifically focused on comparing the predictive power of the early life topologies of hubs, glucose metabolism, and a novel metric “metabolic inefficiency” (which reflects metabolism exceeding that predicted by degree centrality) in explaining the topologies of A $\beta$  and tau in late-life.

## Materials and methods

### Participants.

We utilized MRI and PET data from the Berkeley Aging Cohort Study (BACS), the IMAP study (Imagerie Multimodale de la maladie d'Alzheimer à un stade Précoce, Caen, France) and the Human Connectome Project (HCP). Cerebral glucose metabolism was measured using FDG-PET in young and middle-aged adults (20 to 41 years old) that participated in BACS (N=13) and IMAP (N=29). Resting-state fMRI was measured in similarly aged adults (22 to 36 years old) from HCP (N=100). A $\beta$  was measured in older adults (65 to 91 years old) using PIB-PET from BACS (N=138). Tau was measured in a subset of the older adults (71 to 93 years old) from BACS (N=59) using AV1451-PET. All participants across facilities underwent structural MRI. Genotype (N=8) and education (N=6) information were missing for a small subset of BACS subjects. See Table 1 for participant demographics.

	<b>rs-fMRI (HCP) (N=100)</b>	<b>FDG-PET (BACS/IMAP) (N=42)</b>	<b>PIB-PET (BACS) (N=138)</b>	<b>AV1451-PET (BACS) (N=59)</b>
<b>Age</b>	29 (22-36)	28 (20-41)	76 (65-91)	79 (70-93)
<b>Sex (% female)</b>	54%	45%	57%	56%
<b>Education (years)</b>	14 (11-17)	14 (9-20)	17 (12-20)	17 (12-20)
<b>Apoe ε4 Carriers</b>	n/a	25% (N=40)	30% (N=131)	37%
<b>PIB Index</b>	n/a	n/a	1.10 (0.71-1.76)	1.17 (0.95-1.85)
<b>Braak Stage</b>	n/a	n/a	n/a	Stage 0: N=13; Stage 1: N=38; Stage 2: N=8
<b>PET Scanner</b>	n/a	ECAT (N=10); Biograph (N=3); Discovery (N=29)	ECAT (N=89); Biograph (N=49)	Biograph (N=59)

**Table 1:** Participant demographics. Values represent means and (range).

### BACS PET and MR imaging acquisition.

For all BACS participants, PET and MR imaging were performed at Lawrence Berkeley National Laboratory.

#### *PET.*

PET imaging was performed on either an ECAT EXACT HR or BIOGRAPH Truepoint 6 scanner in 3D acquisition mode. For each PET scan a 10-min transmission scan or X-ray CT was obtained for attenuation correction.

PET data were reconstructed using an ordered subset expectation maximization algorithm with a 4mm Gaussian smoothing kernel, weighted attenuation correction, and scatter correction. The resulting resolution of the image was 6.5 x 6.5 x 7.25 mm<sup>3</sup>.

[<sup>11</sup>C]PIB was synthesized at LBNL Biomedical Isotope facility using a previously published protocol (Mathis et al., 2003); approximately 15-mCi of [<sup>11</sup>C]PIB was injected into an antecubital vein. PIB-PET scanning began immediately upon injection, with dynamic acquisition

frames obtained over 90-minutes as follows: 4 x 15 s, 8 x 30 s, 9 x 60 s, 2 x 180 s, 10 x 300 s, and 2 x 600 s.

[<sup>18</sup>F]AV1451 was synthesized at LBNL Biomedical Isotope facility; approximately 10-mCi of [<sup>18</sup>F]AV1451 was injected. Data from 80-100 min post injection were used to construct tissue ratios (SUVRs) using an inferior cerebellar gray matter reference region (Baker et al., 2017).

[<sup>18</sup>F]FDG was purchased from a commercial vendor (IBA Molecular, Morgan Hill, CA); 6 to 10-mCi of [<sup>18</sup>F]FDG was injected. During [<sup>18</sup>F]FDG tracer uptake, subjects rested quietly in a dimly lit room. FDG-PET scanning began 30-minutes following injection, consisting of six 5-min emission frames.

#### *MRI.*

To aid preprocessing and tissue segmentation of the PET data, anatomical MR imaging was performed on a 1.5T Magnetom Avanto (Siemens Medical Systems) scanner using a 12-channel head coil. Anatomical MRI scans were acquired axially using a high-resolution T1 MP-RAGE sequence (TR = 2110 ms; TE = 3.58 ms; TI = 1100 ms; flip angle = 15°; voxel dimension = 1.00 mm<sup>3</sup>; slice thickness = 1.00 mm with 50% gap).

#### IMAP PET and MR imaging acquisition.

For all IMAP participants, PET and MR imaging were performed at the Cyceron Center (Caen, France).

#### *PET.*

PET imaging was performed on a Discovery RX VCT 64 PET-CT scanner. For each PET scan a transmission scan was acquired for attenuation correction. The PET scanner had an image resolution of 5.22 x 5.22 x 5.78 mm (measured using the Nema Nu2-2001 standard) and images were reconstructed without smoothing with a voxel size of 1.95 x 1.95 x 3.2 mm. Approximately 180-MBq of [<sup>18</sup>F]FDG was injected. During [<sup>18</sup>F]FDG tracer uptake, subjects rested quietly in a dark environment. At 50-min post-injection a 10-min FDG-PET acquisition scan was acquired.

#### *MRI.*

To aid preprocessing and tissue segmentation of the PET data, MR imaging was performed on a Philips Achieva 3T MRI scanner using an 8-channel head coil. Anatomical MRI scans were acquired sagittally using a high-resolution 3D T1 fast field echo sequence (TR = 20 ms; TE = 4.6 ms; flip angle = 20°; voxel dimension 1.00 mm<sup>3</sup>; slice thickness = 1.00 mm with no gap).

#### HCP MR imaging acquisition.

For all HCP participants, MR imaging was acquired as part of the Washington University-Minnesota Consortium HCP (Van Essen et al., 2013) and accessed using the ConnectomeDB database (Marcus et al., 2011). Participants were selected from the “100 Unrelated Subjects” subset of the “500 Subjects” HCP release. MR imaging was performed on a modified Siemens Skyra 3T MRI scanner using a 32-channel head coil. Resting-state fMRI scans were acquired over 14-minutes and 30-seconds with a multiband gradient-EPI sequence (TR = 720ms, TE = 33.1 ms, multiband factor = 8; flip angle = 52°; voxel dimension = 2 mm<sup>3</sup>, number of slices = 72,

multiband acceleration factor = 8, see Ugurbil et al., 2013). Data were collected over 2 d. Detailed description of the resting-state fMRI data collection can be found elsewhere (Smith et al., 2013).

#### IMAP and BACS anatomical MRI processing.

All anatomical MRIs were collected a maximum of 426 days (median: 14 days) from the PET scan. Anatomical MRIs were linearly coregistered to a template to straighten or, for non-baseline MRIs, were coregistered to the baseline MRI. Each anatomical MRI underwent tissue segmentation using Freesurfer v5.3 (<http://surfer.nmr.mgh.harvard.edu/>) to produce regions of interest (ROIs) in each subject's native space based on the Desikan-Killiany atlas. The segmentation was coregistered to the PET data using an inverted transformation of the affine mapping between the mean PET image and the skull-stripped brain in Anatomical Normalization Tools (ANTS; <http://picsl.upenn.edu/software/ants/>). The Freesurfer segmentation was used for PET processing.

#### IMAP and BACS PET processing.

Frames within the first 5 minutes of PIB-PET data were summed, and all frames including the summed image were realigned to the middle frame. The cerebellar grey matter ROI from Freesurfer was used as a reference region for Logan graphical analysis on frames corresponding to 35- to 90-minutes post-injection, which produced PIB distribution volume ratio (DVR) images.

All frames of FDG-PET data were realigned to the first frame for each subject. We computed the sum of the frames, and then intensity normalized the data by the mean value of the pons to produce standardized uptake value (SUVR) images. We manually extracted the pons based on the brainstem ROI from Freesurfer. Images with incomplete coverage of the pons were excluded from the study. To achieve the same image resolution across PET imaging centers of  $6.5 \times 6.5 \times 7.25 \text{ mm}^3$ , the SUVR data from Caen were smoothed with a  $3.873 \times 3.873 \times 4.377 \text{ mm}^3$  Gaussian kernel using SPM12.

The AV1451 frames were realigned to the first frame for each subject. We computed the mean uptake 80-100 minutes post-injection, and then intensity normalized the data by mean inferior cerebellar grey matter uptake to obtain SUVR images (Baker et al., 2017). We created the inferior cerebellar grey ROI using the reverse-normalized SUIT template (see Baker et al., 2017 for more detail).

We warped the DVR/SUVR images to the MNI 152 2-mm template using ANTS and downsampled to 4-mm voxels using FSL. To obtain group brainmaps of the average topology of each tracer (FDG, PIB, and AV1451) for use in the analyses, we computed the average SUVR or DVR value for each voxel across subjects. We used the fsaverage from Freesurfer, downsampled to 4mm voxels from MNI 152 2 mm space, to restrict analyses to cortical voxels. Restriction to cortex should minimize the effects of off-target binding of AV1451 to subcortical brain areas.

#### HCP rs-fMRI processing.

The rs-fMRI scans underwent the HCP minimal processing pipeline (Glasser et al., 2013) with global signal regression. We warped the rs-fMRI scan to the MNI 152 2 mm template using ANTS and then downsampled to 4 mm voxels using FSL. We used the fsaverage from Freesurfer, downsampled to 4mm voxels from MNI 152 2 mm, space, to restrict analyses to

cortical voxels. Restriction to cortex should maximize signal-to-noise in the HCP multiband sequence (Barch et al., 2013).

### Graph construction.

Using the rs-fMRI data for each HCP participant, we computed the Pearson's correlation over time between each pair of voxels. This resulted in an adjacency matrix of 15,970 x 15,970 voxels, equivalent to a fully connected weighted graph with 15,970 nodes. To create binary graphs consistent with those generated by Buckner and colleagues (2009), we thresholded each adjacency matrix at a cost of 0.25 to preserve the top 25% of edges.

### Node centrality.

For each individual subject, we computed degree centrality for each node (i.e. voxel) by summing the number of edges of each node with all other nodes using the subject's binary graph. We then z-scored the degree centrality values for each subject. To ensure consistency of results, the analyses were repeated for fully weighted graphs, for which we estimated correlation strength by computing the average Fischer-transformed correlation of each node with all other nodes and then inverse transforming back to ensure range of -1 to 1.

### Consensus maps.

We created consensus maps to represent the average topologies of our measures. For the PET data, we used the SUVR and DVR maps for each subject to compute the average SUVR and DVR maps in the sample. We created a metabolism consensus map, representing the average FDG SUVR of each voxel in the young BACS and IMAP samples. We created an A $\beta$  consensus map and a tau consensus map, respectively representing the average PIB DVR and the average AV1451 SUVR of each voxel in the older BACS samples. We also created a hub consensus map, representing the average z-scored degree centrality of each voxel in the young HCP sample.

To improve the generalizability of our results, we validated the analyses using the Buckner hub consensus map of degree centrality in 127 young subjects, provided to us by Buckner and colleagues (2009). The data were downsampled to 4mm voxels using FSL. Analyses were restricted to cortical voxels in fsaverage from Freesurfer.

### Linear regression model of centrality on metabolism.

To model the relationship between the hub consensus map and the metabolism consensus map, we used the topology of degree centrality to predict the topology of metabolism via linear regression (using the sklearn function `linear_model.LinearRegression` in Python):

$$y = \beta_0 + \beta_1 x + \varepsilon$$

Where  $y$  is a vector [FDG SUVR<sub>1</sub>, ..., FDG SUVR<sub>n</sub>] representing the average metabolism in young adults for each voxel,  $x$  is a vector [degree<sub>1</sub>, ..., degree<sub>n</sub>] representing voxels average degree centrality in young adults for each voxel,  $\varepsilon$  is a vector of the errors [ $\varepsilon_1$ , ...,  $\varepsilon_n$ ], with  $n$  total voxels representing a different point in 3D space on the brain, not a different individual.

To obtain an unbiased estimate of each voxel's metabolism, given the topology of metabolism and degree centrality in the rest of the brain, for each voxel we removed the voxel and its neighbors from  $x$  and  $y$  before performing the linear regression. We used this approach, which is conceptually similar to leave-on-out cross validation from machine learning (Norman et al., 2006, Haynes et al., 2015, Cole et al., 2016) to reduce the influence of spatial

autocorrelations on the predictions (Kiebel et al., 1999). Then, we computed the predicted metabolism ( $\hat{y}_i$ ) for each voxel  $i$ :

$$\hat{y}_i = b_0 + b_1 x_i$$

Where  $b_0$  and  $b_1$  are the fitted values of  $\beta_0$  and  $\beta_1$  and  $x_i$  is the degree centrality of the voxel from the hub consensus map.

To measure what we call the “metabolic inefficiency” of each voxel, we subtracted the metabolism predicted by the model for each voxel ( $\hat{y}_i$ ) from the observed metabolism ( $y$ ) of the voxel from the metabolism consensus map. This is equivalent to the residual error ( $\epsilon_i$ ) of the model.

### Removing shared variance of A $\beta$ and tau.

In addition to naïve examination of the distributions of A $\beta$  and tau in healthy older adults, we sought to determine whether any associations with A $\beta$  and with tau were driven by their shared variance. To examine independent features of the topologies of A $\beta$  and tau, we removed their shared variance. To estimate A $\beta$  independent from tau, we use the residual A $\beta$  after performing a linear regression of tau on A $\beta$  using their consensus maps. Residual A $\beta$  is equivalent to the error of the model and represents independent A $\beta$  decorrelated from tau. We performed the complementary procedure to estimate tau independent from A $\beta$ .

### Statistical analysis.

We examined differences in AD pathology between metabolically efficient and inefficient voxels as well as between hubs ( $>$  mean degree centrality) and non-hubs ( $\leq$  mean degree centrality). We conducted a t-test to assess statistical significance between the two sets of voxels. We employed a bootstrap procedure to estimate the mean and confidence interval of differences in AD pathology. For the bootstrapping procedure, with each iteration we selected N random subjects (A $\beta$ : N=138; tau: N=59) with replacement and created a bootstrapped consensus map of AD pathology and calculated the percent difference in AD pathology:

$$\frac{\left| \sum_{i \in set_1} AD \text{ pathology}_i - \sum_{j \notin set_1} AD \text{ pathology}_j \right|}{\left( \frac{\sum_{i \in set_1} AD \text{ pathology}_i + \sum_{j \notin set_1} AD \text{ pathology}_j}{2} \right)} * 100$$

Where  $set_1$  is a set of nodes (e.g. set of all metabolically efficient voxels or set of all hubs), N is the number of elements in set 1, and 15,970 is the total number of voxels. We repeated this procedure 500 times, and then calculated the mean and the 95% confidence interval from the bootstrapped values.

To provide a continuous estimate, we compared the topologies of the early-life predictors with late-life AD pathology by calculating the Pearson’s correlation of the consensus maps:

$$R = \frac{\sum_{i=1}^{15,970} (x_i - \bar{x})(y_i - \bar{y})}{\sqrt{\sum_{i=1}^{15,970} (x_i - \bar{x})^2} \sqrt{\sum_{i=1}^{15,970} (y_i - \bar{y})^2}}$$

Where X is the early-life predictor (e.g. the hub consensus map or metabolic inefficiency), Y is late-life AD pathology (e.g. A $\beta$  or tau consensus map), and  $i$  is a voxel in the consensus map (not an individual).

## Results

### Linear regression of degree centrality on metabolism.

The results of the linear regression of degree centrality on metabolism using the hub and the metabolism consensus maps in the younger adults are shown in Fig. 1 A and B. Consistent with previously published work, we found a significant dependence of metabolism on degree centrality ( $R^2=0.284\pm0.0007$ ,  $p<<e^{-100}$ ), with voxels with higher degree centrality tending to have higher metabolic rate. This supports the intuition that it is energetically demanding to sustain high levels of connectivity with the rest of the brain.

### Metabolic inefficiency associated with elevated AD pathology in healthy aging.

We hypothesized that areas of the brain that are metabolically inefficient in early-life are more susceptible to A $\beta$  deposition in late-life. To examine this, we dichotomized all voxels according to whether or not they were metabolically efficient or metabolically inefficient. In the linear model of degree centrality on metabolism, the regression line (Fig. 1 B) represents the predicted metabolism given degree centrality. We used predicted metabolism to calculate the residual error (i.e. the difference between actual and predicted metabolism), which we call “metabolic inefficiency”. We designated “metabolically efficient” any voxels that were less metabolic than predicted by the model (i.e. with a negative residual, below the regression line in Fig. 1 B). We designated “metabolically inefficient” any voxels that were more metabolic than predicted by the model (i.e. with a positive residual, above the regression line in Fig. 1 B). To test the hypothesis that areas of the brain that are metabolically inefficient in early-life are more susceptible to AD pathology in late-life, we compared the amount of AD pathology in metabolically inefficient versus efficient brain areas.

We calculated the average PIB DVR in the older adults for voxels that were metabolically inefficient versus voxels that were metabolically efficient. Using a t-test, we found significantly higher PIB DVR in areas of the brain that were metabolically inefficient in early-life compared to those areas that were metabolically efficient ( $t=44.627$ ;  $p<<e^{-100}$ , Fig. 1 C). Bootstrapping revealed that inefficient brain areas had an average PIB DVR 10.847% [10.186%, 11.558%] higher than efficient brain areas. This suggests that brain areas with higher metabolic rate than predicted by their degree centrality in early-life are more susceptible to A $\beta$  deposition in late-life. This effect of metabolic efficiency was seen regardless of the voxel’s degree centrality – even a brain area with low degree centrality was likely to be associated with higher A $\beta$  if it was metabolically inefficient, whereas a brain area with high degree centrality was likely to be associated with lower A $\beta$  if it was metabolically efficient.

We ran a parallel analysis to examine whether areas of the brain that are metabolically inefficient in early-life are also more susceptible to tau deposition in late-life, effectively allowing us to compare how specific early-life predictors are for A $\beta$  deposition versus tau. Using a t-test, we found significantly higher AV1451 SUVR in areas of the brain that are metabolically inefficient in early-life ( $t=16.531$ ;  $p<e^{-61}$ , Fig. 1 D). Bootstrapping revealed that inefficient brain areas had an AV1451 SUVR approximately 2.937% [2.308%, 3.633%] higher than efficient brain areas. This suggests that brain areas with higher metabolic rate than predicted by their degree centrality in early-life are more susceptible to tau in preclinical AD, a similar pattern as we observed for A $\beta$ . However, it is notable that the effect for tau was much smaller than that found for A $\beta$ .

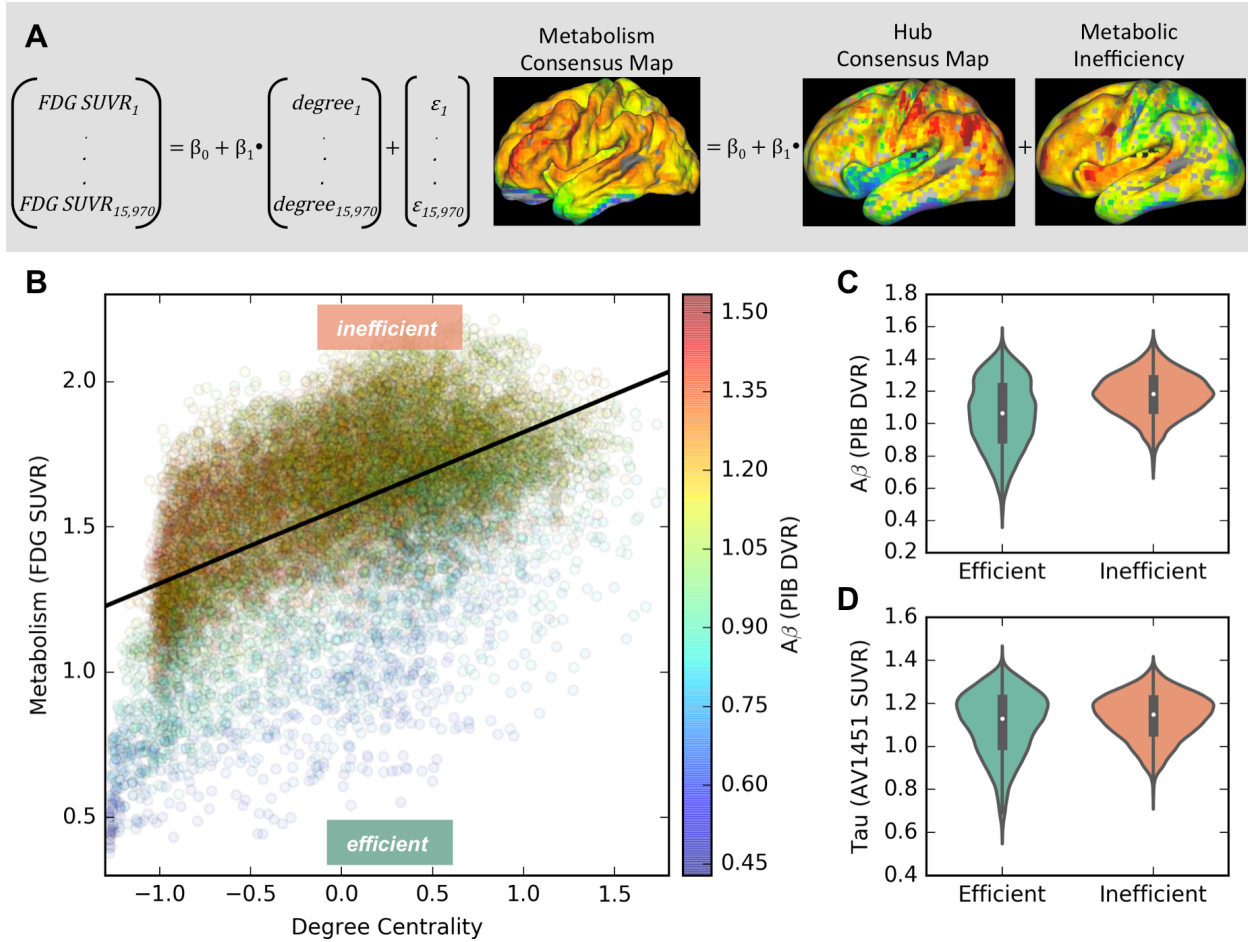


**Fig. 1:** Linear regression of degree centrality on metabolism. **(A)** Linear regression model of degree centrality on glucose metabolism from the hub consensus map and the metabolism consensus map of the average younger adult. **(B)** Scatter plot showing the degree centrality (x-axis) and FDG SUVR (y-axis), respectively from the hub consensus map and the metabolism consensus map. Each point is a different voxel, with a total of 15,970 voxels. To show the relationship between metabolic inefficiency and A $\beta$ , the color of each point corresponds to the PIB DVR from the A $\beta$  consensus map of the average older adult. Points above the regression line are considered metabolically inefficient (i.e. more metabolic than predicted by degree centrality). Points below the regression line are considered metabolically efficient (i.e. less metabolic than predicted by degree centrality). Selecting the voxels that were metabolically efficient or inefficient in the average young adult, we then examine whether AD pathology in the average older adult differs between voxels that were efficient or inefficient in early-life. Violin plots with an embedded box plot showing the distribution of **(C)** A $\beta$  pathology (PIB DVR)\* and **(D)** tau pathology (AV1451 SUVR)\*\* in voxels that were inefficient (orange) or efficient (teal) in early-life. \* ( $p < e^{-100}$ ) \*\* ( $p < e^{-61}$ )

#### AD pathology in not elevated in hubs in healthy aging.

We hypothesized that areas of the brain that are hubs in early-life are more susceptible to A $\beta$  deposition in late-life. To examine this, we dichotomized all voxels according to whether or not they were hubs (i.e. degree centrality  $>$  mean degree centrality). Then we calculated the average PIB DVR in the older adults for hubs versus non-hubs. Using a t-test, we found significantly lower PIB DVR in hubs compared to non-hubs ( $t = -14.505$ ;  $p < e^{-47}$ , Fig. 2 A). Bootstrapping revealed that hubs had an average PIB DVR 3.711% [3.212%, 4.245%] lower than non-hubs. This suggests that hubs are not more susceptible to A $\beta$  deposition in healthy aging.

We ran a parallel analysis to examine whether hubs in early-life were more susceptible to tau deposition in late-life. We calculated the average AV1451 SUVR in the older adults for

voxels that were hubs versus non-hubs. Using a t-test, we found significantly lower AV1451 SUVR in hubs compared to non-hubs ( $t=-33.672$ ;  $p<<e^{-100}$ , Fig. 2 B). Bootstrapping revealed that hubs had an average AV1451 SUVR 5.865% [4.923%, 6.768%] lower than non-hubs. This suggests that hubs are not more susceptible to tau deposition in healthy aging.

#### A $\beta$ and tau topologies in healthy aging.

We compared the distributions of A $\beta$  and tau from consensus maps in the average older adult (Fig. 3 A and B), observing substantial correlation of A $\beta$  and tau ( $R^2=0.522$ ). Some of the similarities in the topologies of A $\beta$  and tau included spared primary sensory cortices and elevations in prefrontal cortex, precuneus, and aspects of the parietal and superior lateral temporal lobes. Notably, many of these elevations were more pronounced for A $\beta$  and would be considered relatively low for tau (Maass et al., 2017). However, there are also critical points of discrepancy in the topologies of A $\beta$  and tau, including the orbitofrontal cortex and medial/inferior temporal lobe, which exhibited high tau and low A $\beta$ , as well as the anterior cingulate, which exhibited high A $\beta$  and low tau.

Given the substantial overlap of the topologies of A $\beta$  and tau in older adults, we sought to examine the independent relationship of A $\beta$  and of tau with early-life brain activity by regressing out their shared variance (Fig. 3 C and D, see “Removing shared variance of A $\beta$  and tau” in Materials and Methods). This approach allowed us to examine whether or not the observed associations of A $\beta$  or tau with features of early-life brain activity were driven by their shared variance.

#### Comparing topologies of early-life predictors with AD pathology in healthy aging.

To gain a qualitative sense of the differences in overlap of the early-life predictors with late-life AD pathology, we visually compared the topologies of consensus maps of degree centrality and metabolic inefficiency in early-life (Fig. 3 E and F) with the topologies of consensus maps of A $\beta$  and tau in healthy aging (Fig. 3 A and B). We found that the topology of metabolic inefficiency compared to degree centrality better tracked A $\beta$  in a number of brain areas: lateral and especially medial prefrontal cortex as well as precuneus/posterior cingulate. Only in occipital cortex, which was not especially vulnerable to A $\beta$ , and lateral parietal cortex did the topology of degree centrality better track A $\beta$ . The topology of degree centrality better tracked tau in the parietal lobe. Notably, tau in the inferior and medial temporal cortex was poorly predicted by both degree centrality and metabolic inefficiency.

We found a strong positive correlation of early-life metabolic inefficiency ( $R=0.525$ ,  $p<<e^{-100}$ ) with late-life A $\beta$  deposition and a positive correlation of early-life metabolic inefficiency ( $R=0.255$ ,  $p<<e^{-100}$ ) with late-life tau. We found a weak, negative correlation of early-life degree centrality ( $R=-0.09$ ,  $p<e^{-30}$ ) with late-life A $\beta$  deposition and a negative correlation of degree centrality ( $R=-0.282$ ,  $p<<e^{-100}$ ) with late-life tau. We validated these findings using the hub consensus map from Buckner and colleagues (2009), which confirmed

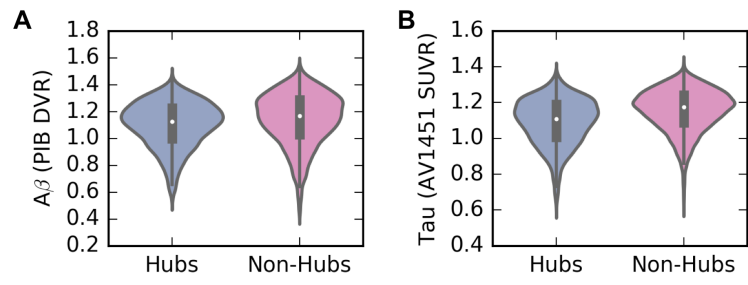


**Fig. 2:** Comparison of AD pathology in hubs vs non-hubs. Violin plots with an embedded box plot showing the distribution of (A) A $\beta$  pathology (PIB DVR) for the A $\beta$  consensus map \* and (B) tau pathology (AV1451 SUVR) from the tau consensus map\*\* in hubs (blue) versus non-hubs (pink). \* ( $p<<e^{-47}$ ) \*\* ( $p<<e^{-100}$ )

that while A $\beta$  may be elevated in hubs in patients with AD, this relationship did not extend to A $\beta$  ( $R=-0.18$ ,  $p<<e^{-100}$ ) or tau ( $R=-0.21$ ,  $p<<e^{-100}$ ) in healthy aging.

Due to the substantial overlap of A $\beta$  and tau, we also examined the relationship of degree centrality after decorrelating A $\beta$  and tau. This allowed us to examine whether the relationship of

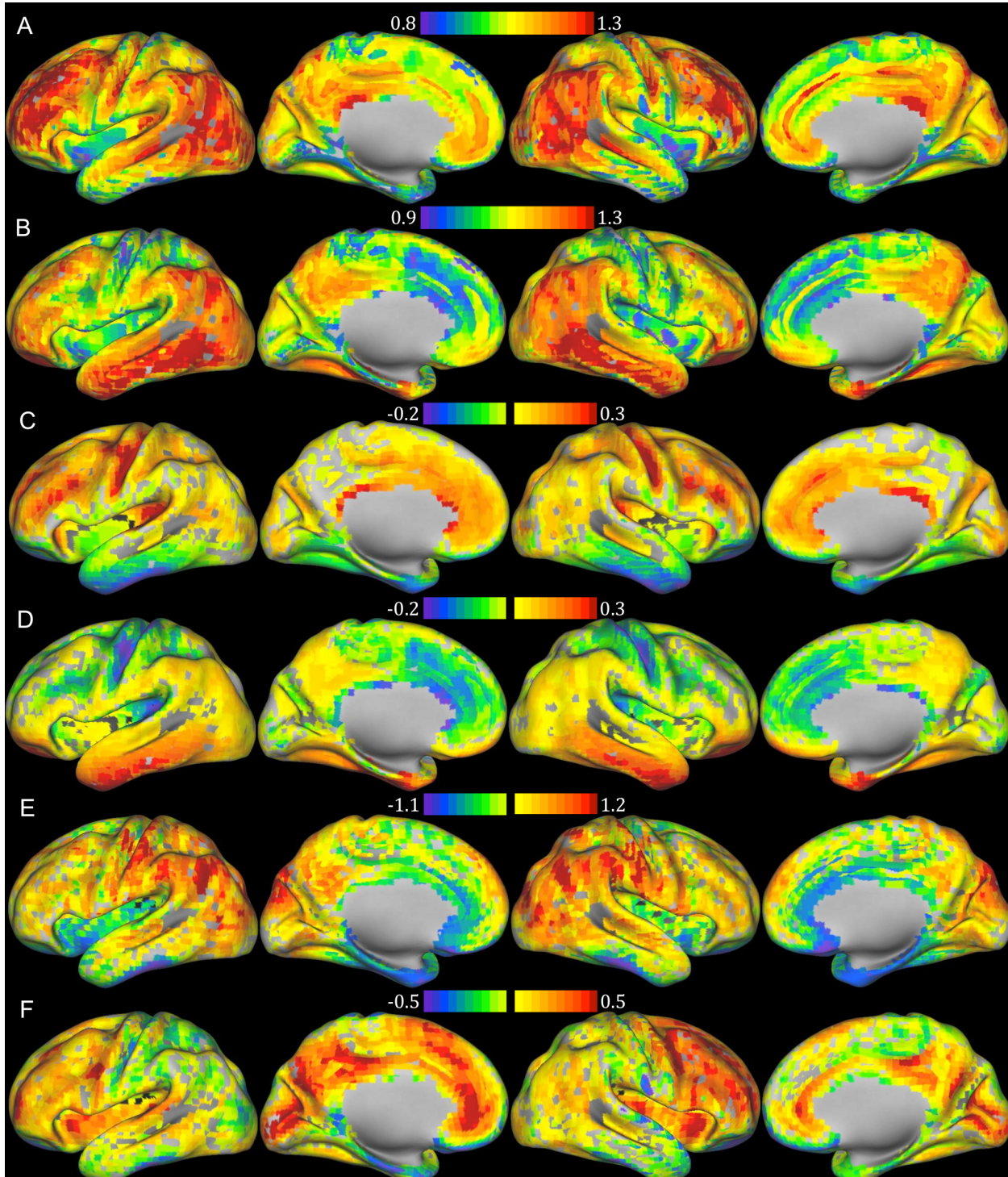


**Fig. 3:** Topologies of AD pathology in healthy aging and early-life predictors of AD pathology. Topologies of the consensus maps from average older adults representing (A) A $\beta$  pathology (PIB DVR), (B) tau pathology (AV1451 SUVR), (C) A $\beta$  pathology decorrelated from tau, and (D) tau pathology decorrelated from A $\beta$ . Topologies of the consensus maps from average young adults representing (E) hubs (z-scored degree centrality) and (F) metabolic inefficiency.

degree centrality with A $\beta$  or tau was driven by the shared variance of A $\beta$  and tau, rather than A $\beta$  or tau itself. We found a strong positive correlation of early-life metabolic inefficiency ( $R=0.493$ ,  $p<<e^{-100}$ ) with late-life A $\beta$  deposition (decorrelated from tau) and a negative correlation of early-life metabolic inefficiency ( $R=-0.18$ ,  $p<e^{-100}$ ) with late-life tau (decorrelated from A $\beta$ ). This suggests that the correlation of tau with metabolic inefficiency was driven by the shared variance of tau with A $\beta$ , rather than tau itself. This is consistent with our qualitative observation that key areas affected by tau – the medial temporal lobe and orbitofrontal cortex – were not metabolically inefficient in early life.

## Discussion

To explore factors that may drive differences across the brain in susceptibility to A $\beta$  and tau pathologies, we examined the overlap of measures of brain function in early-life with AD pathology in late-life. We investigated the extent to which the topology of hubs and a novel metric “metabolic inefficiency” in young adults overlapped with the topology of A $\beta$  and tau in cognitively normal older adults. To examine the earliest stages of AD progression, we focused on A $\beta$  and tau in cognitively normal older adults. To avoid confounding age- and disease-related changes and to gain a lifespan view of brain function, we focused on measures of metabolism and hubs in a separate group of young adults. We found that hubs explained 29% of the variance of metabolism across the brain of the average young adult. However, the topology of “metabolic inefficiency”, or unexplained variance in metabolism indicative of metabolic demand unrelated to brain connectivity, was strongly predictive of the topology of A $\beta$  in late-life. The strong positive relationship of early-life metabolic inefficiency with late-life A $\beta$  stood in contrast to its weaker positive relationship with late-life tau, as well as the weaker negative relationships of early-life hubs with late-life A $\beta$  and tau. Intriguingly, the relationship of metabolic inefficiency with A $\beta$  pathology suggests that, given a particular metabolic rate, more highly connected areas are less – not more – susceptible to A $\beta$  pathology. These findings support a shift away from the focus of the role of hubs in initial vulnerability to AD pathology, and towards a focus instead on the susceptibility of alternate aspects of tissue metabolic characteristics to A $\beta$  pathology.

### The physiological underpinning of vulnerability to A $\beta$ in healthy aging.

We sought to examine the physiological underpinning of AD pathology in healthy aging by examining two prominent aspects of brain physiology – functional connectivity and glucose metabolism. While elevated metabolism (Oh et al., 2016) and hubs (Buckner et al., 2009) have both been linked to A $\beta$  pathology, increased brain connectivity entails higher metabolic demand (Liang et al., 2013, Bullmore and Sporns, 2012, Riedl et al., 2014) and its relationship to A $\beta$  has only been established in patients with AD with pervasive, and presumably longstanding widespread A $\beta$  deposition (Buckner et al., 2009). We aimed to differentiate between contributions of hubs versus glucose metabolism to susceptibility to A $\beta$  across brain tissue in healthy aging, distinguishing metabolic demands related to sustaining brain connectivity from other brain processes that contribute to metabolic demand. We show that the metabolic demands for non-connectivity-related brain processes in early-life, which we call “metabolic inefficiency”, explain the topology of A $\beta$  in late-life.

The brain has differential demands for non-oxidative and oxidative metabolic processes. Brain areas with high levels of aerobic glycolysis exhibit increased genetic expression for synapse formation and growth, whereas areas with high levels of oxidative glucose metabolism exhibit increased expression for metabolic processes (Goyal et al., 2014). Aerobic glycolysis undergoes profound age-related reduction in late-life that may underlie the vulnerability of areas with high aerobic glycolysis to AD pathology (Goyal et al., 2017, Sheline and Raichle, 2013). Glucose metabolism also undergoes age-related changes (Chetelat et al., 2013), although, interestingly, brain areas with age-invariant metabolism and hypermetabolism may be more – not less – vulnerable in AD (Oh et al., 2016). It is possible that the brain processes captured by metabolic inefficiency, like aerobic glycolysis, support neuroprotective mechanisms that are depleted in aging and lead to vulnerability to A $\beta$  pathology through synaptic depression, loss of

dendritic spines, excitotoxicity, and/or oxidative stress (Goyal et al., 2017, Sheline and Raichle, 2013).

Alternately, metabolic inefficiency may reflect and/or overlap with non-metabolic mechanisms that drive vulnerability to AD pathology. Metabolically inefficient brain areas may reflect developmental differences between brain regions in properties like redundancy (e.g. of synapses) or differential pruning during development. The default mode and executive control networks, which are vulnerable to AD pathology and the effects of aging generally (Jagust, 2013), demonstrate persistent plasticity into late childhood and early adulthood (Reisberg et al., 2002). Moreover, these systems also reflect areas of high cortical expansion in humans relative to other primates (Hill et al., 2010, Fjell et al., 2015). Further work is necessary to delineate the source of vulnerability of metabolically inefficient brain areas to A $\beta$  pathology.

#### Hubs don't explain topology of AD pathology in healthy aging.

Theoretical work suggests that hubs may be vulnerable in AD through activity-dependent degeneration (de Haan et al., 2012), which may be a prolonged process that occurs over the lifespan (Jagust, 2013). In mouse models of AD, A $\beta$  has been linked to synaptic activity resulting in the secretion of A $\beta$  and associated with the formation of A $\beta$  plaques (Bero et al., 2011). The functional synchrony that underlies functional connectivity takes the form of high-gamma oscillations, generated through the inhibitory action of GABA-ergic interneurons, and drive resting glucose metabolism (Lord et al., 2013). Previous work has demonstrated that the topology of A $\beta$  in patients with AD was reflected by the topology of hubs (Buckner et al., 2009). In light of these observations, we sought to see if hubs were also associated with vulnerability to A $\beta$  pathology in healthy aging.

When examining the earliest stages of AD pathology, before the widespread and dramatic accumulation associated with AD, we did not find a correspondence between hubs and A $\beta$  deposition. Thus our findings in cognitively normal older adults diverge from a prior study relating hubs to A $\beta$  deposition in patients with AD (Buckner et al., 2009). Besides the different populations used to examine A $\beta$ , these studies differed in that our study excluded subcortical brain areas. However, we confirmed our results – a weak negative correlation of A $\beta$  with hubs – using the consensus hub map used in the study by Buckner and colleagues (2009). Our study indicates that A $\beta$  may not preferentially accumulate in hubs in the earliest stages of AD. Rather, hubs may be vulnerable as the disease progresses, which would be consistent with AD models of cascading network failure (Jones et al., 2016).

#### Metabolic inefficiency explains topology of A $\beta$ , not tau.

We observed substantial overlap of A $\beta$  and tau in cognitively normal older adults, which we posit to have driven the association between metabolic inefficiency and tau. When A $\beta$  was decorrelated with tau, we observed a consistent strong positive relationship of A $\beta$  with metabolic inefficiency. In contrast, when tau was decorrelated with A $\beta$  we instead observed a negative relationship of tau with metabolic inefficiency. Moreover, the preferential overlap of metabolic inefficiency with A $\beta$  – but not tau – became apparent when focusing on the brain areas uniquely susceptible to A $\beta$  or to tau. The medial temporal lobe – which exhibits the earliest susceptibility to tau and typically only accumulates A $\beta$  only with more advanced AD progression – was metabolically efficient in young adults. These discrepancies make it unlikely that early life metabolic inefficiency contributes initially to vulnerability of the brain to tau. Instead, the areas of overlap of metabolic inefficiency, A $\beta$ , and tau are consistent with interdependence of A $\beta$  and

tau pathologies, which has been reported using various manipulations in cell and animal models (Ittner and Gotz, 2011) and observations of widespread local correlations of A $\beta$  and tau from *in-vivo* PET imaging of humans (Sepulcre et al., 2016). Therefore, due to the overlapping distributions of A $\beta$  and tau, we concluded that metabolic inefficiency was associated vulnerability to A $\beta$  (including brain areas with joint A $\beta$  and tau pathology), but not brain areas specifically vulnerable to tau early in AD.

#### Implications for the mechanism of accumulation of AD pathology.

If A $\beta$  and/or tau pathology spread transsynaptically, the focus should be on identifying the earliest-affected area(s) to determine the initial source of introduction of AD pathology. Early A $\beta$  deposition has been reported in the precuneus, medial orbitofrontal, and posterior cingulate cortices (Palmqvist et al., 2017), without consensus on a single initial source. The diffuse pattern of A $\beta$  accumulation even in initial stages of presentation of A $\beta$  pathology (Braak and Braak, 1991) seems to support the shared vulnerability hypothesis. However these regions form core areas of the default mode network (Palmqvist et al., 2017), so it is possible that they reflect trans-synaptic spread through a large and highly connected network. The identification of shared physiological features in early life that mirror the topology of A $\beta$ , including metabolic inefficiency, also support the shared-vulnerability framework of A $\beta$ . In contrast, the lack of a clear physiological explanation for the topology of tau – particularly in transentorhinal cortex, widely considered to be the initial locus of tau (Braak and Braak, 1991) – suggest that the topology of tau may largely reflect trans-synaptic spread (Jacobs et al., 2018). Further work is necessary to understand the etiology of tau pathology and its coevolution with A $\beta$ , which may be linked through neuroplasticity failure (Mesulam, 1999, Styr and Slutsky, 2018) and/or cascading network failure (Jones et al., 2017).

#### Limitations.

There are some notable limitations to this study. We used three separate groups of subjects, which could introduce noise and error into measurements, however this would be expected to attenuate any effects, thus the persistence of our findings increases the likelihood that these results generalize to a larger population. Due to the large number of voxels that went into this comparison, the level of significance of the statistics across voxels is of lesser importance than the effect size (e.g. R and % changes). It would be informative to examine other measures of brain load and neural activity, besides measures of connectivity derived from spontaneous activity during “resting state” and glucose metabolism from FDG-PET. However, it has been suggested that task-related brain activity accounts for a small – though potentially informative – portion of metabolic activity (Liang et al., 2013) and dependencies in spontaneous brain activity predict the majority of task-related activity (Cole et al., 2016). However, brain state even during “resting state” can alter functional connectivity (Patriat et al., 2013, Kawagoe et al., 2018). Moreover, this study does not take into account age-related changes to functional connectivity and metabolism across the lifespan, and it is unclear to what extent these predictions would hold up if we drew upon functional data from older subjects. However, the use of measure of brain function in young adults to predict markers of AD in older adults allows us to examine healthy brain function in a state unperturbed by age- and AD-related changes, avoiding any confounding influence of pathology on brain function.

## Conclusion.

This work refines the narrative surrounding the roles of hubs and metabolism in AD pathology. The explanatory power of metabolic inefficiency in predicting A $\beta$  topology suggests that glucose metabolism – beyond its role in supporting brain connectivity – is associated with A $\beta$ .

Furthermore, hubs do not play a predominant role in early vulnerability to A $\beta$  or tau in healthy older adults. In light of previous work linking hubs to A $\beta$  pathology, this suggests that hubs become vulnerable to A $\beta$  pathology with more advanced progression of AD pathology (e.g. in patients with MCI or AD). We also found a relationship of tau with metabolic inefficiency, however we provide evidence that this relationship was driven by covariance in the topologies of A $\beta$  and tau in the healthy older adults. Further work into the processes underling metabolic demand and alternate features that may be driving vulnerability to A $\beta$  and tau pathology is necessary to fully understand the etiology of AD pathology.

## Chapter 4

### Amyloid- $\beta$ spreads from multiple sources in healthy aging

#### Abstract

The hallmark pathology of Alzheimer's disease, amyloid- $\beta$  plaques (A $\beta$ ), typically exhibits advanced progression throughout cortex by the time cognitive symptoms manifest. Despite a characteristic spatiotemporal progression of A $\beta$  pathology in the pre-symptomatic phase, there is no consensus on the earliest brain areas that accumulate A $\beta$ . We developed a novel cross-sectional approach to examine regional accumulation relative to the total amount of A $\beta$  pathology in the brain within different stages of A $\beta$  progression in healthy aging – PIB-, Early PIB+, and Late PIB+ – by examining PIB-PET from 147 cognitively normal older adults as well as from 16 young adults. We modeled the cross-sectional rates of accumulation to generate directed progression networks, which measure progression from earlier to a later A $\beta$  stages by drawing connections emanating from regions with accelerated accumulation in earlier A $\beta$  stages and emanating to regions with accelerated accumulation in later A $\beta$  stages. We identified potential sources of A $\beta$  pathology in the PIB- stage, relays in the Early PIB+ stage, and targets in the Late PIB+ stage. The sources, relays, and targets of A $\beta$  pathology were distributed across the brain, comprising multiple brain networks. The largest number of sources and relays were in the default mode network, however all regions of the memory network were impacted. Relays, and to a lesser extent sources, additionally impacted the other higher order brain networks whereas the targets of advanced A $\beta$  pathology primarily impacted sensory networks. This framework suggests that distributed brain areas across multiple networks may serve as sources of A $\beta$  even before substantial A $\beta$  pathology is detected in healthy aging. While specific brain networks such as the default mode and memory networks may be particularly impacted, especially as A $\beta$  pathology progresses, accumulation of A $\beta$  pathology is diffuse, multifocal, and does not appear to emanate from any single source or brain network.

## Introduction

Alzheimer's disease (AD) is characterized by a systematic spatiotemporal progression of amyloid- $\beta$  plaques (A $\beta$ ) and neurofibrillary tangles (tau). Central to understanding and treating AD, we must delineate the pathways through which the major pathological hallmarks of AD propagate. Tau progression is fairly well characterized in cross-sectional autopsy studies, occurring in progressive stages that initiate in the transentorhinal cortex, spread to medial and inferior temporal brain areas, and then to association cortex (Braak and Braak, 1995). However, characterizing stages of A $\beta$  progression has been more challenging – in the “initial” stage of AD, A $\beta$  neuropathology is already widely distributed across frontal, parietal, occipital, and temporal neocortex (Thal et al., 2002). However, AD develops over the course of decades with a prolonged preclinical phase (Sperling et al., 2011); to achieve a complete understanding we must explore the temporal progression of AD in the pre-symptomatic phase.

The primary mechanism(s) and pathway(s) through which A $\beta$  typically spreads remain unclear. Numerous mechanisms have been proposed, including spread of A $\beta$  through extracellular-based transmission via diffusion to spatially contiguous neighbors (Knowles et al., 2011), transneuronal-based transmission through neural connections (de Calignon et al., 2012, Eisele et al., 2010, Moreno-Gonzalez and Soto, 2011), and other mechanisms including via the blood stream (Walker et al., 2012). Increasing evidence suggests that A $\beta$  may be multifocal – emanating from multiple sources or “epicenters” (Palmqvist et al., 2017, Cho et al., 2016, Grothe et al., 2017). However, there is no consensus on which brain areas initiate the spread of A $\beta$  throughout the brain and through which pathways, if any, A $\beta$  typically spreads.

Approaches from graph theory, which focus on the interdependencies of structure and function between distributed brain areas, have illuminated many aspects of neurological disease. Patterns of atrophy suggest that large-scale brain networks may shape neurodegeneration in dementia (Seeley et al., 2009). Atrophy patterns have been examined cross-sectionally to construct cortical thickness networks (He et al., 2007) – an approach extended to examine cross-sectional A $\beta$  and tau covariance networks (Sepulcre et al., 2013, Sepulcre et al., 2016). However, amyloid covariance networks reveal widespread elevated correlations of A $\beta$  across the brain – leading to little insight on A $\beta$  propagation besides that when A $\beta$  is elevated in one brain area, A $\beta$  is elevated throughout the brain (Sepulcre et al., 2016, Lockhart et al., 2017). Network structure may be exploited to gain insights into the mechanisms and pathways at play (Zhou et al., 2012, Sepulcre et al., 2013), although few applications directly model the temporal progression of A $\beta$  pathology. Examination of how A $\beta$  pathology spreads in humans is limited, facing the experimental hurdle of measuring the spatiotemporal changes of pathology that slowly progresses over the course of decades, as well as the challenge of modeling and drawing meaningful conclusions about a dynamic process. One promising approach, developed to characterize longitudinal dependencies in atrophy, is directed progression networks (Freidman et al., 2014).

In the present work, we expanded the directed progression network approach, extending it to cross-sectional PIB-PET to explore the progression of A $\beta$  pathology in normal aging across young adults and cognitively normal older adults. We defined a Young stage as well as three stages of A $\beta$  progression in older adults: PIB-, Early PIB+, and Late PIB+. For each brain region, we used cross-sectional data to measure the slope of the relationship across subjects between local A $\beta$  (i.e. regional PIB) and total PIB load – interpreting the slope as the cross-sectional “rate of accumulation”. This approximation of cross-sectional rate of accumulation

differs from traditional measures – which are defined longitudinally within a given subject – using the total PIB load of each scan as a rough approximation of “time” in a theoretically systematic progression of A $\beta$  across subjects. We conceptualized a lower total PIB load as representing an earlier point in the spectrum of A $\beta$  progression in normal aging, with higher total PIB loads indicative of more advanced A $\beta$  progression. We then constructed directed progression networks, comprised of connections that emanated from brain regions with cross-sectional accumulation in an earlier A $\beta$  stage (e.g. Young to PIB-; PIB- to Early PIB+) and went to brain regions with cross-sectional rates of accumulation that accelerated in a later A $\beta$  stage (e.g. PIB- to Early PIB+; Early PIB+ to Late PIB+). By focusing on accelerations in the cross-sectional rates of accumulation, we avoided over-interpreting positive cross-sectional rates of accumulation, which were observed even in young adults presumably free of A $\beta$  pathology. We used directed progression networks to identify potential sources, relays, and targets of A $\beta$  pathology in healthy aging.

## Materials and methods

### Participants.

The study examined 16 young adults and 147 cognitively normal older adults from the Berkeley Aging Cohort Study (BACS). Participants underwent PIB-PET to measure A $\beta$  and structural MRI to aid processing and analysis of the PET data. Participants were recruited from the community via newspaper advertisements and were required to live in the community independently and to be without major medical, neurological, and psychiatric illnesses that could influence cognition. Normal cognition was established by scores on the Mini Mental State Examination  $\geq 26$  and performance on memory tests within 1.5 standard deviations of age-adjusted norms. Genotype (N=15) and education (N=5) information were missing for a small subset of BACS subjects. See Table 1 for participant demographics.

	<b>Young (N=16)</b>	<b>Old PIB- (N=93)</b>	<b>Old Early PIB+ (N=40)</b>	<b>Old Late PIB+ (N=14)</b>
<b>Age</b>	$23.6 \pm 2.5$ (21, 30)	$76.83 \pm 6.01$ (61, 91)	$76.62 \pm 5.77$ (65, 96)	$78.14 \pm 4.91$ (71, 87)
<b>Sex (%F)</b>	50%	54.84%	57.5%	78.57%
<b>Education (years)</b>	$15.4 \pm 1.3$ (12, 18)	$17. \pm 2.07$ (12, 20)	$16.08 \pm 2.06$ (12, 20)	$16.36 \pm 2.35$ (12, 20)
<b>Apoe <math>\epsilon 4</math> Carrier</b>	28.6%	19.05%	37.84%	76.92%
<b>PIB Index</b>	$0.98 \pm 0.03$ (0.92, 1.05)	$0.99 \pm 0.05$ (0.71, 1.06)	$1.18 \pm 0.11$ (1.06, 1.4)	$1.57 \pm 0.11$ (1.42, 1.76)

Table 1: Participant demographics.

### MRI acquisition and processing.

To aid preprocessing and tissue segmentation of the PET data, anatomical MR imaging was performed on a 1.5T Magnetom Avanto (Siemens Medical Systems) scanner using a 12-channel head coil at Lawrence Berkeley National Laboratory. Anatomical MRI scans were acquired axially using a high-resolution T1 MP-RAGE sequence (TR = 2110 ms; TE = 3.58 ms; TI = 1100 ms; flip angle = 15°; voxel dimension = 1.00 mm<sup>3</sup>; slice thickness = 1.00 mm with 50% gap).

Anatomical MRIs were linearly coregistered to a template to straighten or, for non-baseline MRIs, were coregistered to the baseline MRI. Each anatomical MRI underwent tissue segmentation using Freesurfer v5.3 (<http://surfer.nmr.mgh.harvard.edu/>). The segmentation was coregistered to PET using an inverted transformation of the affine mapping between the mean PET image and the skull-stripped brain in Anatomical Normalization Tools (ANTs; <http://picsl.upenn.edu/software/ants/>). The cerebellar grey matter ROI from Freesurfer was used as a reference region for PIB-PET processing.

### PIB-PET acquisition and processing.

PIB-PET imaging was performed on either an ECAT EXACT HR or BIOGRAPH Truepoint 6 scanner in 3D acquisition mode at Lawrence Berkeley National Laboratory. For each PET scan a 10-min transmission scan or an X-ray CT was obtained for attenuation correction. PET data were reconstructed using an ordered subset expectation maximization algorithm with a 4mm Gaussian

smoothing kernel, weighted attenuation correction, and scatter correction. The LBNL Biomedical Isotope Facility synthesized [<sup>11</sup>C]PIB using a previously published protocol (Mathis et al., 2003). PIB-PET scanning began immediately upon injection of approximately 15-mCi of [<sup>11</sup>C]PIB into an antecubital vein, with dynamic acquisition frames obtained over 90-minutes as follows: 4 x 15 s, 8 x 30 s, 9 x 60 s, 2 x 180 s, 10 x 300 s, and 2 x 600 s.

Frames within the first 5 minutes of PIB-PET data were summed, and all frames including the summed image were realigned to the middle frame. The cerebellar grey matter ROI from Freesurfer was used as a reference region for Logan graphical analysis on frames corresponding to 35- to 90-minutes post-injection, which produced PIB distribution volume ratio (DVR) images.

#### PIB index.

The PIB index was computed for each PIB-PET scan as the mean PIB DVR across prefrontal, lateral temporal, parietal, and cingulate cortices (Mormino et al., 2012) to approximate the extent of A<sub>β</sub> pathological burden in the brain of each participant that underwent PIB PET.

#### Definition of A<sub>β</sub> stages.

We used PIB index as the basis to form subgroups of cognitively normal older subjects representative of progressive ‘stages’ of A<sub>β</sub> accumulation in the pre-symptomatic phase of Alzheimer’s disease (Fig. 1). We defined all scans with a PIB index  $\geq 1.06$  as “PIB+” and all scans with a PIB index  $< 1.06$  as “PIB-”. We calculated the range of PIB index values of the PIB+ scans and split the subjects into two groups – representing the “Early PIB+” and “Late PIB+” stages of PIB progression – with similar ranges of PIB indexes. The range of the PIB indexes of the PIB- scans ( $N = 93$ ) was 0.344 (0.71 to 1.06). The range of the PIB indexes of the PIB+ scans ( $N = 54$ ) was 0.701 (1.06 to 1.76). The PIB+ scans were divided into “Early PIB+” and “Late PIB+” stages representing a similar range of PIB indexes, such that the early PIB+ stage ( $N=40$ ) had a range of 0.34 (1.06 to 1.4) and the late PIB+ stage ( $N=14$ ) had a range of 0.345 (1.42 to 1.76). Thus, the PIB-, Early PIB+, and Late PIB+ stages all represent a similar dynamic range in the spectrum of A<sub>β</sub> progression in healthy aging. This approach does not ensure that there is an equal number of subjects in each group, however it does ensure that each stage – PIB-, Early PIB+, and Late PIB+ – represents a similar dynamic range in the spectrum of PIB progression in preclinical AD. Given that this sample reflects healthy aging, we expect the largest number of subjects to be in the PIB- stage and the fewest number of subjects to be in the late PIB+ stage. We also defined the ‘Young’ stage, which we consider the baseline ‘stage’ prior to A<sub>β</sub> accumulation.

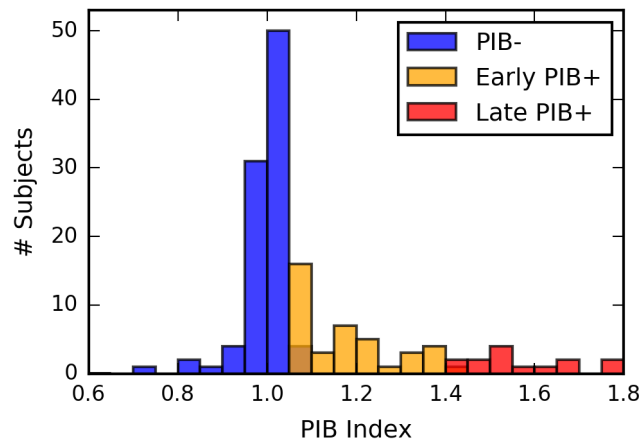


**Fig. 1:** Histogram of PIB indexes for each A<sub>β</sub> stage in healthy aging.

### ROI definition.

After converting the MNI coordinates from the atlas from Power and colleagues (2011) to MNI 152 2mm space, we defined the regions of interest (ROIs) by using fslmaths to delineate 10 mm spheres around each coordinate. This approach produced 264 ROIs across the brain of uniform size in MNI 152 2mm space. We used the assignments of each ROI into a canonical functional brain network defined by Power and colleagues (2011). We excluded subcortical and cerebellar ROIs from the analysis, focusing our analysis on the 246 cortical ROIs.

### Calculation of cross-sectional rates of accumulation.

We computed the cross-sectional “rate of accumulation” ( $r_{v,s}$ ) of PIB for each ROI (v) at each stage (s). The calculation was performed across subjects within a given A $\beta$  stage, using each subject’s total PIB load, calculated as the average DVR across cortical ROIs, as a proxy for the “time” point of A $\beta$  progression. We

conceptualize a lower total PIB load as an earlier point and a higher total PIB load as a later point across the spectrum of A $\beta$  progression in healthy aging. We measure the rate of accumulation for a given ROI by computing the slope using Theil-Sen regression – a form of regression that is robust to outliers – of the ROI’s PIB on total PIB (where each point in the regression is a different subject). This resulted in an estimate of the rate of accumulation for each ROI at each ‘stage’, with a positive slope indicating the PIB DVR in the ROI was higher with increased total PIB load – consistent with cross-sectional “accumulation” of PIB in the ROI that should reflect a temporally driven process. See Fig. 2 for an example.

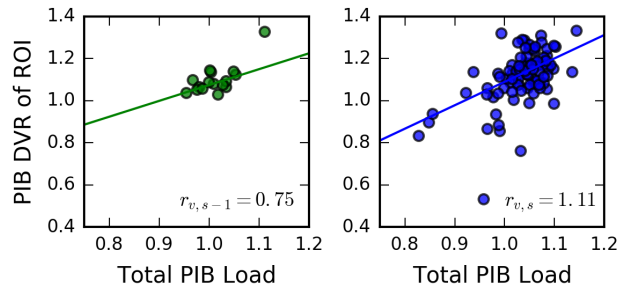


**Fig. 2:** Cross-sectional rates of accumulation for an example node from the memory network. Scatter shows total PIB load by the ROI’s PIB DVR, where each point is a different subject. This node (v) is a source, possessing cross-sectional rates of accumulation that accelerate from the Young stage ( $r_{v,s-1}$ ) to the PIB+ stage ( $r_{v,s}$ ). Green = Young, Blue = PIB+.

### Bootstrap procedure for cross-sectional rates of accumulation.

To restrict analysis to only those rates of accumulation that are positive, we used a bootstrap procedure to estimate the 95% confidence interval of each rate of accumulation estimate. We completed the bootstrap procedure for each ROI at each A $\beta$  stage by randomly selecting N subjects from the A $\beta$  stage with replacement, where N is the number of subjects in the A $\beta$  stage, and calculating the cross-sectional rate of accumulation. This procedure was repeated 200 times. We defined the lower bound of the 95% confidence interval as the value for which 95% (N=190) of the bootstrapped rate of accumulation estimates were greater than the value. The rate of accumulation of the ROI was set to 0 if the lower bound of the 95% confidence interval was  $\leq 0$ .

### Directed progression graph of PIB.

We extended the directed progression graph approach (Friedman et al., 2014) to estimate progression of A $\beta$  in healthy aging. We examined two stages of progression: from the PIB- to the Early PIB+ stage as well as from the Early PIB+ to the Late PIB+ stage. Using the cross-

sectional rates of accumulation ( $r_{v,s}$ , described above), we computed the directed similarity between each pair of ROIs ( $v, w$ ):

$$\begin{array}{ll}
 \text{if } r_{v,s} \leq r_{v,s-1} & \rightarrow 0 \\
 \text{elif } r_{w,s+1} \leq r_{w,s} & \rightarrow 0 \\
 \text{elif } r_{v,s} < r_{w,s} & \rightarrow 0 \\
 \text{elif } r_{w,s-1} \leq r_{w,s} & \rightarrow 0 \\
 \text{else} & \rightarrow 1
 \end{array}$$

Where  $r$  is the cross-sectional rate of accumulation,  $v$  is a potential source,  $w$  is a potential target, and  $s$  is the A $\beta$  stage. For the directed progression network from PIB- to Early PIB+, the A $\beta$  stages for **s-1**, **s**, and **s+1** were respectively the Young, PIB-, and Early PIB+ stages. For the directed progression network from Early PIB+ to Late PIB+, the A $\beta$  stages for **s-1**, **s**, and **s+1** were respectively PIB-, Early PIB+, and Late PIB+. The algorithm enforced that (1) sources had an accelerated rate of accumulation at stage  $s$  relative to the prior A $\beta$  stage (i.e. **s-1**), (2) targets had an accelerated rate of accumulation at stage **s+1** relative to the prior A $\beta$  stage (i.e. **s**), (3) sources had a faster rate of accumulation than targets at stage  $s$ , (4) targets did not have an accelerated rate of accumulation at stage  $s$  relative to the prior A $\beta$  stage (i.e. **s-1**). Rule (4) ensured that targets were not also sources within the same graph. This produced a directed progression graph where directed edges emanated from sources with accumulation that accelerated from the baseline (i.e. **s-1**) to earlier stage (i.e. **s**) and went to targets with accumulation that began to accelerate from the earlier (i.e. **s**) to later stage (i.e. **s+1**) (see Table 1).

	Cross-sectional rates of accumulation ( $r_{v,s}$ )		
A $\beta$ Stage ( $s$ )	<b>s-1</b>	<b>s</b>	<b>s+1</b>
Source ( $v$ )	- or +	++	- or = or ++
Target ( $w$ )	- or +	- or =	++

$$- : r_{v,s} \leq 0 \quad + : r_{v,s} > 0 \quad = : r_{v,s} = r_{s-1} \quad ++ : r_{v,s} > r_{v,s-1}$$

**Table 1:** Pattern of cross-sectional rates of accumulation across A $\beta$  stages for sources ( $v$ ) and targets ( $w$ ) in directed progression networks. For the PIB- to Early PIB+ directed progression network,  $s-1$  = Young,  $s$  = PIB-,  $s+1$  = Early PIB+. For the Early PIB+ to Late PIB+ directed progression network,  $s-1$  = PIB-,  $s$  = Early PIB+, and  $s+1$  = Late PIB+.

### Node classification.

For each node of a directed progression graph, we computed the out-degree, the number of directed edges emanating from the given node to all other nodes, and the in-degree, the number of directed edges emanating to the given node from all other nodes. We designated as “sources” all nodes with 1 or more outputs (i.e. out-degree  $> 0$ ) in the PIB- to Early PIB+ directed progression graph, since these nodes are the initial loci of PIB pathology. We designated as “relays” all sources in the Early PIB+ to Late PIB+ directed progression graph, since these regions aren’t necessarily the initial loci of PIB pathology, but still “relay” PIB pathology to a more advanced stage of PIB progression. We designated as “targets” all nodes with 1 or more inputs (i.e. in-degree  $> 0$ ) in the Early PIB+ to Late PIB+ directed progression graph, since these nodes receive input in the most advanced stage of A $\beta$  progression in healthy aging.

## Results

### Cross-sectional rates of accumulation of PIB.

For each ROI, we modeled the rates of accumulation of A $\beta$  pathology using cross-sectional data within each A $\beta$  stage. The rates of accumulation with each stage were centered around 1, with the PIB- stage possessing the most narrow range of values and the Young and Early PIB+ stages possessing the widest range of values, including the largest number of ROIs that were not accumulating (Fig. 3 A). Although young subjects show many ROIs exhibiting “accumulation”, the narrow range of PIB DVRs across regions, along with the assumption that true A $\beta$  accumulation in people of this age group is unlikely, suggests that within the young subjects these associations could reflect noise. Noise seems a less likely explanation for associations in other groups because the DVRs are generally much higher than one would expect to occur randomly.

Across ROIs within each A $\beta$  stage, we found that regional rate of accumulation correlated with mean regional PIB DVR (Fig. 3 B). This indicates that ROIs with a higher mean PIB DVR within each stage had an elevated rate of accumulation compared to ROIs with a lower mean PIB DVR. The maintenance of this relationship through the Late PIB+ suggests that PIB may continue to accumulate in ROIs with relatively high PIB DVR.

We also compared the rates of accumulation of different canonical brain networks for each stage of A $\beta$  progression. We examined the total rate of accumulation within each canonical brain network as well as the mean rate of accumulation to account for disparities in network size – the largest network, the DMN, had 58 ROIs (23.48% of total cortical ROIs) and the smallest network, the “memory/retrieval network” had 5 ROIs (2.02% of total cortical ROIs). The DMN had the highest total rate of accumulation across A $\beta$  stages, however the networks with the highest mean rate of accumulation across ROIs varied by A $\beta$  stage (Fig. 4).

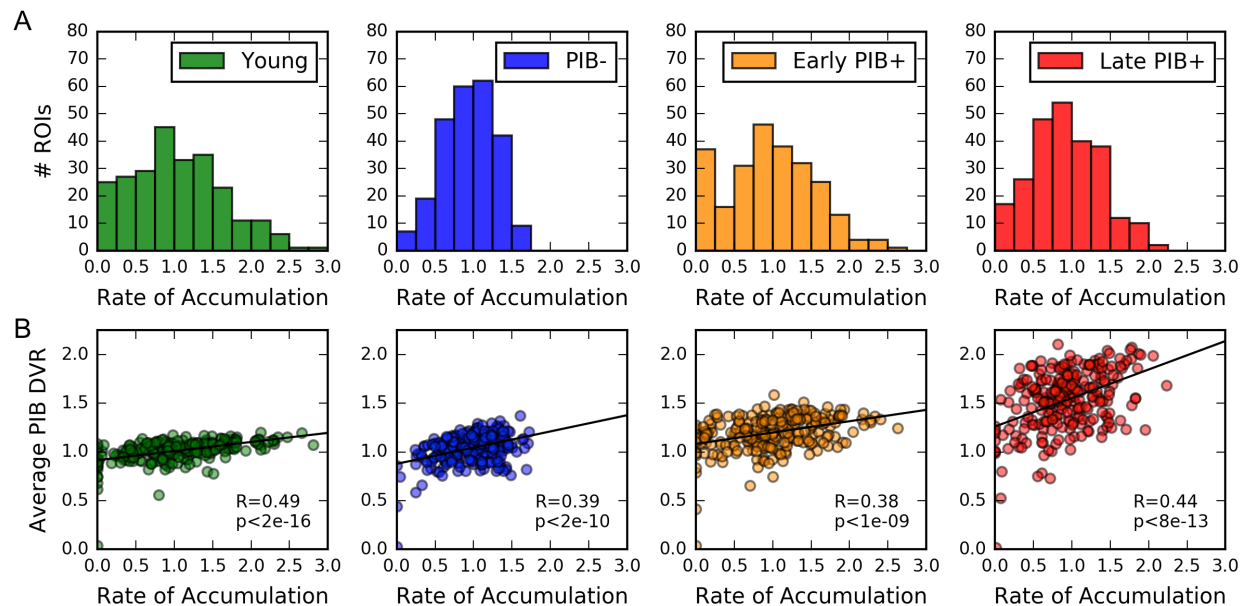


**Fig. 3:** Summary of rates of accumulation for each A $\beta$  stage. **A.** Histograms of distribution of rates of accumulation across ROIs for each A $\beta$  stage. **B.** Scatter plots showing relationship across ROIs between regional rate of accumulation and mean regional PIB DVR (average across subjects) for each A $\beta$  stage. Each point is a different ROI. Green = Young, Blue = PIB- stage, Orange = Early PIB+ stage, Red = Late PIB+ stage

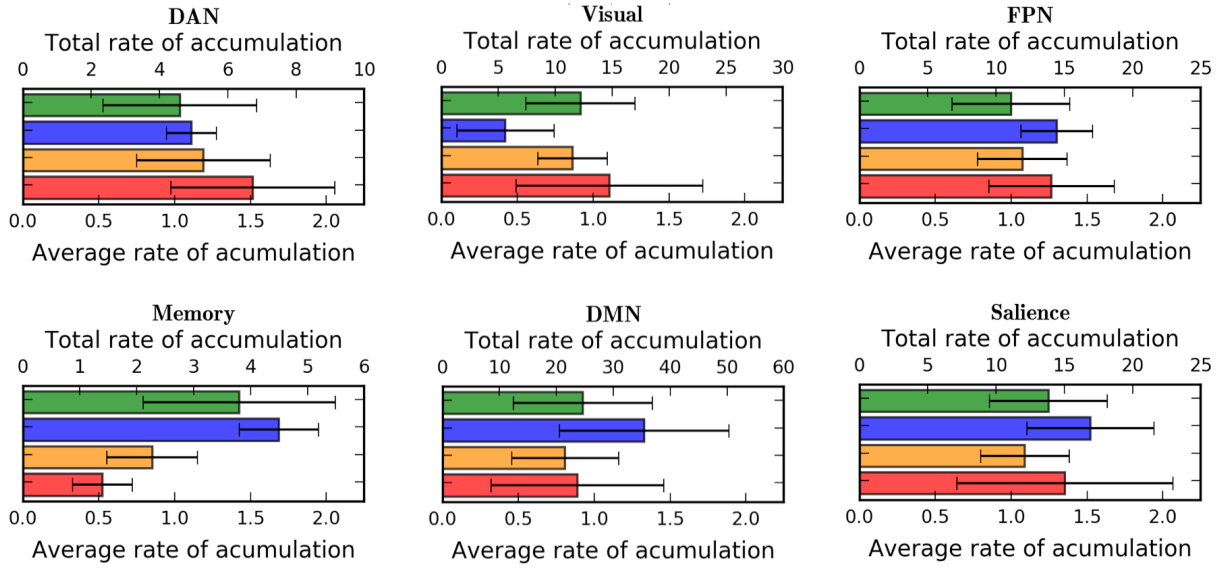


**Fig. 4:** Cross-sectional rates of accumulation of major canonical brain network. Green = Young, Blue = PIB-, Orange = Early PIB+, Red = Late PIB+, DAN = Dorsal Attention Network, FPN = Fronto-Parietal Network, DMN = Default Mode Network

#### Directed progression graph of A $\beta$ .

We generated directed progression graphs of A $\beta$  to represent transitions from earlier to later A $\beta$  stages: from PIB- to Early PIB+ as well as from Early PIB+ to Late PIB+. Each directed edge indicated that accelerated rate of accumulation of A $\beta$  in the earlier stage in one node was associated with accelerated rate of accumulation of A $\beta$  in the later stage in the other node. The total number of edges in the PIB- to Early PIB+ directed progression network comprised 10.96% of the total possible number of edges. This increased to 14.55% of edges in the Early PIB+ to Late PIB+ directed progression network. This is consistent with more diffuse spread of A $\beta$  pathology in more advanced stages of A $\beta$  progression.

#### Sources of directed progression in the PIB-stage.

ROIs with a positive out-degree in the PIB- to Early PIB+ directed progression network were sources of A $\beta$  pathology (see Fig. 5 and Fig. 6). Sources encompassed 46.56% of the nodes. The largest number of sources was in the DMN, with 48.28% of the DMN serving

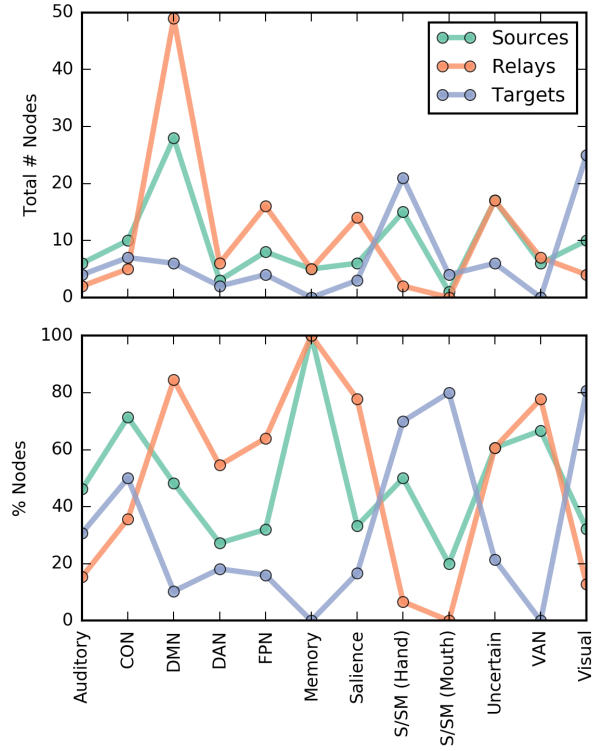


**Fig. 5:** Sources, relays and targets across canonical brain networks. Sources of A $\beta$  progression in the PIB- stage, relays of A $\beta$  progression in the Early PIB+ stage, and targets of A $\beta$  progression in the Late PIB+ stage. (**Top**) The number of ROIs with each node role in each canonical brain networks. (**Bottom**) The percent of the canonical brain network comprised of each node role. CON = Cingulo-Opercular Network, DMN = Default Mode Network, DAN = Dorsal Attention Network, FPN = Fronto-Parietal Network, S/SIM = Sensory/Sensorimotor, VAN = Ventral Attention Network

as sources for the transition from the PIB- to Early PIB+ A $\beta$  stage. Additionally, all of the nodes in the memory network served as sources. Beyond the DMN and memory network, more than half of the nodes in the cingulo-opercular and the ventral attention networks were implicated as sources. The sources included brain regions broadly distributed across temporal, inferior and superior frontal, lateral and medial orbitofrontal, superior parietal, precentral, lateral occipital, lingual, insular, precuneus, and cingulate cortex.

#### Relays of directed progression in the Early PIB+ stage.

ROIs with a positive out-degree in the Early PIB+ to Late PIB+ directed progression network were relays of A $\beta$  pathology (see Fig. 5 and Fig. 6). Relays encompassed 51.42% of the nodes. ROIs with an in-degree in the PIB- to Early PIB+ directed progression network comprised a subset of the relays (52.76% of relays). The rest of the relays were sources in the PIB- to Early PIB+ directed progression network, possessing rates of accumulation that accelerated in both the PIB- and Early PIB+ stages of A $\beta$  pathology. The largest number of relays was in the DMN, with 84.48% of the DMN serving as relays. Additionally, all nodes in the memory network were relays. Beyond the DMN and memory network, relays were broadly distributed across the salience, dorsal attention, ventral attention, and frontoparietal networks. The relays primarily included brain regions in cingulate, temporal, frontal, insular, and parietal cortices.

#### Targets of directed progression in the Late PIB+ stage.

ROIs with a positive in-degree in the Early PIB+ to Late PIB+ directed progression network were considered targets of A $\beta$  pathology (see Fig. 5 and Fig. 6). Targets of A $\beta$  pathology in the Late PIB+ stage encompassed 33.2% of nodes and were primarily in the sensory and the cingulo-opercular networks. Targets in the late stages of A $\beta$  progression in healthy aging predominantly implicated primary sensory cortices.

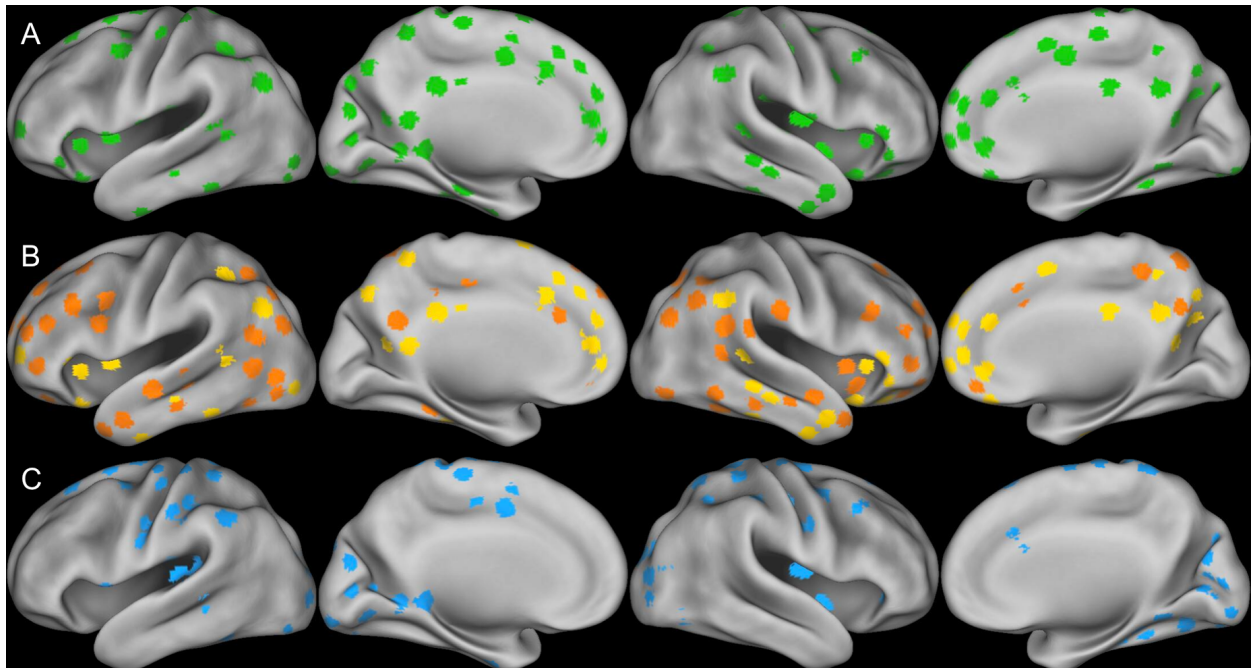


**Fig. 6:** Sources, relays and targets of A $\beta$  pathology. **(A)** Sources of A $\beta$  pathology in the PIB- stage (green). **(B)** Relays of A $\beta$  pathology in the Early PIB+ stage, colored based on relays that overlap with sources (light-orange) and unique relays (dark-orange). **(C)** Targets of A $\beta$  pathology in the Late PIB+ stage (blue).

## Discussion

We developed a novel method to examine the spread of A $\beta$  pathology across the spectrum of healthy aging. We modeled the rate of accumulation of A $\beta$  pathology using cross-sectional data in Young, PIB-, Early PIB+, and Late PIB+ stages of A $\beta$  pathology, with the total PIB load in each subject serving as a proxy for the relative extent of A $\beta$  progression. Utilizing data across subjects to model the rates of accumulation from each A $\beta$  stage, we created directed progression networks that characterized when the cross-sectional rates of accumulation accelerated relative to the antecedent A $\beta$  stage. We characterized the progression of A $\beta$  pathology from sources to relays and finally to targets of A $\beta$  pathology. We show that we can detect sources, the earliest brain areas impacted by A $\beta$  pathology, prior to the deposition of substantial amounts of A $\beta$  by detecting accelerated accumulation in PIB- older adults relative to the young adults. The largest number of sources and relays were in the default mode network, however all regions of the memory network were implicated. Relays, and to a lesser extent sources, additionally impacted the other higher order brain networks, leaving sensory networks for the final targets of A $\beta$  progression in healthy aging. Our results suggest that accumulation of A $\beta$  pathology is diffuse and multifocal in the earliest stages of A $\beta$  pathology in healthy aging.

Studies that focus on identifying the earliest location(s) of A $\beta$  have divergent results. Longitudinal A $\beta$  PET scans implicated precuneus, orbitofrontal, and posterior cingulate cortices in non-demented older adults in the initial phase of A $\beta$  accumulation (Palmqvist et al., 2017) – mirroring results from a cross-sectional study of early A $\beta$  in cognitively normal older adults (Villeneuve et al., 2015). A different longitudinal A $\beta$  PET study identified the precuneus as the origin of A $\beta$  in autosomal dominant AD (Gordon et al., 2018). Exactly which brain areas most frequently harbor substantial A $\beta$  varies by study – one study implicated frontotemporal association cortex (Cho et al., 2016) and another inferior temporal, fusiform, anterior cingulate, and parietal operculum (Grothe et al., 2017). Moreover, age-related increases of A $\beta$  in non-elderly adults implicated middle temporal neocortex and angular gyrus, which exhibited steeper and earlier increase compared to neocortical A $\beta$  (Gonneaud et al., 2017). By examining patterns of accumulation of A $\beta$  pathology across the full spectrum of healthy aging, our study adds to this literature by detecting diffuse and multifocal early sources of A $\beta$  pathology in PIB- older adults without substantial A $\beta$  deposition.

It is unclear whether the lack of consensus on initial sources of A $\beta$  is driven by methodological differences and challenges or if it indicates that the progressive accumulation of A $\beta$  is a heterogeneous and/or diffuse process. Widespread association between local A $\beta$  and distributed A $\beta$  throughout the brain (Sepulcre et al., 2016) may be indicative of a diffuse process (Mezias and Raj, 2017). In AD, the topology of A $\beta$  is typically characterized as following the default mode network, however, even in its earliest stages, our study and others find that A $\beta$  accumulates – albeit to a much lesser extent – in other canonical brain networks as well as the DMN (Palmqvist et al., 2017). Importantly, A $\beta$  topology can also be explained by vulnerability of hubs (Buckner et al., 2009) and brain areas with high metabolic load (Vlassenko et al., 2010, Oh et al., 2016). Thus, while our results implicate the default mode and memory networks, the acceleration of A $\beta$  pathology is not unique to these networks and may not be best explained in the framework of canonical brain networks and connectivity-based spread. Our results demonstrating numerous sources of A $\beta$  that are broadly distributed across brain networks, alongside multiple studies demonstrating different “first” regions affected, point strongly away from connectivity-based spread driving distributed A $\beta$ . A multifocal origin, or multiple

“epicenters”, is more consistent with a metabolic tissue characteristic driving A $\beta$  accumulation concurrently across distributed brain areas.

By focusing on cross-sectional rates of accumulation that accelerate with advancing A $\beta$  pathology, we were able to detect progression of A $\beta$  pathology unique to each stage of A $\beta$  progression in normal aging. We detected “accumulation” of PIB even in the Young stage, when there is unlikely to be meaningful A $\beta$  pathology. Autopsy studies indicate that A $\beta$  pathology is rare in young adults less than 40 years old (Braak and Braak, 1997), although accumulation may begin in middle-aged adults (Gonneaud et al., 2017, Farrell et al., 2017). We suspect that the measured accumulation predominantly reflects noise as well as systematic patterns in where the PIB tracer binds in the absence of A $\beta$  pathology. To account for this, and to prevent over-interpretation of “positive” rates of accumulation, we focus on accelerations in the cross-sectional rates of accumulation relative to the antecedent A $\beta$  stage. Thus, we restricted sources to be those brain regions with accelerated cross-sectional rates of accumulation in the PIB- stage relative to the Young stage, and so on for advancing stages of A $\beta$  pathology. This not only yielded sources of A $\beta$  pathology in the PIB- stage, but allowed us to identify changes specific to the most advanced stages of A $\beta$  progression in healthy aging, which were targets of A $\beta$  pathology in the Late PIB+ stage. Typical approaches examining advanced stages of A $\beta$  progression would implicate most of the brain in late-stage A $\beta$  pathology. However, our method clearly highlights the relative sparing of involvement of the sensorimotor and visual cortex until the most advanced stages of A $\beta$  progression, demonstrating the ability of our method to highlight jumps in A $\beta$  vulnerability in each progressive stage of A $\beta$  pathology rather than linear continuation of the same progressive process.

Any examination of how and if A $\beta$  pathology “spreads” in humans is limited, facing a plethora of methodological limitations. The greatest hurdle is the protracted period over which A $\beta$  accumulates – measurement of the full course of progression within an individual would require longitudinal PET imaging over the course of decades, facing uncertainty as to when and if any given individual will begin to develop A $\beta$  pathology. Beyond experimental limitations, the statistical tools to model these processes are not fully developed, typically relying on implementation of arbitrary thresholds to form consensus maps based on group information (Cho et al., 2016, Grothe et al., 2017) and resulting in a considerable loss of information. Our current method explores how A $\beta$  pathology accumulates across the spectrum of healthy aging, looking for accelerated accumulation relative to earlier stages of A $\beta$  progression and therefore bypassing the need for thresholds.

The use of cross-sectional data constitutes a significant limitation due to variability of brain structure and tracer uptake across individuals, as well as the difficulty of approximating temporal progression. Ideally, the study would incorporate repeated longitudinal data across decades to measure rate of accumulation within individuals. An additional caveat of the study is that different numbers of subjects were assigned to each stage of A $\beta$  progression, with a relatively small number in the “Young” (N=16) and “Late PIB+” (N=14) stages. While the use of cross-sectional data is not ideal, it allows examination of the full spectrum of A $\beta$  progression in healthy aging. Most longitudinal PET studies consist of a single repeat scan 1 to 3 years after baseline (e.g. Palmqvist et al., 2017, Jack et al., 2018b) – a timeframe that is unlikely to exhibit substantial change in A $\beta$  due to its slow progression. It remains unclear how, given the relatively small anticipated accumulation of A $\beta$  in such a timeframe, the noise of such longitudinal PET studies would compare to the present approach that leverages a wide range of PIB progression

within each A $\beta$  stage. Future studies incorporating longitudinal measures of A $\beta$  accumulation would complement and validate the present framework.

Delineating the earliest epicenter(s) of A $\beta$  pathology and the pathway(s) through which A $\beta$  progresses is central to illuminating the etiology of AD. By extending directed progression networks to cross-sectional A $\beta$  PET, we demonstrate that we can use the wide spectrum of A $\beta$  pathology observed in healthy aging to illuminate how A $\beta$  pathology progresses throughout the brain. We identified multiple sources of A $\beta$  pathology, broadly distributed across the brain, indicating that A $\beta$  pathology is already diffuse and multifocal before substantial A $\beta$  deposition can be detected (i.e. prior to “positive” A $\beta$  PET scans). We identified the targets of A $\beta$  pathology in advanced stages of A $\beta$  progression in healthy aging, demonstrating the ability of our method to highlight the late-stage of involvement of sensorimotor and visual brain areas relative to the rest of the brain. Our approach demonstrates the need to circumvent the use of arbitrary thresholds when detecting the earliest stages of A $\beta$  pathology, providing an alternative based on the rates of accumulation of A $\beta$  pathology (in our case defined using cross-sectional data) that improves sensitivity to early changes in A $\beta$  pathology. However, it appears to be necessary to focus on accelerations in the rate of accumulation for cross-sectional data, but also possibly for longitudinal data. To further advance understanding of the etiology of AD, future studies must delve deeper into the progression of A $\beta$  pathology in individuals typically considered to have negative A $\beta$  PET scans.

## Chapter 5

### Discussion

This dissertation utilizes information from multiple neuroimaging modalities to explore fundamental questions about the etiology of Alzheimer's disease (AD) in its presymptomatic phase. PIB-PET, AV1451-PET, FDG-PET, and resting-state fMRI – respectively measuring A $\beta$ , tau, glucose metabolism, and functional activity in the brain – are examined in cognitively normal young and older adults. The approaches applied throughout are cast in a network framework, based on the viewpoint that AD reflects widespread, systemic failure of association cortex. There is a particular emphasis on the potential role of metabolic processes in the etiology of amyloid- $\beta$  (A $\beta$ ) pathology. **Chapter 2** examines metabolic brain networks in normal aging, characterizing distinct, widespread changes in the dependencies in glucose metabolism with old age that differ from those at high risk for progressing to Alzheimer's disease. **Chapter 3** defines a novel marker "metabolic inefficiency," demonstrating a strong association of metabolic inefficiency – but not highly connected brain areas called "hubs" – with the topology of A $\beta$  pathology in normal aging. **Chapter 4** models the progressive accumulation of A $\beta$  pathology across the brain, demonstrating that A $\beta$  is multifocal and widespread even in the earliest stages of A $\beta$  accumulation in normal aging. While a network-based framework is applied throughout, the results across approaches converge to suggest that early A $\beta$  accumulation is a widespread, multifocal process driven by tissue vulnerability to metabolic factors.

#### Early A $\beta$ pathology is diffuse and multifocal.

The factors that drive accumulation of A $\beta$  remain unclear, however there is a systematic spatiotemporal course of progression of A $\beta$  pathology. It is well established that the widespread, distributed topology of A $\beta$  pathology that characterizes AD is similar in cognitively normal older adults with substantial A $\beta$  deposition (Jansen et al., 2015). **Chapter 4** demonstrates that accumulation of A $\beta$  pathology is multifocal and broadly distributed, even in older adults with low levels of A $\beta$  deposition. Our observation of diffuse, multifocal early A $\beta$  deposition is consistent with the lack of consensus on the 'earliest' area(s) of A $\beta$  deposition across neuroimaging studies (Palmqvist et al., Villeneuve et al., 2015, Cho et al., 2016, Grothe et al., 2017, Gordon et al., 2018, Gonneaud et al., 2017) and histological examination of postmortem brain tissue (Braak and Braak, 1991). Whether or not A $\beta$  demonstrates prion-like qualities (Frost and Diamond, 2010), it is unlikely that trans-synaptic spread explains the pattern of accumulation of A $\beta$  across distributed brain areas.

#### Metabolic tissue vulnerability explains A $\beta$ pathology.

Although there is evidence that A $\beta$  is released as a byproduct of synaptic activity (Cirrito et al., 2005, Bero et al., 2011) – it is unclear whether or not this could explain the systematic pattern of accumulation of A $\beta$  across the brain. However, the spatial topology of A $\beta$  pathology in patients with AD is similar to the topologies of aerobic glycolysis (Vlassenko et al., 2010) and cerebral glucose metabolism (Oh et al., 2016), suggesting that systematic differences in metabolism across the brain may explain differences in vulnerability to A $\beta$  pathology. However, the topology of A $\beta$  pathology in patients with AD is also similar to the topology of hubs (Buckner et al., 2009). This raises the possibility that susceptibility of highly metabolic brain areas could reflect

the process of activity-dependent degeneration – which exerts particularly damaging effects on hubs – rather than metabolic tissue vulnerability (de Haan et al., 2012)

Based on observations that hubs typically have higher metabolic demands (Bullmore and Sporns, 2012), **Chapter 3** characterizes the topology of metabolic inefficiency – glucose metabolism that exceeds metabolic demand predicted by hubs. **Chapter 3** demonstrates that metabolic inefficiency in early life explains the topology of A $\beta$  in normal aging, whereas hubs do not explain the topology of A $\beta$ . Our findings suggest that hubs may be more vulnerable as AD pathology progresses, and may be relatively spared in healthy aging compared to patients with AD. The similarity of the topologies of A $\beta$  and metabolic inefficiency indicates that metabolic tissue vulnerability explains the pattern of accumulation of A $\beta$  across the brain in healthy aging. This finding is also consistent with the multifocal nature of A $\beta$  deposition revealed in Chapter 4.

#### Age and AD-related reorganization of metabolic processes in healthy aging.

The potential link between metabolic tissue vulnerability and A $\beta$  pathology motivates further work that can reveal the factors that contribute to cerebral glucose metabolism, explain what leads to differential metabolic demands across the brain, and identify age- and pathology-related changes in metabolic processes across the brain.

While selective age-related changes in metabolism have been characterized, it remains unclear how and if A $\beta$  pathology relates to reorganization of metabolism in healthy aging. There are contradictory findings as to whether or not glucose metabolism systematically changes in cognitively normal older adults with A $\beta$  pathology (Drzezga et al., 2011, Lowe et al., 2014, Cohen et al., 2009, Oh et al., 2014, Altmann et al., 2015). However, cerebral glucose metabolism declines with age in prefrontal, precentral, perisylvian, and anterior cingulate cortices (Chetelat et al., 2013) – which may reflect age-related loss of aerobic glycolysis (Goyal et al., 2017). Our findings in **Chapter 3** raise the intriguing possibility that our metric of metabolic inefficiency captures brain areas exhibiting aerobic glycolysis. Work on the genetics underlying aerobic glycolysis versus oxidative glucose metabolism (Goyal et al., 2014) – respectively linked to synaptic growth/remodeling and to mitochondrial/synaptic transmission – constitutes an important starting point for understanding the differential processes that contribute to metabolic demand across the brain. These observations raise the intriguing possibility that brain areas undergoing high levels of synaptic plasticity are metabolically inefficient, which may confer vulnerability to A $\beta$  pathology in old age (Mesulam, 1999)

By examining metabolic brain networks, **Chapter 2** provides evidence of systematic changes in the dependencies of metabolism across the brain in old age. The old-age-related pattern differed in those with both substantial A $\beta$  pathology and genetic risk for AD, but not in those with only A $\beta$  pathology or only genetic risk. This suggests that there is a highly systematic profile of relative glucose metabolism in old age, from which only those at the highest risk for progression to AD depart. Further work is necessary to determine whether this highly vulnerable group departed from the profile typical of old age or if they are exhibiting maintenance of youth-like metabolic function. Brain areas that maintain more youth-like metabolic function may be more vulnerable to A $\beta$  pathology (Oh et al., 2016), suggesting that age-related metabolic reorganization may play a role in protecting the brain from AD pathology. Our observation of widespread elevated metabolic correlations across the brain in old age indicates that desegregation of metabolic processes is a pervasive feature of the aging brain – a metabolic form of the age-related phenomenon of “dedifferentiation” (Dolcos et al., 2002, Park et al., 2004, Prakash et al., 2012). Metabolic dedifferentiation could reflect loss of aerobic glycolysis (Goyal

et al., 2017) in old age. Understanding the factors that drive reorganization of metabolism may advance insight into why the aging brain – especially highly metabolic brain tissue – is more vulnerable to A $\beta$  pathology.

### Conclusion.

This dissertation explores how AD pathology begins and progresses in its presymptomatic phase, revealing that – even in the earliest stages of accumulation – A $\beta$  pathology is widespread and multifocal. The various approaches provide converging evidence that metabolic tissue vulnerability may underlie A $\beta$  pathology in healthy aging. Understanding how and why glucose metabolism is systematically reorganized in old age may help reveal why the aging brain becomes susceptible to A $\beta$  pathology. Further work is necessary to understand the earliest stages of AD; these studies will require long-term longitudinal observations to understand the evolution of the changes leading to A $\beta$  deposition and AD.

## References

- Adams, J. N., Lockhart, S. N., Li, L., & Jagust, W. J. (2018). Relationships between tau and glucose metabolism reflect Alzheimer's disease pathology in cognitively normal older adults. *Cereb Cortex In Press*.
- Agosta, F., Vossel, K. A., Miller, B. L., Migliaccio, R., Bonasera, S. J., Filippi, M., . . . Gorno-Tempini, M. L. (2009). Apolipoprotein E epsilon4 is associated with disease-specific effects on brain atrophy in Alzheimer's disease and frontotemporal dementia. *Proc Natl Acad Sci U S A, 106*(6), 2018-2022. doi:10.1073/pnas.0812697106
- Alexander-Bloch, A., Giedd, J. N., & Bullmore, E. (2013). Imaging structural co-variance between human brain regions. *Nat Rev Neurosci, 14*, 322-336. doi:10.1038/nrn3465
- Altmann, A., Ng, B., Landau, S. M., Jagust, W. J., Greicius, M. D., & Alzheimer's Disease Neuroimaging, I. (2015). Regional brain hypometabolism is unrelated to regional amyloid plaque burden. *Brain, 138*(Pt 12), 3734-3746. doi:10.1093/brain/awv278
- Andrews-Hanna, J. R., Snyder, A. Z., Vincent, J. L., Lustig, C., Head, D., Raichle, M. E., & Buckner, R. L. (2007). Disruption of large-scale brain systems in advanced aging. *Neuron, 56*(5), 924-935. doi:10.1016/j.neuron.2007.10.038
- Azari, N. P., Rapoport, S. I., Salerno, J. A., Grady, C. L., Gonzalez-Aviles, A., Schapiro, M. B., & Horwitz, B. (1992). Interregional correlations of resting cerebral glucose metabolism in old and young women. *Brain Res, 589*(2), 279-290.
- Baker, S. L., Maass, A., & Jagust, W. J. (2017). Considerations and code for partial volume correcting [(18)F]-AV-1451 tau PET data. *Data Brief, 15*, 648-657. doi:10.1016/j.dib.2017.10.024
- Ballatore, C., Lee, V. M., & Trojanowski, J. Q. (2007). Tau-mediated neurodegeneration in Alzheimer's disease and related disorders. *Nat Rev Neurosci, 8*(9), 663-672. doi:10.1038/nrn2194
- Barch, D. M., Burgess, G. C., Harms, M. P., Petersen, S. E., Schlaggar, B. L., Corbetta, M., . . . Consortium, W.-M. H. (2013). Function in the human connectome: Task-fMRI and individual differences in behavior. *Neuroimage, 80*, 169-189. doi:10.1016/j.neuroimage.2013.05.033
- Bassett, D. S., Meyer-Lindenberg, A., Achard, S., Duke, T., & Bullmore, E. (2006). Adaptive reconfiguration of fractal small-world human brain functional networks. *Proc Natl Acad Sci U S A, 103*(51), 19518-19523. doi:10.1073/pnas.0606005103
- Bateman, R. J., Xiong, C., Benzinger, T. L., Fagan, A. M., Goate, A., Fox, N. C., . . . Dominantly Inherited Alzheimer, N. (2012). Clinical and biomarker changes in dominantly inherited Alzheimer's disease. *N Engl J Med, 367*(9), 795-804. doi:10.1056/NEJMoa1202753
- Bejanin, A., Schonhaut, D. R., La Joie, R., Kramer, J. H., Baker, S. L., Sosa, N., . . . Rabinovici, G. D. (2017). Tau pathology and neurodegeneration contribute to cognitive impairment in Alzheimer's disease. *Brain, 140*(12), 3286-3300. doi:10.1093/brain/awx243
- Bero, A. W., Yan, P., Roh, J. H., Cirrito, J. R., Stewart, F. R., Raichle, M. E., . . . Holtzman, D. M. (2011). Neuronal activity regulates the regional vulnerability to amyloid-beta deposition. *Nat Neurosci, 14*(6), 750-756. doi:10.1038/nn.2801
- Bertram, L., Lill, C. M., & Tanzi, R. E. (2010). The genetics of Alzheimer disease: back to the future. *Neuron, 68*(2), 270-281. doi:10.1016/j.neuron.2010.10.013
- Braak, H., & Braak, E. (1991). Neuropathological stageing of Alzheimer-related changes. *Acta*

- Neuropathol*, 82(4), 239-259.
- Braak, H., & Braak, E. (1995). Staging of Alzheimer's disease-related neurofibrillary changes. *Neurobiol Aging*, 16(3), 271-278; discussion 278-284.
- Braak, H., & Braak, E. (1997). Frequency of stages of Alzheimer-related lesions in different age categories. *Neurobiol Aging*, 18(4), 351-357.
- Braak, H., Thal, D. R., Ghebremedhin, E., & Del Tredici, K. (2011). Stages of the pathologic process in Alzheimer disease: age categories from 1 to 100 years. *J Neuropathol Exp Neurol*, 70(11), 960-969. doi:10.1097/NEN.0b013e318232a379
- Brier, M. R., Thomas, J. B., Fagan, A. M., Hassenstab, J., Holtzman, D. M., Benzinger, T. L., . . . Ances, B. M. (2014). Functional connectivity and graph theory in preclinical Alzheimer's disease. *Neurobiol Aging*, 35(4), 757-768. doi:10.1016/j.neurobiolaging.2013.10.081
- Brier, M. R., Thomas, J. B., Snyder, A. Z., Wang, L., Fagan, A. M., Benzinger, T., . . . Ances, B. M. (2014). Unrecognized preclinical Alzheimer disease confounds rs-fcMRI studies of normal aging. *Neurology*, 83(18), 1613-1619. doi:10.1212/WNL.0000000000000939
- Brookmeyer, R., Evans, D. A., Hebert, L., Langa, K. M., Heeringa, S. G., Plassman, B. L., & Kukull, W. A. (2011). National estimates of the prevalence of Alzheimer's disease in the United States. *Alzheimers Dement*, 7(1), 61-73. doi:10.1016/j.jalz.2010.11.007
- Brown, A. J., & Jessup, W. (2009). Oxysterols: Sources, cellular storage and metabolism, and new insights into their roles in cholesterol homeostasis. *Mol Aspects Med*, 30(3), 111-122. doi:10.1016/j.mam.2009.02.005
- Buckner, R. L., Sepulcre, J., Talukdar, T., Krienen, F. M., Liu, H., Hedden, T., . . . Johnson, K. A. (2009). Cortical hubs revealed by intrinsic functional connectivity: mapping, assessment of stability, and relation to Alzheimer's disease. *J Neurosci*, 29(6), 1860-1873. doi:10.1523/JNEUROSCI.5062-08.2009
- Bullmore, E., & Sporns, O. (2009). Complex brain networks: graph theoretical analysis of structural and functional systems. *Nat Rev Neurosci*, 10(3), 186-198. doi:10.1038/nrn2575
- Bullmore, E., & Sporns, O. (2012). The economy of brain network organization. *Nat Rev Neurosci*, 13(5), 336-349. doi:10.1038/nrn3214
- Carbonell, F., Charil, A., Zijdenbos, A. P., Evans, A. C., & Bedell, B. J. (2014). beta-Amyloid is associated with aberrant metabolic connectivity in subjects with mild cognitive impairment. *J Cereb Blood Flow Metab*, 34(7), 1169-1179. doi:10.1038/jcbfm.2014.66
- Chen, Z. J., He, Y., Rosa-Neto, P., Germann, J., & Evans, A. C. (2008). Revealing modular architecture of human brain structural networks by using cortical thickness from MRI. *Cereb Cortex*, 18(10), 2374-2381. doi:10.1093/cercor/bhn003
- Chen, Z. J., He, Y., Rosa-Neto, P., Gong, G., & Evans, A. C. (2011). Age-related alterations in the modular organization of structural cortical network by using cortical thickness from MRI. *Neuroimage*, 56(1), 235-245. doi:10.1016/j.neuroimage.2011.01.010
- Chetelat, G., Desgranges, B., Landeau, B., Mezenge, F., Poline, J. B., de la Sayette, V., . . . Baron, J. C. (2008). Direct voxel-based comparison between grey matter hypometabolism and atrophy in Alzheimer's disease. *Brain*, 131(Pt 1), 60-71. doi:10.1093/brain/awm288
- Chetelat, G., Landeau, B., Salmon, E., Yakushev, I., Bahri, M. A., Mezenge, F., . . . Fellgiebel, A. (2013). Relationships between brain metabolism decrease in normal aging and changes in structural and functional connectivity. *Neuroimage*, 76, 167-177. doi:10.1016/j.neuroimage.2013.03.009
- Chetelat, G., Villemagne, V. L., Villain, N., Jones, G., Ellis, K. A., Ames, D., . . . Group, A. R.

- (2012). Accelerated cortical atrophy in cognitively normal elderly with high beta-amyloid deposition. *Neurology*, 78(7), 477-484. doi:10.1212/WNL.0b013e318246d67a
- Chirotis, K., Saint-Aubert, L., Rodriguez-Vieitez, E., Leuzy, A., Almkvist, O., Savitcheva, I., . . . Nordberg, A. (2017). Longitudinal changes of tau PET imaging in relation to hypometabolism in prodromal and Alzheimer's disease dementia. *Mol Psychiatry*. doi:10.1038/mp.2017.108
- Cho, H., Choi, J. Y., Hwang, M. S., Kim, Y. J., Lee, H. M., Lee, H. S., . . . Lyoo, C. H. (2016). In vivo cortical spreading pattern of tau and amyloid in the Alzheimer disease spectrum. *Ann Neurol*, 80(2), 247-258. doi:10.1002/ana.24711
- Cirrito, J. R., Yamada, K. A., Finn, M. B., Sloviter, R. S., Bales, K. R., May, P. C., . . . Holtzman, D. M. (2005). Synaptic activity regulates interstitial fluid amyloid-beta levels in vivo. *Neuron*, 48(6), 913-922. doi:10.1016/j.neuron.2005.10.028
- Cohen, A. D., Price, J. C., Weissfeld, L. A., James, J., Rosario, B. L., Bi, W., . . . Klunk, W. E. (2009). Basal cerebral metabolism may modulate the cognitive effects of Abeta in mild cognitive impairment: an example of brain reserve. *J Neurosci*, 29(47), 14770-14778. doi:10.1523/JNEUROSCI.3669-09.2009
- Cole, M. W., Ito, T., Bassett, D. S., & Schultz, D. H. (2016). Activity flow over resting-state networks shapes cognitive task activations. *Nat Neurosci*, 19(12), 1718-1726. doi:10.1038/nn.4406
- Corder, E. H., Saunders, A. M., Strittmatter, W. J., Schmechel, D. E., Gaskell, P. C., Small, G. W., . . . Pericak-Vance, M. A. (1993). Gene dose of apolipoprotein E type 4 allele and the risk of Alzheimer's disease in late onset families. *Science*, 261(5123), 921-923.
- Crossley, N. A., Mechelli, A., Scott, J., Carletti, F., Fox, P. T., McGuire, P., & Bullmore, E. T. (2014). The hubs of the human connectome are generally implicated in the anatomy of brain disorders. *Brain*, 137(Pt 8), 2382-2395. doi:10.1093/brain/awu132
- de Calignon, A., Polydoro, M., Suarez-Calvet, M., William, C., Adamowicz, D. H., Kopeikina, K. J., . . . Hyman, B. T. (2012). Propagation of tau pathology in a model of early Alzheimer's disease. *Neuron*, 73(4), 685-697. doi:10.1016/j.neuron.2011.11.033
- de Haan, W., Mott, K., van Straaten, E. C., Scheltens, P., & Stam, C. J. (2012). Activity dependent degeneration explains hub vulnerability in Alzheimer's disease. *PLoS Comput Biol*, 8(8), e1002582. doi:10.1371/journal.pcbi.1002582
- de Leon, M. J., Ferris, S. H., George, A. E., Reisberg, B., Christman, D. R., Kricheff, II, & Wolf, A. P. (1983). Computed tomography and positron emission transaxial tomography evaluations of normal aging and Alzheimer's disease. *J Cereb Blood Flow Metab*, 3(3), 391-394. doi:10.1038/jcbfm.1983.57
- Deco, G., Jirsa, V. K., & McIntosh, A. R. (2011). Emerging concepts for the dynamical organization of resting-state activity in the brain. *Nat Rev Neurosci*, 12(1), 43-56. doi:10.1038/nrn2961
- Dennis, E. L., & Thompson, P. M. (2014). Functional brain connectivity using fMRI in aging and Alzheimer's disease. *Neuropsychol Rev*, 24(19), 49-62. doi:10.1007/s11065-014-9249-6
- Dolcos, F., Rice, H. J., & Cabeza, R. (2002). Hemispheric asymmetry and aging: right hemisphere decline or asymmetry reduction. *Neurosci Biobehav Rev*, 26(7), 819-825.
- Dore, V., Villemagne, V. L., Bourgeat, P., Fripp, J., Acosta, O., Chetelat, G., . . . Rowe, C. C. (2013). Cross-sectional and longitudinal analysis of the relationship between Abeta deposition, cortical thickness, and memory in cognitively unimpaired individuals and in

- Alzheimer disease. *JAMA Neurol*, 70(7), 903-911. doi:10.1001/jamaneurol.2013.1062
- Drzezga, A., Becker, J. A., Van Dijk, K. R., Sreenivasan, A., Talukdar, T., Sullivan, C., . . . Sperling, R. A. (2011). Neuronal dysfunction and disconnection of cortical hubs in non-demented subjects with elevated amyloid burden. *Brain*, 134(Pt 6), 1635-1646. doi:10.1093/brain/awr066
- Du, A. T., Schuff, N., Amend, D., Laakso, M. P., Hsu, Y. Y., Jagust, W. J., . . . Weiner, M. W. (2001). Magnetic resonance imaging of the entorhinal cortex and hippocampus in mild cognitive impairment and Alzheimer's disease. *J Neurol Neurosurg Psychiatry*, 71(4), 441-447.
- DuPre, E. and Spreng, N. (2017). Structural covariance networks across the life span, from 6 to 94 years of age. *Network Neuroscience*, 1(3), 302-323. doi:10.1162/NETN\_a\_00016
- Eisele, Y. S., Obermuller, U., Heilbronner, G., Baumann, F., Kaeser, S. A., Wolburg, H., . . . Jucker, M. (2010). Peripherally applied Abeta-containing inoculates induce cerebral beta-amyloidosis. *Science*, 330(6006), 980-982. doi:10.1126/science.1194516
- Farrell, M. E., Kennedy, K.M., Rodrigue, K.M., Wig, G., Bischof, G.N., Rieck, J.R., . . . Park, D.C. (2017). Association of longitudinal cognitive decline with amyloid burden in middle-aged and older adults: evidence for a dose-response relationship. *JAMA Neurol*, 74(7): 830-838.
- Fjell, A. M., Amlien, I. K., Sneve, M. H., Grydeland, H., Tamnes, C. K., Chaplin, T. A., . . . Walhovd, K. B. (2015). The Roots of Alzheimer's Disease: Are High-Expanding Cortical Areas Preferentially Targeted?dagger. *Cereb Cortex*, 25(9), 2556-2565. doi:10.1093/cercor/bhu055
- Fleisher, A. S., Chen, K., Quiroz, Y. T., Jakimovich, L. J., Gomez, M. G., Langois, C. M., . . . Reiman, E. M. (2012). Flortetapir PET analysis of amyloid-beta deposition in the presenilin 1 E280A autosomal dominant Alzheimer's disease kindred: a cross-sectional study. *Lancet Neurol*, 11(12), 1057-1065. doi:10.1016/S1474-4422(12)70227-2
- Fox, P. T., & Raichle, M. E. (1986). Focal physiological uncoupling of cerebral blood flow and oxidative metabolism during somatosensory stimulation in human subjects. *Proc Natl Acad Sci U S A*, 83(4), 1140-1144.
- Friedman, E. J., Young, K., Asif, D., Jutla, I., Liang, M., Wilson, S., . . . Alzheimer's Disease Neuroimaging, I. (2014). Directed progression brain networks in Alzheimer's disease: properties and classification. *Brain Connect*, 4(5), 384-393. doi:10.1089/brain.2014.0235
- Frost, B., & Diamond, M. I. (2010). Prion-like mechanisms in neurodegenerative diseases. *Nat Rev Neurosci*, 11(3), 155-159. doi:10.1038/nrn2786
- Garrett, D. D., Kovacevic, N., McIntosh, A. R., & Grady, C. L. (2011). The importance of being variable. *J Neurosci*, 31(12), 4496-4503. doi:10.1523/JNEUROSCI.5641-10.2011
- Geerligs, L., Renken, R. J., Saliasi, E., Maurits, N. M., & Lorist, M. M. (2015). A Brain-Wide Study of Age-Related Changes in Functional Connectivity. *Cereb Cortex*, 25(7), 1987-1999. doi:10.1093/cercor/bhu012
- Glasser, M. F., Sotiroopoulos, S. N., Wilson, J. A., Coalson, T. S., Fischl, B., Andersson, J. L., . . . Consortium, W.-M. H. (2013). The minimal preprocessing pipelines for the Human Connectome Project. *Neuroimage*, 80, 105-124. doi:10.1016/j.neuroimage.2013.04.127
- Gonneaud, J., Arenaza-Urquijo, E. M., Mezenge, F., Landeau, B., Gaubert, M., Bejanin, A., . . . Chetelat, G. (2017). Increased florbetapir binding in the temporal neocortex from age 20 to 60 years. *Neurology*, 89(24), 2438-2446. doi:10.1212/WNL.0000000000004733
- Gordon, B. A., Blazey, T. M., Su, Y., Hari-Raj, A., Dincer, A., Flores, S., . . . Benzinger, T. L. S.

- (2018). Spatial patterns of neuroimaging biomarker change in individuals from families with autosomal dominant Alzheimer's disease: a longitudinal study. *Lancet Neurol*, 17(3), 241-250. doi:10.1016/S1474-4422(18)30028-0
- Gotz, J., Ittner, L. M., & Kins, S. (2006). Do axonal defects in tau and amyloid precursor protein transgenic animals model axonopathy in Alzheimer's disease? *J Neurochem*, 98(4), 993-1006. doi:10.1111/j.1471-4159.2006.03955.x
- Goyal, M. S., Hawrylycz, M., Miller, J. A., Snyder, A. Z., & Raichle, M. E. (2014). Aerobic glycolysis in the human brain is associated with development and neotenous gene expression. *Cell Metab*, 19(1), 49-57. doi:10.1016/j.cmet.2013.11.020
- Goyal, M. S., Vlassenko, A. G., Blazey, T. M., Su, Y., Couture, L. E., Durbin, T. J., . . . Raichle, M. E. (2017). Loss of Brain Aerobic Glycolysis in Normal Human Aging. *Cell Metab*, 26(2), 353-360 e353. doi:10.1016/j.cmet.2017.07.010
- Grothe, M. J., Barthel, H., Sepulcre, J., Dyrba, M., Sabri, O., Teipel, S. J., & Alzheimer's Disease Neuroimaging, I. (2017). In vivo staging of regional amyloid deposition. *Neurology*, 89(20), 2031-2038. doi:10.1212/WNL.0000000000004643
- Grothe M. J., Teipel S. J., & Alzheimer's Disease Neuroimaging Initiative. (2016). Spatial patterns of atrophy, hypometabolism, and amyloid deposition in Alzheimer's disease correspond to dissociable functional brain networks. *Hum Brain Mapp*, 37(1), 35-53. doi:10.1002/hbm.23018
- Haass, C., & Selkoe, D. J. (2007). Soluble protein oligomers in neurodegeneration: lessons from the Alzheimer's amyloid beta-peptide. *Nat Rev Mol Cell Biol*, 8(2), 101-112. doi:10.1038/nrm2101
- Hanseeuw, B. J., Betensky, R. A., Schultz, A. P., Papp, K. V., Mormino, E. C., Sepulcre, J., . . . Johnson, K. A. (2017). Fluorodeoxyglucose metabolism associated with tau-amyloid interaction predicts memory decline. *Ann Neurol*, 81(4), 583-596. doi:10.1002/ana.24910
- Haynes, J. D. (2015). A Primer on Pattern-Based Approaches to fMRI: Principles, Pitfalls, and Perspectives. *Neuron*, 87(2), 257-270. doi:10.1016/j.neuron.2015.05.025
- He, Y., Chen, Z., & Evans, A. (2008). Structural insights into aberrant topological patterns of large-scale cortical networks in Alzheimer's disease. *J Neurosci*, 28(18), 4756-4766. doi:10.1523/JNEUROSCI.0141-08.2008
- He, Y., Chen, Z. J., & Evans, A. C. (2007). Small-world anatomical networks in the human brain revealed by cortical thickness from MRI. *Cereb Cortex*, 17(10), 2407-2419. doi:10.1093/cercor/bhl149
- He, Y., Wang, J., Wang, L., Chen, Z. J., Yan, C., Yang, H., . . . Evans, A. C. (2009). Uncovering intrinsic modular organization of spontaneous brain activity in humans. *PLoS One*, 4(4), e5226. doi:10.1371/journal.pone.0005226
- Hedden, T., Oh, H., Younger, A. P., & Patel, T. A. (2013). Meta-analysis of amyloid-cognition relations in cognitively normal older adults. *Neurology*, 80(14), 1341-1348. doi:10.1212/WNL.0b013e31828ab35d
- Herholz, K., Salmon, E., Perani, D., Baron, J. C., Holthoff, V., Frolich, L., . . . Heiss, W. D. (2002). Discrimination between Alzheimer dementia and controls by automated analysis of multicenter FDG PET. *Neuroimage*, 17(1), 302-316.
- Hill, J., Inder, T., Neil, J., Dierker, D., Harwell, J., & Van Essen, D. (2010). Similar patterns of cortical expansion during human development and evolution. *Proc Natl Acad Sci U S A*, 107(29), 13135-13140. doi:10.1073/pnas.1001229107
- Horwitz, B., Duara, R., & Rapoport, S. I. (1984). Intercorrelations of glucose metabolic rates

- between brain regions: application to healthy males in a state of reduced sensory input. *J Cereb Blood Flow Metab*, 4(4), 484-499. doi:10.1038/jcbfm.1984.73
- Horwitz, B., Duara, R., & Rapoport, S. I. (1986). Age differences in intercorrelations between regional cerebral metabolic rates for glucose. *Ann Neurol*, 19(1), 60-67. doi:10.1002/ana.410190111
- Horwitz, B., Grady, C. L., Schlageter, N. L., Duara, R., & Rapoport, S. I. (1987). Intercorrelations of regional cerebral glucose metabolic rates in Alzheimer's disease. *Brain Res*, 407(2), 294-306.
- Ibanez V., Pietrini, P., Alexander G. E., Furey, M. L., Teichberg, D., Rajapakse J. C., . . . Horwitz, B. (1998). Regional glucose metabolic abnormalities are not the result of atrophy in Alzheimer's disease. *Neurology*, 50(6), 1585-1593.
- Iqbal, K., Alonso Adel, C., Chen, S., Chohan, M. O., El-Akkad, E., Gong, C. X., . . . Grundke-Iqbali, I. (2005). Tau pathology in Alzheimer disease and other tauopathies. *Biochim Biophys Acta*, 1739(2-3), 198-210. doi:10.1016/j.bbadi.2004.09.008
- Ittner, L. M., & Gotz, J. (2011). Amyloid-beta and tau--a toxic pas de deux in Alzheimer's disease. *Nat Rev Neurosci*, 12(2), 65-72. doi:10.1038/nrn2967
- Ittner, L. M., Ke, Y. D., & Gotz, J. (2009). Phosphorylated Tau interacts with c-Jun N-terminal kinase-interacting protein 1 (JIP1) in Alzheimer disease. *J Biol Chem*, 284(31), 20909-20916. doi:10.1074/jbc.M109.014472
- Jack, C. R., Jr., Bennett, D. A., Blennow, K., Carrillo, M. C., Dunn, B., Haeberlein, S. B., . . . Contributors. (2018). NIA-AA Research Framework: Toward a biological definition of Alzheimer's disease. *Alzheimers Dement*, 14(4), 535-562. doi:10.1016/j.jalz.2018.02.018
- Jack, C. R., Jr., Knopman, D. S., Jagust, W. J., Shaw, L. M., Aisen, P. S., Weiner, M. W., . . . Trojanowski, J. Q. (2010). Hypothetical model of dynamic biomarkers of the Alzheimer's pathological cascade. *Lancet Neurol*, 9(1), 119-128. doi:10.1016/S1474-4422(09)70299-6
- Jack, C. R., Jr., Knopman, D. S., Jagust, W. J., Peterson, R. C., Weiner, M. W., Aisen, P. S., . . . Trojanowski, J. Q. (2013). Update on hypothetical model of Alzheimer's disease biomarkers. *Lancet Neurol*, 12(2), 207-216. doi:10.1016/S1474-4422(12)70291-0
- Jack, C. R., Jr., Wiste, H. J., Schwarz, C. G., Lowe, V. J., Senjem, M. L., Vemuri, P., . . . Petersen, R. C. (2018). Longitudinal tau PET in ageing and Alzheimer's disease. *Brain*. doi:10.1093/brain/awy059
- Jacobs, H. I. L., Hedden, T., Schultz, A. P., Sepulcre, J., Perea, R. D., Amariglio, R. E., . . . Johnson, K. A. (2018). Structural tract alterations predict downstream tau accumulation in amyloid-positive older individuals. *Nat Neurosci*. doi:10.1038/s41593-018-0070-z
- Jagust, W. (2013). Vulnerable neural systems and the borderland of brain aging and neurodegeneration. *Neuron*, 77(2), 219-234. doi:10.1016/j.neuron.2013.01.002
- Jagust, W. J., & Mormino, E. C. (2011). Lifespan brain activity, beta-amyloid, and Alzheimer's disease. *Trends Cogn Sci*, 15(11), 520-526. doi:10.1016/j.tics.2011.09.004
- Jansen, W. J., Ossenkoppele, R., Knol, D. L., Tijms, B. M., Scheltens, P., Verhey, F. R. J., . . . Amyloid Biomarker Study Group. (2015). Prevalence of cerebral amyloid pathology in persons without dementia: a meta-analysis. *JAMA*, 313(19), 1924-1938. doi:10.1001/jama.2015.4668
- Jansen, W. J., Ossenkoppele, R., Tijms, B. M., Fagan, A. M., Hansson, O., Klunk, W. E., . . . Zetterberg, H. (2018). Association of Cerebral Amyloid-beta Aggregation With Cognitive Functioning in Persons Without Dementia. *JAMA Psychiatry*, 75(1), 84-95.

doi:10.1001/jamapsychiatry.2017.3391

- Johnson, K. A., Schultz, A., Betensky, R. A., Becker, J. A., Sepulcre, J., Rentz, D., . . . Sperling, R. (2016). Tau positron emission tomographic imaging in aging and early Alzheimer disease. *Ann Neurol*, 79(1), 110-119. doi:10.1002/ana.24546
- Jones, D. T., Graff-Radford, J., Lowe, V. J., Wiste, H. J., Gunter, J. L., Senjem, M. L., . . . Jack, C. R., Jr. (2017). Tau, amyloid, and cascading network failure across the Alzheimer's disease spectrum. *Cortex*, 97, 143-159. doi:10.1016/j.cortex.2017.09.018
- Jones, D. T., Knopman, D. S., Gunter, J. L., Graff-Radford, J., Vemuri, P., Boeve, B. F., . . . Alzheimer's Disease Neuroimaging, I. (2016). Cascading network failure across the Alzheimer's disease spectrum. *Brain*, 139(Pt 2), 547-562. doi:10.1093/brain/awv338
- Kantarci, K., Lowe, V., Przybelski, S. A., Weigand, S. D., Senjem, M. L., Ivnik, R. J., . . . Jack, C. R., Jr. (2012). APOE modifies the association between Abeta load and cognition in cognitively normal older adults. *Neurology*, 78(4), 232-240. doi:10.1212/WNL.0b013e31824365ab
- Kawagoe, T., Onoda, K., & Yamaguchi, S. (2018). Different pre-scanning instructions induce distinct psychological and resting brain states during functional magnetic resonance imaging. *Eur J Neurosci*, 47(1), 77-82. doi:10.1111/ejn.13787
- Kiebel, S. J., Poline, J. B., Friston, K. J., Holmes, A. P., & Worsley, K. J. (1999). Robust smoothness estimation in statistical parametric maps using standardized residuals from the general linear model. *Neuroimage*, 10(6), 756-766. doi:10.1006/nimg.1999.0508
- Kljajevic, V., Grothe, M. J., Ewers, M., Teipel, S., Alzheimer's Disease Neuroimaging Initiative. (2014). Distinct pattern of hypometabolism and atrophy in preclinical and predementia Alzheimer's disease. *Neurobiol Aging*, 35(), 1973-1981. doi:10.1016/j.neurobiolaging.2014.04.006
- Klunk, W. E., Engler, H., Nordberg, A., Wang, Y., Blomqvist, G., Holt, D. P., . . . Langstrom, B. (2004). Imaging brain amyloid in Alzheimer's disease with Pittsburgh Compound-B. *Ann Neurol*, 55(3), 306-319. doi:10.1002/ana.20009
- Knowles, T. P., White, D. A., Abate, A. R., Agresti, J. J., Cohen, S. I., Sperling, R. A., . . . Weitz, D. A. (2011). Observation of spatial propagation of amyloid assembly from single nuclei. *Proc Natl Acad Sci U S A*, 108(36), 14746-14751. doi:10.1073/pnas.1105555108
- Kramer, J. H., Jurik, J., Sha, S. J., Rankin, K. P., Rosen, H. J., Johnson, J. K., & Miller, B. L. (2003). Distinctive neuropsychological patterns in frontotemporal dementia, semantic dementia, and Alzheimer disease. *Cogn Behav Neurol*, 16(4), 211-218.
- La Joie, R., Perrotin, A., Barré, L., Hommet, C., Mézenge, F., Ibazizene, . . . Chételat, G. (2012). Region-specific hierarchy between atrophy, hypometabolism, and  $\beta$ -amyloid ( $A\beta$ ) load in Alzheimer's disease dementia. *J Neurosci*, 32(46), 16265-16273. doi:10.1523/JNEUROSCI.2170-12.2012
- LaPoint, M. R., Chhatwal, J. P., Sepulcre, J., Johnson, K. A., Sperling, R. A., & Schultz, A. P. (2017). The association between tau PET and retrospective cortical thinning in clinically normal elderly. *Neuroimage*, 157, 612-622. doi:10.1016/j.neuroimage.2017.05.049
- Leal, S. L., Lockhart, S. N., Maass, A., Bell, R. K., & Jagust, W. J. (2018). Subthreshold amyloid predicts local tau deposition in aging. *Journal of Neuroscience* In press.
- Liang, X., Zou, Q., He, Y., & Yang, Y. (2013). Coupling of functional connectivity and regional cerebral blood flow reveals a physiological basis for network hubs of the human brain. *Proc Natl Acad Sci U S A*, 110(5), 1929-1934. doi:10.1073/pnas.1214900110
- Lin, A. L., Fox, P. T., Hardies, J., Duong, T. Q., & Gao, J. H. (2010). Nonlinear coupling

- between cerebral blood flow, oxygen consumption, and ATP production in human visual cortex. *Proc Natl Acad Sci U S A*, 107(18), 8446-8451. doi:10.1073/pnas.0909711107
- Lockhart, S. N., Scholl, M., Baker, S. L., Ayakta, N., Swinnerton, K. N., Bell, R. K., . . . Jagust, W. J. (2017). Amyloid and tau PET demonstrate region-specific associations in normal older people. *Neuroimage*, 150, 191-199. doi:10.1016/j.neuroimage.2017.02.051
- Logan, J., Fowler, J. S., Volkow, N. D., Wang, G. J., Ding, Y. S., & Alexoff, D. L. (1996). Distribution volume ratios without blood sampling from graphical analysis of PET data. *J Cereb Blood Flow Metab*, 16(5), 834-840. doi:10.1097/00004647-199609000-00008
- Lord, L. D., Expert, P., Huckins, J. F., & Turkheimer, F. E. (2013). Cerebral energy metabolism and the brain's functional network architecture: an integrative review. *J Cereb Blood Flow Metab*, 33(9), 1347-1354. doi:10.1038/jcbfm.2013.94
- Lowe, V. J., Weigand, S. D., Senjem, M. L., Vemuri, P., Jordan, L., Kantarci, K., . . . Petersen, R. C. (2014). Association of hypometabolism and amyloid levels in aging, normal subjects. *Neurology*, 82(22), 1959-1967. doi:10.1212/WNL.0000000000000467
- Lowe, V. J., Wiste, H. J., Senjem, M. L., Weigand, S. D., Therneau, T. M., Boeve, B. F., . . . Jack, C. R., Jr. (2018). Widespread brain tau and its association with ageing, Braak stage and Alzheimer's dementia. *Brain*, 141(1), 271-287. doi:10.1093/brain/awx320
- Maass, A., Landau, S., Baker, S. L., Horng, A., Lockhart, S. N., La Joie, R., . . . Alzheimer's Disease Neuroimaging, I. (2017). Comparison of multiple tau-PET measures as biomarkers in aging and Alzheimer's disease. *Neuroimage*, 157, 448-463. doi:10.1016/j.neuroimage.2017.05.058
- Maass, A., Lockhart, S. N., Harrison, T. M., Bell, R. K., Mellinger, T., Swinnerton, K., . . . Jagust, W. J. (2018). Entorhinal Tau Pathology, Episodic Memory Decline, and Neurodegeneration in Aging. *J Neurosci*, 38(3), 530-543. doi:10.1523/JNEUROSCI.2028-17.2017
- Marcus, D. S., Harwell, J., Olsen, T., Hodge, M., Glasser, M. F., Prior, F., . . . Van Essen, D. C. (2011). Informatics and data mining tools and strategies for the human connectome project. *Front Neuroinform*, 5, 4. doi:10.3389/fninf.2011.00004
- Masliah, E., Mallory, M., Hansen, L., DeTeresa, R., & Terry, R. D. (1993). Quantitative synaptic alterations in the human neocortex during normal aging. *Neurology*, 43(1), 192-197.
- Mathis, C. A., Wang, Y., Holt, D. P., Huang, G. F., Debnath, M. L., & Klunk, W. E. (2003). Synthesis and evaluation of <sup>11</sup>C-labeled 6-substituted 2-arylbenzothiazoles as amyloid imaging agents. *J Med Chem*, 46(13), 2740-2754. doi:10.1021/jm030026b
- McIntosh, A. R., Kovacevic, N., Lippe, S., Garrett, D., Grady, C., & Jirsa, V. (2010). The development of a noisy brain. *Arch Ital Biol*, 148(3), 323-337.
- McKhann, G. M., Knopman, D. S., Chertkow, H., Hyman, B. T., Jack, C. R., Jr., Kawas, C. H., . . . Phelps, C. H. (2011). The diagnosis of dementia due to Alzheimer's disease: recommendations from the National Institute on Aging-Alzheimer's Association workgroups on diagnostic guidelines for Alzheimer's disease. *Alzheimers Dement*, 7(3), 263-269. doi:10.1016/j.jalz.2011.03.005
- Mesulam, M. M. (1999). Neuroplasticity failure in Alzheimer's disease: bridging the gap between plaques and tangles. *Neuron*, 24(3), 521-529.
- Mezias, C., & Raj, A. (2017). Analysis of Amyloid-beta Pathology Spread in Mouse Models Suggests Spread Is Driven by Spatial Proximity, Not Connectivity. *Front Neurol*, 8, 653. doi:10.3389/fneur.2017.00653
- Minoshima, S., Frey, K. A., Foster, N. L., & Kuhl, D. E. (1995) Preserved pontine glucose

- metabolism in Alzheimer's disease: a reference region for functional brain image (PET) analysis. *J Comput Assist Tomogr*, 19(4), 541-547. doi:10.1097/00004728-199507000-00006
- Minoshima, S., Giordani, B., Berent, S., Frey, K. A., Foster, N. L., & Kuhl, D. E. (1997). Metabolic reduction in the posterior cingulate cortex in very early Alzheimer's disease. *Ann Neurol*, 42(1), 85-94. doi:10.1002/ana.410420114
- Montembeault, M., Rouleau, I., Provost, J. S., Brambati, S. M., & Alzheimer's Disease Neuroimaging Initiative. (2016). Altered gray matter structural covariance networks in early stages of Alzheimer's disease. *Cereb Cortex*, 26(6), 2650-2662. doi:10.1093/cercor/bhv10
- Moreno-Gonzalez, I., & Soto, C. (2011). Misfolded protein aggregates: mechanisms, structures and potential for disease transmission. *Semin Cell Dev Biol*, 22(5), 482-487. doi:10.1016/j.semcdcb.2011.04.002
- Mormino, E. C., Betensky, R. A., Hedden, T., Schultz, A. P., Ward, A., Huijbers, W., . . . Harvard Aging Brain, S. (2014). Amyloid and APOE epsilon4 interact to influence short-term decline in preclinical Alzheimer disease. *Neurology*, 82(20), 1760-1767. doi:10.1212/WNL.000000000000431
- Mormino, E. C., Brandel, M. G., Madison, C. M., Rabinovici, G. D., Marks, S., Baker, S. L., & Jagust, W. J. (2012). Not quite PIB-positive, not quite PIB-negative: slight PIB elevations in elderly normal control subjects are biologically relevant. *Neuroimage*, 59(2), 1152-1160. doi:10.1016/j.neuroimage.2011.07.098
- Mosconi, L. (2005). Brain glucose metabolism in the early and specific diagnosis of Alzheimer's disease. FDG-PET studies in MCI and AD. *Eur J Nucl Med Mol Imaging*, 32(4), 486-510. doi:10.1007/s00259-005-1762-7
- Mosconi, L. (2013). Glucose metabolism in normal aging and Alzheimer's disease: Methodological and physiological considerations for PET studies. *Clin Transl Imaging*, 1(4). doi:10.1007/s40336-013-0026-y
- Naslund, J., Haroutunian, V., Mohs, R., Davis, K. L., Davies, P., Greengard, P., & Buxbaum, J. D. (2000). Correlation between elevated levels of amyloid beta-peptide in the brain and cognitive decline. *JAMA*, 283(12), 1571-1577.
- Newberg, A. B., Wang, J., Rao, H., Swanson, R. L., Wintering, N., Karp, J. S., . . . Detre, J. A. (2005). Concurrent CBF and CMRGlc changes during human brain activation by combined fMRI-PET scanning. *Neuroimage*, 28(2), 500-506. doi:10.1016/j.neuroimage.2005.06.040
- Norman, K. A., Polyn, S. M., Detre, G. J., & Haxby, J. V. (2006). Beyond mind-reading: multi-voxel pattern analysis of fMRI data. *Trends Cogn Sci*, 10(9), 424-430. doi:10.1016/j.tics.2006.07.005
- Oddo, S., Billings, L., Kesslak, J. P., Cribbs, D. H., & LaFerla, F. M. (2004). Abeta immunotherapy leads to clearance of early, but not late, hyperphosphorylated tau aggregates via the proteasome. *Neuron*, 43(3), 321-332. doi:10.1016/j.neuron.2004.07.003
- Oh, H., Habeck, C., Madison, C., & Jagust, W. (2014). Covarying alterations in Abeta deposition, glucose metabolism, and gray matter volume in cognitively normal elderly. *Hum Brain Mapp*, 35(1), 297-308. doi:10.1002/hbm.22173
- Oh, H., Madison, C., Baker, S., Rabinovici, G., & Jagust, W. (2016). Dynamic relationships between age, amyloid-beta deposition, and glucose metabolism link to the regional

- vulnerability to Alzheimer's disease. *Brain*. doi:10.1093/brain/aww108
- Ossenkoppele, R., Schonhaut, D. R., Scholl, M., Lockhart, S. N., Ayakta, N., Baker, S. L., . . . Rabinovici, G. D. (2016). Tau PET patterns mirror clinical and neuroanatomical variability in Alzheimer's disease. *Brain*, 139(Pt 5), 1551-1567. doi:10.1093/brain/aww027
- Palmqvist, S., Scholl, M., Strandberg, O., Mattsson, N., Stomrud, E., Zetterberg, H., . . . Hansson, O. (2017). Earliest accumulation of beta-amyloid occurs within the default-mode network and concurrently affects brain connectivity. *Nat Commun*, 8(1), 1214. doi:10.1038/s41467-017-01150-x
- Park, D. C., Polk, T. A., Park, R., Minear, M., Savage, A., & Smith, M. R. (2004). Aging reduces neural specialization in ventral visual cortex. *Proc Natl Acad Sci U S A*, 101(35), 13091-13095. doi:10.1073/pnas.0405148101
- Park, D. C., & Reuter-Lorenz, P. (2009). The adaptive brain: aging and neurocognitive scaffolding. *Annu Rev Psychol*, 60, 173-196. doi:10.1146/annurev.psych.59.103006.093656
- Patriat, R., Molloy, E. K., Meier, T. B., Kirk, G. R., Nair, V. A., Meyerand, M. E., . . . Birn, R. M. (2013). The effect of resting condition on resting-state fMRI reliability and consistency: a comparison between resting with eyes open, closed, and fixated. *Neuroimage*, 78, 463-473. doi:10.1016/j.neuroimage.2013.04.013
- Phelps, M. E., Huang, S. C., Hoffman, E. J., Selin, C., Sokoloff, L., & Kuhl, D. E. (1979). Tomographic measurement of local cerebral glucose metabolic rate in humans with (F-18)2-fluoro-2-deoxy-D-glucose: validation of method. *Ann Neurol*, 6(5), 371-388. doi:10.1002/ana.410060502
- Power, J. D., Cohen, A. L., Nelson, S. M., Wig, G. S., Barnes, K. A., Church, J. A., . . . Petersen, S. E. (2011). Functional network organization of the human brain. *Neuron*, 72(4), 665-678. doi:10.1016/j.neuron.2011.09.006
- Prakash, R. S., Heo, S., Voss, M. W., Patterson, B., & Kramer, A. F. (2012). Age-related differences in cortical recruitment and suppression: implications for cognitive performance. *Behav Brain Res*, 230(1), 192-200. doi:10.1016/j.bbr.2012.01.058
- Price, J. L., & Morris, J. C. (1999). Tangles and plaques in nondemented aging and "preclinical" Alzheimer's disease. *Ann Neurol*, 45(3), 358-368.
- Priller, C., Bauer, T., Mitteregger, G., Krebs, B., Kretzschmar, H. A., & Herms, J. (2006). Synapse formation and function is modulated by the amyloid precursor protein. *J Neurosci*, 26(27), 7212-7221. doi:10.1523/JNEUROSCI.1450-06.2006
- Raj, A., Kuceyeski, A., & Weiner, M. (2012). A network diffusion model of disease progression in dementia. *Neuron*, 73(6), 1204-1215. doi:10.1016/j.neuron.2011.12.040
- Reisberg, B., Franssen, E. H., Souren, L. E., Auer, S. R., Akram, I., & Kenowsky, S. (2002). Evidence and mechanisms of retrogenesis in Alzheimer's and other dementias: management and treatment import. *Am J Alzheimers Dis Other Demen*, 17(4), 202-212. doi:10.1177/153331750201700411
- Richiardi, J., Altmann, A., Milazzo, A. C., Chang, C., Chakravarty, M. M., Banaschewski, T., . . . consortium, I. (2015). BRAIN NETWORKS. Correlated gene expression supports synchronous activity in brain networks. *Science*, 348(6240), 1241-1244. doi:10.1126/science.1255905
- Riedl, V., Bienkowska, K., Strobel, C., Tahmasian, M., Grimmer, T., Forster, S., . . . Drzezga, A. (2014). Local activity determines functional connectivity in the resting human brain: a

- simultaneous FDG-PET/fMRI study. *J Neurosci*, 34(18), 6260-6266.  
doi:10.1523/JNEUROSCI.0492-14.2014
- Roberson, E. D., Scearce-Levie, K., Palop, J. J., Yan, F., Cheng, I. H., Wu, T., . . . Mucke, L. (2007). Reducing endogenous tau ameliorates amyloid beta-induced deficits in an Alzheimer's disease mouse model. *Science*, 316(5825), 750-754.  
doi:10.1126/science.1141736
- Rocher, A. B., Chapon, F., Blaizot, X., Baron, J. C., & Chavoix, C. (2003). Resting-state brain glucose utilization as measured by PET is directly related to regional synaptophysin levels: a study in baboons. *Neuroimage*, 20(3), 1894-1898.
- Rousset, O. G., Ma, Y., & Evans, A. C. (1998). Correction for partial volume effects in PET: principle and validation. *J Nucl Med*, 39(5), 904-911.
- Rowe, C. C., Ng, S., Ackermann, U., Gong, S. J., Pike, K., Savage, G., . . . Villemagne, V. L. (2007). Imaging beta-amyloid burden in aging and dementia. *Neurology*, 68(20), 1718-1725. doi:10.1212/01.wnl.0000261919.22630.ea
- Saenger, V. M., Ponce-Alvarez, A., Adhikari, M., Hagmann, P., Deco, G., & Corbetta, M. (2017). Linking entropy at rest with the underlying structural connectivity in the healthy and lesioned brain. *Cereb Cortex*. doi:10.1093/cercor/bhx176
- Saint-Aubert, L., Lemoine, L., Chirotis, K., Leuzy, A., Rodriguez-Vieitez, E., & Nordberg, A. (2017). Tau PET imaging: present and future directions. *Mol Neurodegener*, 12(1), 19. doi:10.1186/s13024-017-0162-3
- Sala-Llonch, R., Bartres-Faz, D., & Junque, C. (2015). Reorganization of brain networks in aging: a review of functional connectivity studies. *Front Psychol*, 6, 663.  
doi:10.3389/fpsyg.2015.00663
- Salvador, R., Suckling, J., Coleman, M. R., Pickard, J. D., Menon, D., & Bullmore, E. (2005). Neurophysiological architecture of functional magnetic resonance images of human brain. *Cereb Cortex*, 15(9), 1332-1342. doi:10.1093/cercor/bhi016
- Sanabria-Diaz, G., Martinez-Montes, E., Melie-Garcia, L., & Alzheimer's Disease Neuroimaging, I. (2013). Glucose metabolism during resting state reveals abnormal brain networks organization in the Alzheimer's disease and mild cognitive impairment. *PLoS One*, 8(7), e68860. doi:10.1371/journal.pone.0068860
- Satpute-Krishnan, P., DeGiorgis, J. A., Conley, M. P., Jang, M., & Bearer, E. L. (2006). A peptide zipcode sufficient for anterograde transport within amyloid precursor protein. *Proc Natl Acad Sci U S A*, 103(44), 16532-16537. doi:10.1073/pnas.0607527103
- Schellenberg, G. D. (1995). Genetic dissection of Alzheimer disease, a heterogeneous disorder. *Proc Natl Acad Sci U S A*, 92(19), 8552-8559.
- Scholl, M., Lockhart, S. N., Schonhaut, D. R., O'Neil, J. P., Janabi, M., Ossenkoppele, R., . . . Jagust, W. J. (2016). PET Imaging of Tau Deposition in the Aging Human Brain. *Neuron*, 89(5), 971-982. doi:10.1016/j.neuron.2016.01.028
- Scholl, M., Ossenkoppele, R., Strandberg, O., Palmqvist, S., Swedish Bio, F. s., Jogi, J., . . . Hansson, O. (2017). Distinct 18F-AV-1451 tau PET retention patterns in early- and late-onset Alzheimer's disease. *Brain*, 140(9), 2286-2294. doi:10.1093/brain/awx171
- Schwarz, A. J., Yu, P., Miller, B. B., Shcherbinin, S., Dickson, J., Navitsky, M., . . . Mintun, M. S. (2016). Regional profiles of the candidate tau PET ligand 18F-AV-1451 recapitulate key features of Braak histopathological stages. *Brain*, 139(Pt 5), 1539-1550.  
doi:10.1093/brain/aww023
- Seeley, W. W., Crawford, R. K., Zhou, J., Miller, B. L., & Greicius, M. D. (2009).

- Neurodegenerative diseases target large-scale human brain networks. *Neuron*, 62(1), 42-52. doi:10.1016/j.neuron.2009.03.024
- Sepulcre, J., Sabuncu, M. R., Becker, A., Sperling, R., & Johnson, K. A. (2013). In vivo characterization of the early states of the amyloid-beta network. *Brain*, 136(Pt 7), 2239-2252. doi:10.1093/brain/awt146
- Sepulcre, J., Schultz, A. P., Sabuncu, M., Gomez-Isla, T., Chhatwal, J., Becker, A., . . . Johnson, K. A. (2016). In Vivo Tau, Amyloid, and Gray Matter Profiles in the Aging Brain. *J Neurosci*, 36(28), 7364-7374. doi:10.1523/JNEUROSCI.0639-16.2016
- Shankar, G. M., Li, S., Mehta, T. H., Garcia-Munoz, A., Shepardson, N. E., Smith, I., . . . Selkoe, D. J. (2008). Amyloid-beta protein dimers isolated directly from Alzheimer's brains impair synaptic plasticity and memory. *Nat Med*, 14(8), 837-842. doi:10.1038/nm1782
- Shaw, P., Lerch, J. P., Pruessner, J. C., Taylor, K. N., Rose, A. B., Greenstein, D., . . . Giedd, J. N. (2007). Cortical morphology in children and adolescents with different apolipoprotein E gene polymorphisms: an observational study. *Lancet Neurol*, 6(6), 494-500. doi:10.1016/S1474-4422(07)70106-0
- Sheline, Y. I., & Raichle, M. E. (2013). Resting state functional connectivity in preclinical Alzheimer's disease. *Biol Psychiatry*, 74(5), 340-347. doi:10.1016/j.biopsych.2012.11.028
- Shirer, W. R., Ryali, S., Rykhlevskaia, E., Menon, V., & Greicius, M. D. (2012). Decoding subject-driven cognitive states with whole-brain connectivity patterns. *Cereb Cortex*, 22(1), 158-165. doi:10.1093/cercor/bhr099
- Smith, S. M., Vidaurre, D., Beckmann, C. F., Glasser, M. F., Jenkinson, M., Miller, K. L., . . . Van Essen, D. C. (2013). Functional connectomics from resting-state fMRI. *Trends Cogn Sci*, 17(12), 666-682. doi:10.1016/j.tics.2013.09.016
- Sperling, R. A., Aisen, P. S., Beckett, L. A., Bennett, D. A., Craft, S., Fagan, A. M., . . . Phelps, C. H. (2011). Toward defining the preclinical stages of Alzheimer's disease: recommendations from the National Institute on Aging-Alzheimer's Association workgroups on diagnostic guidelines for Alzheimer's disease. *Alzheimers Dement*, 7(3), 280-292. doi:10.1016/j.jalz.2011.03.003
- Sperling, R. A., Laviolette, P. S., O'Keefe, K., O'Brien, J., Rentz, D. M., Pihlajamaki, M., . . . Johnson, K. A. (2009). Amyloid deposition is associated with impaired default network function in older persons without dementia. *Neuron*, 63(2), 178-188. doi:10.1016/j.neuron.2009.07.003
- Spreng, R. N., & Turner, G. R. (2013). Structural covariance of the default network in healthy and pathological aging. *J Neurosci*, 33(38), 15226-15234. doi:10.1523/JNEUROSCI.2261-13.2013
- Stam, C. J., Jones, B. F., Nolte, G., Breakspear, M., & Scheltens, P. (2007). Small-world networks and functional connectivity in Alzheimer's disease. *Cereb Cortex*, 17(1), 92-99. doi:10.1093/cercor/bhj127
- Styr, B., & Slutsky, I. (2018). Imbalance between firing homeostasis and synaptic plasticity drives early-phase Alzheimer's disease. *Nat Neurosci*. doi:10.1038/s41593-018-0080-x
- Thal, D. R., Rub, U., Orantes, M., & Braak, H. (2002). Phases of A beta-deposition in the human brain and its relevance for the development of AD. *Neurology*, 58(12), 1791-1800.
- Tomasi, D., & Volkow, N. D. (2012). Aging and functional brain networks. *Mol Psychiatry*, 17(5), 549-558. doi:10.1038/mp.2011.81
- Tomasi, D., Wang, G. J., & Volkow, N. D. (2013). Energetic cost of brain functional

- connectivity. *Proc Natl Acad Sci U S A*, 110(33), 13642-13647. doi:10.1073/pnas.1303346110
- Tosun, D., Landau, S., Aisen, P. S., Petersen, R. C., Mintun, M., Jagust, W., . . . Alzheimer's Disease Neuroimaging, I. (2017). Association between tau deposition and antecedent amyloid-beta accumulation rates in normal and early symptomatic individuals. *Brain*, 140(5), 1499-1512. doi:10.1093/brain/awx046
- Tsai, J., Grutzendler, J., Duff, K., & Gan, W. B. (2004). Fibrillar amyloid deposition leads to local synaptic abnormalities and breakage of neuronal branches. *Nat Neurosci*, 7(11), 1181-1183. doi:10.1038/nn1335
- Ugurbil, K., Xu, J., Auerbach, E. J., Moeller, S., Vu, A. T., Duarte-Carvajalino, J. M., . . . Consortium, W. U.-M. H. (2013). Pushing spatial and temporal resolution for functional and diffusion MRI in the Human Connectome Project. *Neuroimage*, 80, 80-104. doi:10.1016/j.neuroimage.2013.05.012
- Vaishnavi, S. N., Vlassenko, A. G., Rundle, M. M., Snyder, A. Z., Mintun, M. A., & Raichle, M. E. (2010). Regional aerobic glycolysis in the human brain. *Proc Natl Acad Sci U S A*, 107(41), 17757-17762. doi:10.1073/pnas.1010459107
- Van Essen, D. C., Smith, S. M., Barch, D. M., Behrens, T. E., Yacoub, E., Ugurbil, K., & Consortium, W. U.-M. H. (2013). The WU-Minn Human Connectome Project: an overview. *Neuroimage*, 80, 62-79. doi:10.1016/j.neuroimage.2013.05.041
- Villemagne, V. L., Burnham, S., Bourgeat, P., Brown, B., Ellis, K. A., Salvado, O., . . . Lifestyle Research, G. (2013). Amyloid beta deposition, neurodegeneration, and cognitive decline in sporadic Alzheimer's disease: a prospective cohort study. *Lancet Neurol*, 12(4), 357-367. doi:10.1016/S1474-4422(13)70044-9
- Villeneuve, S., Rabinovici, G. D., Cohn-Sheehy, B. I., Madison, C., Ayakta, N., Ghosh, P. M., . . . Jagust, W. (2015). Existing Pittsburgh Compound-B positron emission tomography thresholds are too high: statistical and pathological evaluation. *Brain*, 138(Pt 7), 2020-2033. doi:10.1093/brain/awv112
- Vlassenko, A. G., Vaishnavi, S. N., Couture, L., Sacco, D., Shannon, B. J., Mach, R. H., . . . Mintun, M. A. (2010). Spatial correlation between brain aerobic glycolysis and amyloid-beta (Abeta) deposition. *Proc Natl Acad Sci U S A*, 107(41), 17763-17767. doi:10.1073/pnas.1010461107
- Walker, L. C., & LeVine, H., 3rd. (2012). Corruption and spread of pathogenic proteins in neurodegenerative diseases. *J Biol Chem*, 287(40), 33109-33115. doi:10.1074/jbc.R112.399378
- Wang, L., Benzinger, T. L., Su, Y., Christensen, J., Friedrichsen, K., Aldea, P., . . . Ances, B. M. (2016). Evaluation of Tau Imaging in Staging Alzheimer Disease and Revealing Interactions Between beta-Amyloid and Tauopathy. *JAMA Neurol*, 73(9), 1070-1077. doi:10.1001/jamaneurol.2016.2078
- Wirth, M., Madison, C. M., Rabinovici, G. D., Oh, H., Landau, S. M., & Jagust, W. J. (2013). Alzheimer's disease neurodegenerative biomarkers are associated with decreased cognitive function but not beta-amyloid in cognitively normal older individuals. *J Neurosci*, 33(13), 5553-5563. doi:10.1523/JNEUROSCI.4409-12.2013
- Wolf, A. B., Valla, J., Bu, G., Kim, J., LaDu, M. J., Reiman, E. M., & Caselli, R. J. (2013). Apolipoprotein E as a beta-amyloid-independent factor in Alzheimer's disease. *Alzheimers Res Ther*, 5(5), 38. doi:10.1186/alzrt204
- Xia, C., Makarets, S. J., Caso, C., McGinnis, S., Gomperts, S. N., Sepulcre, J., . . . Dickerson, B.

- C. (2017). Association of In Vivo [18F]AV-1451 Tau PET Imaging Results With Cortical Atrophy and Symptoms in Typical and Atypical Alzheimer Disease. *JAMA Neurol*, 74(4), 427-436. doi:10.1001/jamaneurol.2016.5755
- Yao, Z., Hu, B., Zheng, J., Zheng, W., Chen, X., Gao, X., . . . Alzheimer's Disease Neuroimaging, I. (2015). A FDG-PET Study of Metabolic Networks in Apolipoprotein E epsilon4 Allele Carriers. *PLoS One*, 10(7), e0132300. doi:10.1371/journal.pone.0132300
- Yao, Z., Zhang, Y., Lin, L., Zhou, Y., Xu, C., & Jiang, T. (2010). Abnormal cortical networks in mild cognitive impairment and Alzheimer's disease. *Plos Comp Biol*, 6(11). doi:10.1371/journal.pcbi.1001006
- Zhou, J., Gennatas, E. D., Kramer, J. H., Miller, B. L., & Seeley, W. W. (2012). Predicting regional neurodegeneration from the healthy brain functional connectome. *Neuron*, 73(6), 1216-1227. doi:10.1016/j.neuron.2012.03.004
- Zimmer, E. R., Parent, M. J., Souza, D. G., Leuzy, A., Lecrux, C., Kim, H. I., . . . Rosa-Neto, P. (2017). [18F]FDG PET signal is driven by astroglial glutamate transport. *Nat Neurosci*. doi:10.1038/nn.4492

## Appendix

#	<b>Freesurfer ROI</b>	<b>Lobe</b>	#	<b>Freesurfer ROI</b>	<b>Lobe</b>
1	ctx-lh-caudalanteriorcingulate	Cingulate	41	ctx-rh-caudalanteriorcingulate	Cingulate
2	ctx-lh-isthmuscingulate	Cingulate	42	ctx-rh-isthmuscingulate	Cingulate
3	ctx-lh-posteriorcingulate	Cingulate	43	ctx-rh-posteriorcingulate	Cingulate
4	ctx-lh-rostralanteriorcingulate	Cingulate	44	ctx-rh-rostralanteriorcingulate	Cingulate
5	ctx-lh-caudalmiddlefrontal	Frontal	45	ctx-rh-caudalmiddlefrontal	Frontal
6	ctx-lh-frontalpole	Frontal	46	ctx-rh-frontalpole	Frontal
7	ctx-lh-lateralorbitofrontal	Frontal	47	ctx-rh-lateralorbitofrontal	Frontal
8	ctx-lh-medialorbitofrontal	Frontal	48	ctx-rh-medialorbitofrontal	Frontal
9	ctx-lh-paracentral	Frontal	49	ctx-rh-paracentral	Frontal
10	ctx-lh-parsopercularis	Frontal	50	ctx-rh-parsopercularis	Frontal
11	ctx-lh-parsorbitalis	Frontal	51	ctx-rh-parsorbitalis	Frontal
12	ctx-lh-parstriangularis	Frontal	52	ctx-rh-parstriangularis	Frontal
13	ctx-lh-precentral	Frontal	53	ctx-rh-precentral	Frontal
14	ctx-lh-rostralmiddlefrontal	Frontal	54	ctx-rh-rostralmiddlefrontal	Frontal
15	ctx-lh-superiorfrontal	Frontal	55	ctx-rh-superiorfrontal	Frontal
16	ctx-lh-insula	Insula	56	ctx-rh-insula	Insula
17	ctx-lh-cuneus	Occipital	57	ctx-rh-cuneus	Occipital
18	ctx-lh-lateraloccipital	Occipital	58	ctx-rh-lateraloccipital	Occipital
19	ctx-lh-lingual	Occipital	59	ctx-rh-lingual	Occipital
20	ctx-lh-pericalcarine	Occipital	60	ctx-rh-pericalcarine	Occipital
21	ctx-lh-inferiorparietal	Parietal	61	ctx-rh-inferiorparietal	Parietal
22	ctx-lh-postcentral	Parietal	62	ctx-rh-postcentral	Parietal
23	ctx-lh-precuneus	Parietal	63	ctx-rh-precuneus	Parietal
24	ctx-lh-superiorparietal	Parietal	64	ctx-rh-superiorparietal	Parietal
25	ctx-lh-supramarginal	Parietal	65	ctx-rh-supramarginal	Parietal
26	Left-Amygdala	Subcortical	66	Right-Amygdala	Subcortical
27	Left-Caudate	Subcortical	67	Right-Caudate	Subcortical
28	Left-Cerebellum-Cortex	Subcortical	68	Right-Cerebellum-Cortex	Subcortical
29	Left-Hippocampus	Subcortical	69	Right-Hippocampus	Subcortical
30	Left-Pallidum	Subcortical	70	Right-Pallidum	Subcortical
31	Left-Putamen	Subcortical	71	Right-Putamen	Subcortical
32	Left-Thalamus-Proper	Subcortical	72	Right-Thalamus-Proper	Subcortical
33	ctx-lh-entorhinal	Temporal	73	ctx-rh-entorhinal	Temporal
34	ctx-lh-fusiform	Temporal	74	ctx-rh-fusiform	Temporal
35	ctx-lh-inferiortemporal	Temporal	75	ctx-rh-inferiortemporal	Temporal
36	ctx-lh-middletemporal	Temporal	76	ctx-rh-middletemporal	Temporal
37	ctx-lh-parahippocampal	Temporal	77	ctx-rh-parahippocampal	Temporal
38	ctx-lh-superiortemporal	Temporal	78	ctx-rh-superiortemporal	Temporal
39	ctx-lh-temporalpole	Temporal	79	ctx-rh-temporalpole	Temporal
40	ctx-lh-transversetemporal	Temporal	80	ctx-rh-transversetemporal	Temporal

**Table 1:** Numerical labels and lobe membership for all regions from the Freesurfer Desikan-Killiany atlas.